



ENHANCED BOUNDING SURFACE MODELLING OF UNDRAINED SAND BEHAVIOUR UNDER MULTIPLE LOADING CYCLES

Fotios-Iason Zygounas

M.Sc. Thesis report

ENHANCED BOUNDING SURFACE PLASTICITY MODELLING OF UNDRAINED SAND BEHAVIOUR UNDER MULTIPLE LOADING CYCLES

A Thesis presented for the degree of Master of Science in Civil
Engineering

by
Fotios Iason Zygounas

Committee: Prof. Cristina Jommi

TU Delft, chairperson

Dr. Federico Pisanò

TU Delft, daily supervisor

Dr. ir. K.N. van Dalen

TU Delft, supervisor



DEPARTMENT OF CIVIL ENGINEERING AND GEOSCIENCES

SECTION, GEO-ENGINEERING

TU DELFT

February 2018

Abstract

Cyclic behaviour of soil has stimulated researchers for several decades to develop constitutive models that will be able to make accurate predictions of soil behaviour and at the same time they will be simple to use. Constitutive models are considered to be more valid compared to empirical models, because they comprise equations that have actual physical meaning. Bounding surface plasticity theory is widely used by researchers and one of the most well-known models is SANISAND, established by Dafalias and Manzari (2004), which is the base for the model presented in this work.

The development of offshore industry during last years, have created the need for models that will be able to simulate soil behaviour under high-cyclic loading, since models like SANISAND were not able to capture the actual number of cycles until liquefaction. This can be done with the incorporation of an additional surface in multi-axial space; the memory surface, which keeps track of the stress history of soil, following the work of Corti (2016).

In this thesis the validation of a new, multiple-surface model, that combines the aforementioned theories, was done. This was achieved by using the data base of Wichtmann and Triantafyllidis (2016), who conducted extensive laboratory testing for sand. This database includes monotonic and cyclic tests for sand under a variety of loading conditions and relative densities. Furthermore, this model was used in order to produce cyclic contour diagrams. These diagrams are practical tools that are often used in practice from offshore foundation designers and they can be constructed using a collection of undrained cyclic tests, either triaxial or DSS.

Acknowledgements

This thesis could not have reached its purpose without the active involvement of many people. First of all, I would like to deeply thank Federico Pisano for his guidance and the fruitful discussions we had throughout the conduction of this research. Realisation of the thesis would not be possible without his advices. Another important person to successfully finish my master thesis project is Haoyuan Liu, Ph.D. student of Geo-engineering section, who developed the new model presented here. I warmly thank him, since he was always helpful with the testing of the model and its deeper understanding. I would like, also, to express my gratitude to Prof. Cristina Jommi and Dr. van Dalen, who accepted to be part of the committee.

In addition, I could not have accomplished my studies, let alone this thesis, without the love and support from my family. Finally, I would like to thank my girlfriend and my friends for their encouragement during last months.

Fotios Iason Zygounas

Delft, February, 2018

Contents

1. INTRODUCTION	1
1.1 BACKGROUND	1
1.2 RESEARCH QUESTIONS.....	3
1.3 STRUCTURE OF THE THESIS.....	3
2. LITERATURE REVIEW	5
2.1 UNDRAINED RESPONSE OF SAND	5
2.1.1 Cyclic behaviour of sand.....	5
2.1.2 Cyclic contour diagrams	8
2.2 MODELING UNDRAINED SAND BEHAVIOUR	10
2.2.1 Empirical modeling	10
2.2.2 Constitutive modeling	12
3. PERFORMANCE OF MODELS.....	19
3.1 EMPIRICAL MODELS.....	19
3.1.1 Seed model.....	19
3.1.2 GMP model.....	20
3.1.2 Ivcic – PWP model.....	22
3.2 SANISAND	24
4. THREE-SURFACE PLASTICITY MODELING	27
4.1 MATHEMATICAL FORMULATION OF THE MODEL.....	27
4.1.1 Elastic relations	27
4.1.2 Yield criterion.....	28
4.1.3 Flow rule	29
4.1.4 Yield surface evolution	30
4.1.5 Memory surface evolution.....	31
4.2 CALIBRATION OF PARAMETERS.....	33
5. RESULTS.....	35
5.1 EXPERIMENTAL TESTS	35
5.2 MONOTONIC PERFORMANCE	36
5.3 CYCLIC PERFORMANCE OF THE MODEL	39
5.3.1 Tests with symmetric loading.....	39
5.3.2 Tests with asymmetric loading	43
5.3.3 Influence of cyclic parameters.....	47

5.3 CYCLIC CONTOUR DIAGRAMS	49
6. CONCLUSIONS-RECOMMENDATIONS.....	53
6.1 CONCLUDING REMARKS.....	53
6.2 FUTURE RESEARCH.....	54
BIBLIOGRAPHY	55
APPENDIX A.....	61
RESULTS FOR MONOTONIC AND CYCLIC TESTS	61

List of figures

Figure 1.1: Increase of offshore wind capacity during 1993-2015 in Europe.....	1
Figure 1.2: Example of constructing a contour diagram for clay (DSS tests).....	2
Figure 2.1: Karlsruhe fine sand response from Wichtmann and Triantafyllidis (2016); Testing conditions: Isotropic, $e_0=0.956$, $p_0=200$ kPa and $q^{amp}/p_0=0.15$	5
Figure 2.2: Karlsruhe fine sand response from Wichtmann and Triantafyllidis (2016); Testing conditions: Isotropic, $e_0=0.800$, $p_0=200$ kPa and $q^{amp}/p_0=0.30$	6
Figure 2.3: Representation of Phase Transformation Line in q-p space.....	7
Figure 2.4: Possible cyclic loading conditions.....	7
Figure 2.5: Example of a three dimensional strain contour diagram derived from undrained triaxial tests on clay (from Sturm et al., 2012).	9
Figure 2.6: Permanent pore pressure contours as a function of loading cycles and cyclic shear stress. Results refer to triaxial tests on dense sand (from Andersen, 2015).....	9
Figure 2.7: Dissipated energy per unit volume of soil (from Green et al., 2001)	11
Figure 2.8: Representation of the yield surface in the stress space.....	13
Figure 2.9: Isotropic (a) and kinematic (b) hardening (from Muransky et al., 2012)	14
Figure 2.10: Illustration of the state parameter concept and the undrained path for sand denser than critical (point a) and looser than critical (point b).	15
Figure 2.11: SANISAND model adapted by Manzari and Dafalias (1997).....	16
Figure 2.12: SANISAND model with closed yield surfaces. Figure from Taiebat and Dafalias (2008), pg. 920.....	16
Figure 2.13: Memory (or history) surface by Stallebrass and Taylor (1997).....	17
Figure 3.1: Comparison of pore pressure development for loose sand between Seed model and experimental results. Testing conditions: Isotropic, $e_0=0.952$, $p_0=200$ kPa and $q^{amp}/p_0=0.15$	19
Figure 3.2: Comparison of pore pressure development for medium dense sand between Seed model and experimental results. Testing conditions: Isotropic, $e_0=0.821$, $p_0=100$ kPa and $q^{amp}/p_0=0.20$	20
Figure 3.3: Comparison of pore pressure development for dense sand between Seed model and experimental results. Testing conditions: Isotropic, $e_0=0.744$, $p_0=300$ kPa and $q^{amp}/p_0=0.30$	Error! Bookmark not defined.
Figure 3.4: Comparison of pore pressure development for loose sand between GMP model and experimental results. Testing conditions: Isotropic, $e_0=0.952$, $p_0=200$ kPa and $q^{amp}/p_0=0.15$	21
Figure 3.5: Comparison of pore pressure development for medium dense sand between GMP model and experimental results. Testing conditions: Isotropic, $e_0=0.821$, $p_0=100$ kPa and $q^{amp}/p_0=0.20$	21
Figure 3.6: Comparison of pore pressure development for dense sand between GMP model and experimental results. Testing conditions: Isotropic, $e_0=0.744$, $p_0=300$ kPa and $q^{amp}/p_0=0.30$	22
Figure 3.7: Cyclic resistance curves for loose, medium dense and dense sand according to Ivcic model.....	22

Figure 3.8: Comparison of pore pressure development for loose sand between GMP model and experimental results. Testing conditions: Isotropic, $e_0=0.952$, $p_0=200$ kPa and $q^{amp}/p_0=0.15$	23
Figure 3.9: Comparison of pore pressure development for medium dense sand between PWP model and experimental results. Testing conditions: Isotropic, $e_0=0.821$, $p_0=100$ kPa and $q^{amp}/p_0=0.20$	23
Figure 3.10: Comparison of pore pressure development for dense sand between GMP model and experimental results. Testing conditions: Isotropic, $e_0=0.744$, $p_0=300$ kPa and $q^{amp}/p_0=0.30$	24
Figure 3.11: Comparison of SANISAND model to the experimental results for loose sand. Testing conditions: Isotropic, $e_0=0.956$, $p_0=200$ kPa and $q^{amp}/p_0=0.15$	24
Figure 3.12: Comparison of SANISAND model to the experimental results for medium dense sand. Testing conditions: Isotropic, $e_0=0.843$, $p_0=200$ kPa and $q^{amp}/p_0=0.20$	25
Figure 3.13: Comparison of SANISAND model to the experimental results for dense sand. Testing conditions: Isotropic, $e_0=0.755$, $p_0=200$ kPa and $q^{amp}/p_0=0.30$	25
Figure 3.14: Pore pressure buildup vs. number of cycles of SANISAND model compared to the experimental results for the sand in figure Figure 3.11.	26
Figure 3.15: Pore pressure buildup vs. cycle ratio of SANISAND model compared to the experimental results for the sand in Figure 3.11.	26
Figure 4.1: The model surfaces	29
Figure 4.2: Defined distance for dilatancy coefficient.....	30
Figure 4.3: Contraction mechanism of memory surface.	32
Figure 4.4: Expansion mechanism of memory surface	32
Figure 5.1: Performance of new model (red line) vs. experimental results (black line) for TMU1.....	36
Figure 5.2: Performance of new model (red line) vs. experimental results (black line) for TMU2.....	36
Figure 5.3: Performance of new model (red line) vs. experimental results (black line) for TMU-AP2.....	37
Figure 5.4: Performance of new model (red line) vs. experimental results (black line) for TMU-AP3.....	37
Figure 5.5: Performance of new model (red line) vs. experimental results (black line) for TMU7.....	38
Figure 5.6: Performance of new model (red line) vs. experimental results (black line) for TMU11.	38
Figure 5.7: Performance of new model (red line) vs. experimental results (black line) for TMD2.....	38
Figure 5.8: Performance of new model (red line) vs. experimental results (black line) for TMD8.....	39

Figure 5.9: Performance of new model (red line) vs. experimental results (black line) for TMD24.	39
Figure 5.10: Stress path of loose sand (TCUI1). Red line refers to the new model and black line to the experimental results.	39
Figure 5.11: Stress path of medium dense sand (TCUI7). Red line refers to the new model and black line to the experimental results.....	40
Figure 5.12: Stress path of dense sand (TCUI17). Red line refers to the new model and black line to the experimental results.	40
Figure 5.13: Stress-strain response of loose sand (TCUI1). Red line refers to the new model and black line to the experimental results.....	41
Figure 5.14: Stress-strain response of medium dense sand (TCUI7). Red line refers to the new model and black line to the experimental results.....	41
Figure 5.15: Pore water pressure accumulation for TCUI12. Optimal value of $\mu_0 = 92$	42
Figure 5.16: Pore water pressure accumulation for TCUI17. Optimal value of $\mu_0 = 92.5$	43
Figure 5.17: Pore water pressure accumulation for TCUI22. Optimal value of $\mu_0 = 87.2$	43
Figure 5.18: Stress path for TCUA4 (a) Experimental results, (b) New model.	44
Figure 5.19: Pore water pressure accumulation for TCUA4. Optimal values: $\mu_0=100$, $\beta=26.5$	45
Figure 5.20: Stress-strain response for TCUA4 (a) Experimental results, (b) New model.	45
Figure 5.21: Pore water pressure accumulation for TCUA2.....	46
Figure 5.22: Pore water pressure accumulation for TCUA3. Optimal values: $\mu_0=350$, $\beta=19$	46
Figure 5.23: Stress path for TCUA19 (a) Experimental results, (b) New model.....	46
Figure 5.24: Pore water pressure accumulation for TCUA19. Optimal values: $\mu_0=150$, $\beta=32$	47
Figure 5.25: Influence of μ_0 on TCUI12.....	47
Figure 5.26: Influence of ζ on TCUI12.	48
Figure 5.27: Influence of β on TCUI12.....	48
Figure 5.28: Influence of μ_0 on TCUA4.	48
Figure 5.29: Influence of β on TCUA4.....	49
Figure 5.30: Pore pressure contour diagram for medium dense sand. Results from triaxial results, $\tau_{av}/p_0'=0$, $p_0'=200$ kPa, without drained precycle.	49
Figure 5.31: Pore pressure contour diagram for medium dense sand. Results from triaxial results, $\tau_{av}/p_0'=0.3$, $p_0'=200$ kPa, without drained precycle.....	50
Figure 5.32: Pore pressure contours for medium dense sand. Results from triaxial results, $\tau_{av}/p_0'=0.25$, $p_0'=250$ kPa (from Andersen, 2015).	50
Figure 5.33: Pore pressure contours as a function of average and cyclic shear stresses for triaxial tests on medium dense sand. The upper figure refers to 10 loading cycles and the lower to 100 cycles.	51
Figure 5.34: Permanent pore pressure for given number of cycles. Triaxial tests on medium dense sand (from Andersen, 2015).	52
Figure 1: TMD3.....	61

Figure 2: TMD5	61
Figure 3: TMD6	61
Figure 4: TMD7	62
Figure 5: TMD9	62
Figure 6: TMD10	62
Figure 7: TMD11	62
Figure 8: TMD12	63
Figure 9: TMD13	63
Figure 10: TMD14.....	63
Figure 11: TMD15.....	63
Figure 12: TMD16.....	64
Figure 13: TMD17.....	64
Figure 14: TMD18.....	64
Figure 15: TMD19.....	64
Figure 16: TMD20.....	65
Figure 17: TMD21.....	65
Figure 18: TMD22.....	65
Figure 19: TMD23.....	65
Figure 20: TMD25.....	66
Figure 21: TMU3	66
Figure 22: TMU4	66
Figure 23: TMU6	66
Figure 24: TMU8	67
Figure 25: TMU10.....	67
Figure 26: TMU12.....	67
Figure 27: TCUI5.....	68
Figure 28: TCUI6.....	68
Figure 29: TCUI8.....	68
Figure 30: TCUI9.....	69
Figure 31: TCUI11	69
Figure 32: TCUI14	68
Figure 33: TCUI15	70
Figure 34: TCUI18	70
Figure 35: TCUI21	70
Figure 36: TCUA4	71
Figure 37: TCUA5	71
Figure 38: TCUA9	70
Figure 39: TCUA10.....	72
Figure 40: TCUA11.....	72
Figure 41: TCUA14.....	72

List of tables

Table 1: Parameters of Seed model.....	19
Table 2: Parameters of Ivicic model	22
Table 3: Parameters of PWP model.....	23
Table 4 Model parameters	33
Table 5: Tests used for validation of new model.....	35
Table 6 Proposed values of monotonic parameters	36
Table 7: Optimum values of μ_0 for each test.....	41
Table 8: Cyclic parameters for different density states of sand	42
Table 9: Optimum values of μ_0 and β for tests of asymmetric loading	43
Table 10: Parameters for tests of anisotropic consolidation (medium dense sand).....	44

List of symbols

e =void ratio

e_0 = initial void ratio

e_c =void ratio at critical state

p_0 =initial mean effective stress

q =deviatoric stress (used as shear stress in triaxial tests)

q^{ampl} =amplitude of deviatoric stress

u_p =permanent pore pressure

u_{acc} =accumulated pore pressure (same as u_p)

η_0 =initial stress ratio

N_{ini} =number of loading cycles to initial liquefaction

ε_1 =axial strain

1. INTRODUCTION

1.1 BACKGROUND

Climate change, as well as higher energy demand, have caused a shift to renewable sources of energy, such as solar or wind. It is especially interesting that during the last 15 years offshore wind farms are developed increasingly, as it can be seen in Figure 1.1, since they have been proved more efficient than the corresponding onshore.

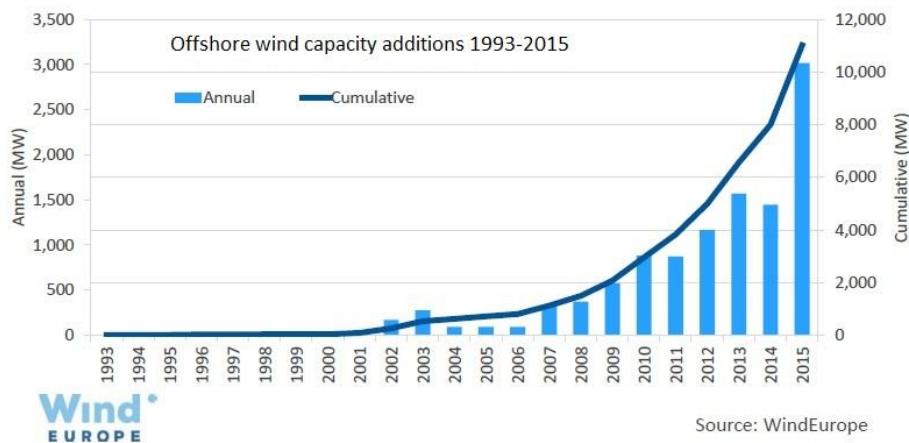


Figure 1.1: Increase of offshore wind capacity during 1993-2015 in Europe.

Further development of offshore wind farms will be ensured with economic design of their foundation, without compromising overall structural integrity. This of course, means that deeper understanding of soil response, especially under cyclic loading, is required. Repeated loading generates excess pore pressure (in partially drained or undrained situations), reduces effective stress and causes accumulation of stresses and/or strains, depending on the boundary conditions (Wichtmann and Triantafyllidis, 2012).

Cyclic soil response has drawn the attention of researchers already from the middle of 20th century, due to failures induced by earthquakes. However, the empirical and constitutive models that have been developed often do not have satisfactory performance under cyclic loading, let alone under high-cyclic loading, which is of special interest for offshore structures. This is due to the significant higher number of cycles from either wave or wind loading. For example, an offshore wind turbine with a lifetime of 25 years has to undergo 10^8 loading cycles (Airey and Fahey, 1991).

A new constitutive model is currently being developed in TU Delft by Liu et al. (2018) for sand. The current thesis validated this model for undrained cyclic conditions, i.e. when water cannot escape pores of soil, and hence there is no

volumetric deformation due to the low compressibility of water. This situation is often encountered in offshore environment, even if usually drainage conditions in sand are considered drained due to its low permeability. Also, in this thesis some empirical models, as well as Sanisand (the model developed by Manzari and Dafalias, in 1997 & 2004, that was basis of the new model), are presented along with their performance.

A problem encountered in practice from foundation designers of offshore structures is that often there is lack of enough available data for a site in the stage of preliminary design. Contour diagram framework offers a chance for designers to conduct feasibility studies with a limited number of site-specific tests (Andersen, 2015). Cyclic contour diagrams can either refer to permanent pore pressure or shear strain that are developed for given cyclic and average shear stresses after certain number of cycles. They are constructed by triaxial and DSS (Direct Simple Shear) test results and each point represents a unique state of a single test. The points with similar level of pore pressure or shear strain are connected. This procedure is illustrated in Figure 1.2. Thus, it can be concluded that it would be extremely useful if a constitutive model combined with a limited number of experimental tests could produce these diagrams and this thesis proved that the new model is capable of doing that.

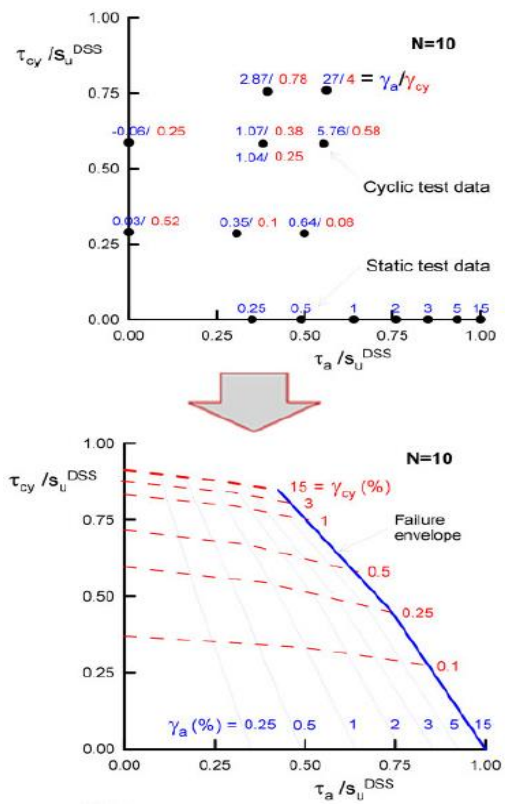


Figure 1.2: Example of constructing a contour diagram for clay (DSS tests)

1.2 RESEARCH QUESTIONS

- Is the new model capable of reproducing the real behaviour of sand under undrained cyclic loading?
- Is the model capable of producing reliable cyclic contour diagrams?

1.3 STRUCTURE OF THE THESIS

The thesis is composed by five chapters.

Chapter 2 presents the behaviour of sand under undrained cyclic conditions, as well as explanation of the concept of cyclic contour diagrams. Also, there is a review of relevant models, both empirical and constitutive.

Chapter 3 provides the performance of older empirical and constitutive models, in order to illustrate their limitations and justify the reason of the current research.

Chapter 4 gives the mathematical formulation of the model that was validated in this thesis. In addition, the calibration strategy of the model parameters is given.

Chapter 5 presents the performance of the new model for monotonic and cyclic loading under undrained conditions. The cyclic contour diagrams constructed with this model are also given.

In chapter 6 the main conclusions are provided and some recommendations for future research, as well.

Finally, in the Appendix all results for monotonic and cyclic tests that were produced are given.

2. LITERATURE REVIEW

This chapter presents a review of the theory and previous research which are relevant to this thesis. At first, the behaviour of sand under undrained cyclic conditions is described, as well as the concept of cyclic contour diagrams. Furthermore, relevant empirical and constitutive models to this thesis are presented.

2.1 UNDRAINED RESPONSE OF SAND

2.1.1 Cyclic behaviour of sand

Undrained conditions occur when the rate of loading is significantly higher than the rate of water drainage. Usually, they are expected in fine soils, but sand can also be susceptible to such conditions, as for example during an earthquake or wave loading (Randolph and Gouvernec, 2011). In the case of undrained loading the volumetric changes in the soil are prevented due to the low compressibility of water. As a result, excess pore pressures will be generated and effective stresses will decrease. This process can lead to liquefaction phenomena in the soil.

Liquefaction is divided into two main categories, according to Kramer (1996); flow liquefaction and cyclic mobility. Flow liquefaction occurs when soil loses its strength and flows like a liquid until the acting shear strength becomes as low as the available strength (Sladen et al., 1985). It is observed that loose samples show this type of failure. In Figure 2.1 an example of liquefaction is given. This figure refers to a triaxial test on loose sand. It can be observed that when mean effective stress (p) shows a sudden decrease, large strains are developed.

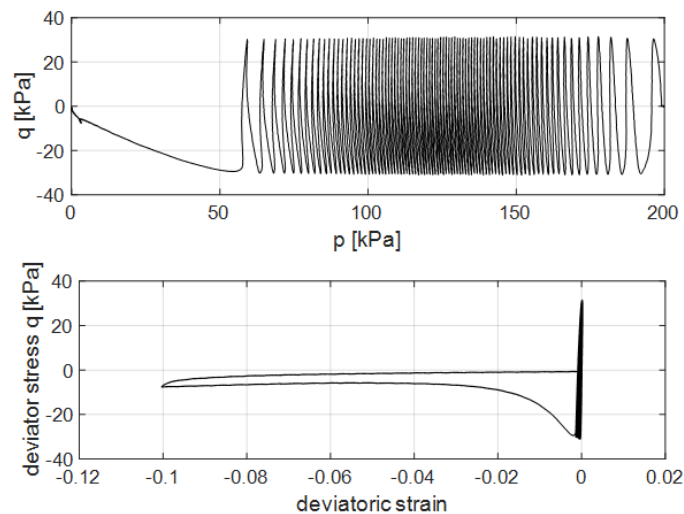


Figure 2.1: Karlsruhe fine sand response from Wichtmann and Triantafyllidis (2016); Testing conditions: Isotropic, $e_0=0.956$, $p_0=200$ kPa and $q^{amp}/p_0=0.15$.

Cyclic mobility on the other hand is the phenomenon when a specimen of saturated sand progressively softens under cyclic loading and after monotonic loading without drainage it stiffens. This occurs because soil tends to dilate and consequently effective stresses increase (Rauch, 1997). In this case development of large shear strains is prevented (Towhata, 2008). Another characteristic of cyclic mobility, as it can be observed from the experimental results of Wichtmann and Triantafyllidis (2016) in Figure 2.2, is that after initial liquefaction ($p=0$ for the first time) there is strain development without mobilization of shear resistance ($q \approx 0$). Also, the characteristic butterfly shape in p - q figure is detected. This type of failure is typical for dense or medium dense sand samples.

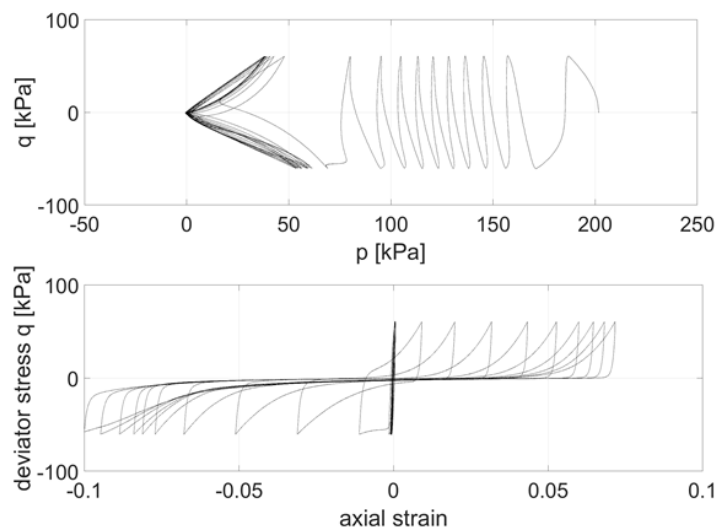


Figure 2.2: Karlsruhe fine sand response from Wichtmann and Triantafyllidis (2016); Testing conditions: Isotropic, $e_0=0.800$, $p_0=200$ kPa and $q^{ampl}/p_0=0.30$.

As stated in Ishihara et al. (1975), there is a locus of stress ratios, shown in Figure 2.3 which defines the transition from contractive to dilative behaviour. Soil density is decisive for the undrained response of sand, as loose sand will experience contractive behaviour and dense sand will tend to dilate (Manzari and Dafalias, 1997). It should be mentioned here that often dense sands show initially a contractive behaviour (Luong, 1982; De Gennaro, 2004).

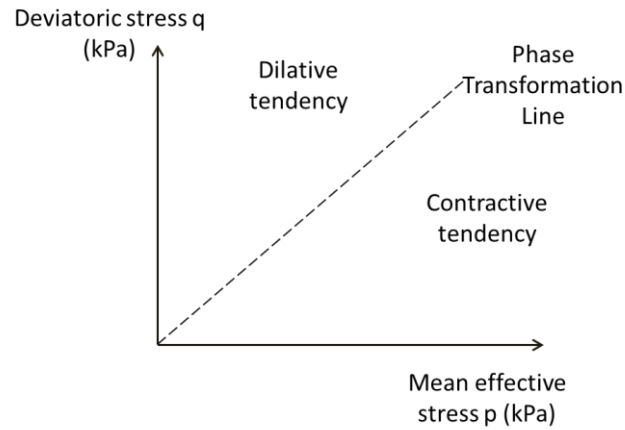


Figure 2.3: Representation of Phase Transformation Line in q-p space.

Regarding the cyclic loading conditions, in Randolph and Gouvernec (2011) four different modes can be distinguished:

- Two way cyclic loading: Shear stress takes positive and negative values.
- One way cyclic loading: Shear stress does not change in sign.
- Symmetric cyclic loading: Specific case of two way loading; average shear stress is zero.
- Asymmetric cyclic loading: Cyclic loading is applied at a non-zero initial shear stress.

These modes are illustrated in Figure 2.4.

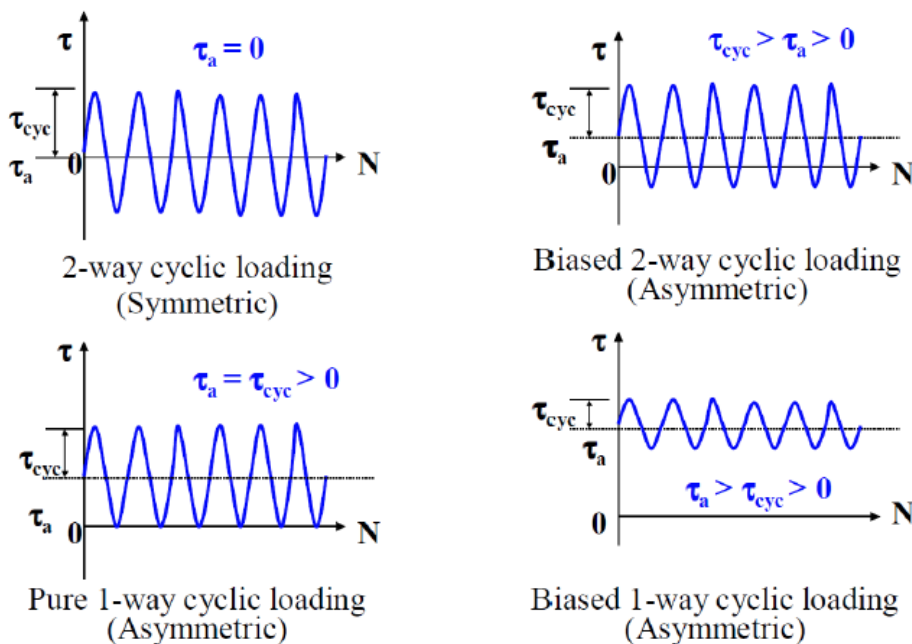


Figure 2.4: Possible cyclic loading conditions

According to De Gennaro et al. (2004), the most critical loading among the above is the two way loading, because of the high strain and pore water pressure accumulation rate.

The most important factors that affect the sand behaviour as it can be observed in various experimental studies (Mao and Fahey 2000; Towhata, 2008; Wichtmann and Triantafyllidis, 2016; Randolph and Gouvernec, 2011) are relative density, cyclic amplitude and mean pressure. It has been already written that relative density affects the mode of failure. The response of sand is also affected by initial mean pressure combined with the cyclic amplitude, as expressed by the ratio q^{amp}/p_0 . For example, from results of Wichtmann and Triantafyllidis it can be seen that greater values of this ratio will give less number of cycles until initial liquefaction. If this ratio is kept constant and initial mean pressure is increased, then the number of cycles will be increased significantly. Another influential factor of sand behaviour is the average stress. It is confirmed that when cyclic loading is symmetric the development of axial strain and pore pressure is quicker (De Gennaro, 2004, Wichtmann and Triantafyllidis, 2016).

2.1.2 Cyclic contour diagrams

The concept of contour diagrams was first presented by Andersen et al. (1988) and Andersen and Lauritzen (1988) and they have been used in practice for many years now. The contour diagrams are derived either by undrained triaxial tests or Direct Simple Shear (DSS) tests (Sturm et al., 2012). In Figure 2.5 an example of such a diagram is presented. On the main axes of this diagram the normalized average and cyclic stress and the number of loading cycles. The contour lines that are approximately parallel to the vertical axis refer to average shear strain, while the other lines refer to cyclic strain. In the introduction, the strategy to construct such a diagram has been presented. When contour diagram refers to clay, the shear stresses (cyclic or average) are normalized to the undrained static shear strength. On the other hand, for sand it is common to normalize the shear stresses to the vertical effective normal stress.

Pore pressure contour diagrams can also be established, in the same manner as the corresponding strain diagrams. In Figure 2.6 a typical example of this type is provided.

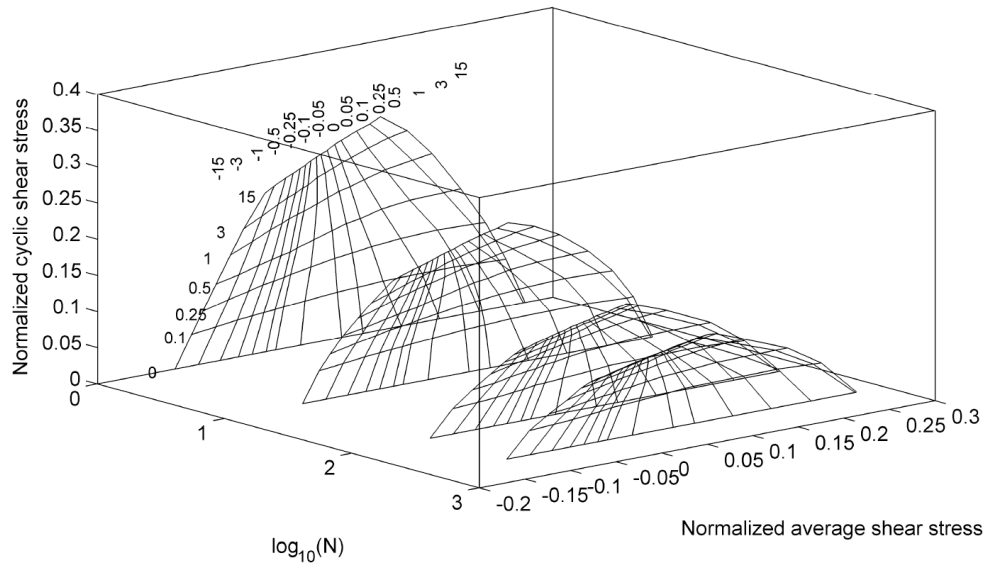


Figure 2.5: Example of a three dimensional strain contour diagram derived from undrained triaxial tests on clay (from Sturm et al., 2012).

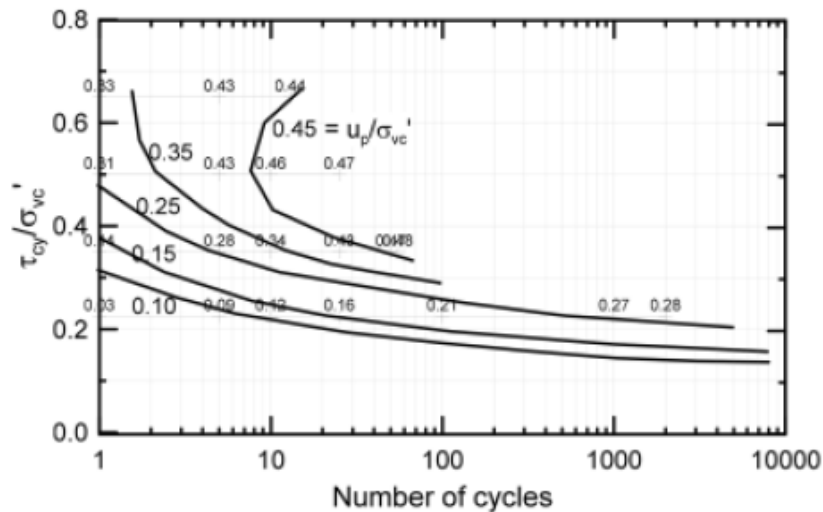


Figure 2.6: Permanent pore pressure contours as a function of loading cycles and cyclic shear stress. Results refer to triaxial tests on dense sand (from Andersen, 2015).

Cyclic contour diagrams is a practical tool which can be used by foundation designers of offshore projects during a feasibility study when there is not enough data available. Of course, they cannot substitute the site specific tests, but they can reduce their number and therefore contribute to the decrease of the final cost of an offshore structure. Another important remark is that these diagrams can be constructed using tests with constant shear stresses. However, real load histories will be irregular. This can be solved by transforming real load histories into equivalent number of cycles with constant shear stress. For example, Andersen (2015) discusses an example of such a transform.

2.2 MODELING UNDRAINED SAND BEHAVIOUR

In this section the available models for sand, which are relevant to this thesis, are presented. Two main categories are presented here; the empirical and the constitutive models. There is also the category of discrete element models, but the characteristics and limitations of this technique were not suitable for this project.

2.2.1 Empirical modeling

Usually empirical equations for sand focus on the pore pressure buildup. This is expressed through the pore pressure ratio (r_u), which is defined as the ratio between the residual excess pore pressure to the initial effective confinement stress ($r_u = u_p / p_0'$). There is a vast number of models that correlate parameters from CPT and SPT tests or earthquake magnitude with the development of excess pore pressure (Rauch, 1998 from Youd, 2001, Robertson and Wride, 1998, Andrus and Stokoe, 1997, 2000 among others). However, the interest of the current thesis lies into models that predict the liquefaction potential of sand based only on Stress Ratio (SR), which is defined as the ratio between the average shear stress to the initial confinement stress ($SR = \tau_{av} / p_0'$). The majority of the models predict pore pressure buildup as a function of the cycle ratio, i.e. the ratio between the number of the applied uniform loading cycles (N) and the number of cycles required to cause liquefaction (N_l). This is considered as an important drawback of these models, since the results will not be representative of the real soil behaviour. For example, if sand will not liquefy these equations cannot be applied. This implies an additional problem of empirical models, which is the limited loading conditions where they can be applied. One of the earliest models of this type was developed by Seed et al. (1975), using data from tests on clean sands:

$$r_u = 0.5 + \frac{1}{\pi} \arcsin\left(2\left(\frac{N}{N_l}\right)^{1/\alpha} - 1\right) \quad (2.1)$$

where α is a fitting parameter.

Booker et al. (1976) proposed a simplified version of Seed's model:

$$r_u = \frac{2}{\pi} \arcsin\left(\frac{N}{N_l}\right)^{1/2\alpha} \quad (2.2)$$

The equations 2.1 and 2.2 are identical in shape, so both will be denoted as Seed model in this thesis.

Polito et al. (2008) presented a correlation for the calculation of α , which is dependent on the fines content, relative density and cyclic stress ratio:

$$\alpha = c_1 FC + c_2 I_{D0} + c_3 SR + c_4 \quad (2.3)$$

In equation 2.3 the parameters $c_1 - c_4$ are coefficients that come after statistical analysis of many cyclic triaxial tests, while FC is the fines content (in percent), I_{D0} the relative density (also in percent) and SR the stress ratio. The coefficients have two different possible values each; one value for FC less than 35% and another for FC greater than 35%.

Green et al. (2000) developed the GMP model, which relates the pore pressure ratio with the energy dissipated per unit volume of soil (W_s), which for undrained triaxial tests is the area of the stress-strain hysteresis loops as it is shown in Figure 2.7. The mathematical expression of this model is the following:

$$r_u = \sqrt{\frac{W_s}{PEC}} \leq 1 \quad (2.4)$$

The term PEC is called “pseudoenergy” capacity and is calculated from:

$$PEC = \frac{W_{s,r_u=0.65}}{0.4225} \quad (2.5)$$

where $W_{s,r_u=0.65}$ is the value of W_s when r_u becomes 0.65. Polito et al. (2008) gave correlation for PEC, which was not used in this thesis, though.

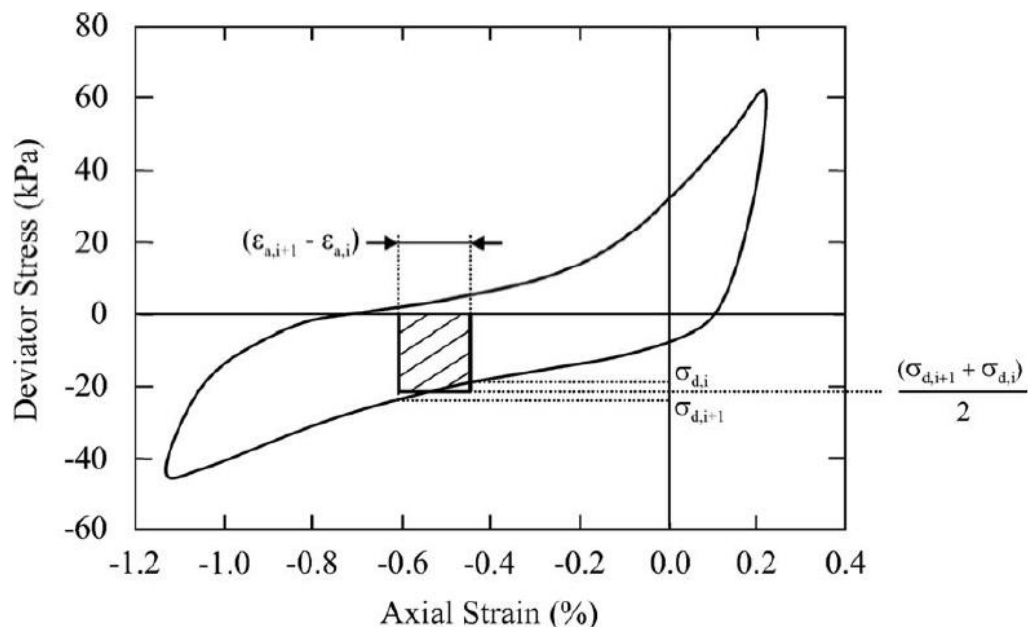


Figure 2.7: Dissipated energy per unit volume of soil (from Green et al., 2001)

The first model which predicted the number of cycles to liquefaction as a function of stress ratio only, was developed by Ivšić (2006). In this model the concept of

damage parameter was used, which was first presented by Finn and Bhatia (1982). Damage parameter contains parameters that describe the strain or stress history and for stress controlled tests is given by equation 2.6:

$$\kappa = 4N(SR - SR_t)^\alpha \quad (2.6)$$

where SR_t is the stress ratio below which no excess pore pressure is generated and α is a fitting parameter. Polito et al. (2008) mention that it is common to estimate the SR needed to cause liquefaction in 15 cycles (SR_r in equation 2.7) and correlate the number of equivalent cycles for the actual applied SR. As a result, Ivšić can be expressed as it is shown in equation 2.7:

$$\frac{(SR - SR_t)}{(SR_r - SR_t)} = \left(\frac{15}{N}\right)^{\frac{1}{\alpha}} \quad (2.7)$$

Using equations 2.6 and 2.7 it is possible to calculate the maximum value for the damage parameter at liquefaction.

$$\kappa_L = 60(SR_r - SR_t)^\alpha \quad (2.8)$$

Chiaradonna et al. (2015) proposed the PWP model to estimate the pore pressure build up as a function of the damage parameter.

$$r_u = a \left(\frac{\kappa}{\kappa_L}\right)^b + c \left(\frac{\kappa}{\kappa_L}\right)^4 \quad (2.9)$$

where a , b and c are fitting parameters.

2.2.2 Constitutive modeling

Constitutive models offer researchers an opportunity to link the experimentally observed behaviour of sands with equations which have proper physical meaning. The need for accuracy as well as the complexity of soil behaviour often leads to complex models with a big number of parameters which sometimes may not have proper physical meaning. The "four ingredients" framework (Muir Wood, 2004) can provide a possible solution to overcome this problem. These ingredients are summarized as follows:

- Elastic properties: The elastic properties describe the elastic behaviour of soil, i.e. when the deformations are recoverable and the strain increment is proportional to the stress increment. Elastic stiffness of sand depends on the stress state and void ratio.
- Yield criterion: The yield surface distinguishes the elastic from the plastic state, i.e. if yield criterion is not met, only elastic deformations are being

developed. A possible example of the yield surface is shown in Figure 2.8, while mathematically it is expressed as:

$$f(\underline{\sigma}) = 0 \quad (2.10)$$

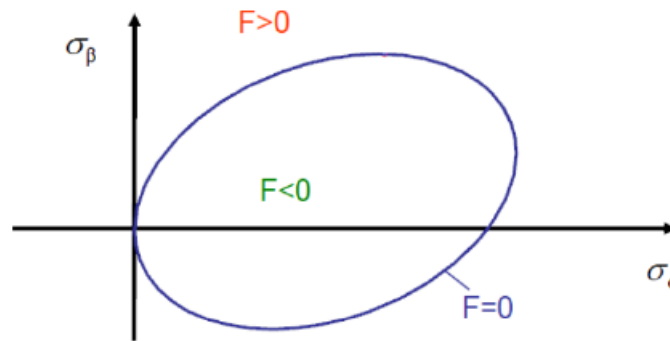


Figure 2.8: Representation of the yield surface in the stress space.

- Flow rule: Once the stress state satisfies equation 2.10 plastic deformations will occur. The development of these deformations is determined with the flow rule, which has the following mathematical expression:

$$d\epsilon_{pl} = d\lambda \frac{dg}{d\underline{\sigma}} \quad (2.11)$$

where $d\lambda$ is a positive scalar and g is the plastic potential, that may or may not be the same as the yield surface. The flow rule is then called associated and non-associated respectively.

- Hardening rule: The hardening rule links the non-linear stress-strain response with a possible translation (kinematic hardening) or expansion (isotropic hardening) of the yield surface. The graphical representation of these two is shown in Figure 2.9.

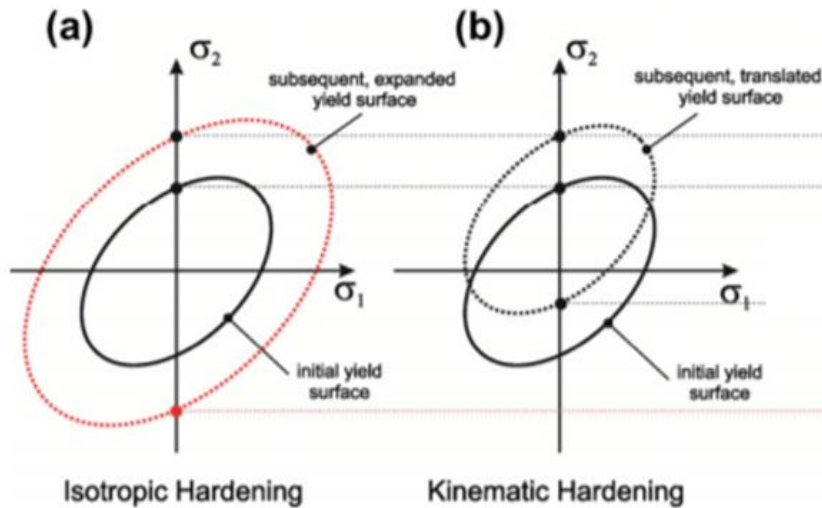


Figure 2.9: Isotropic (a) and kinematic (b) hardening (from Muransky et al., 2012)

2.2.2.1 Bounding surface plasticity models

Bounding surface theory is a widely adopted theory that describes both metal and soil behaviour. Dafalias and Popov (1975) and Krieg (1975) were the first that developed it in parallel. This theory states that there is one surface that in the stress space always encloses the loading surface. The full mathematical development of this theory was done by Dafalias (1986).

Dafalias and Popov (1975) observed that distance between bounding and loading surface as well as the plastic work done by the material affect the plastic stiffness. Mroz et al. (1978) based on these conclusions linked the evolution of the plastic stiffness to the distance between the two surfaces. Finally, Bardet (1986) showed the influence of the Phase Transformation Line and, by extension, of the relative density, on the soil behaviour.

2.2.2.2 Critical state framework

Casagrande (1936; 1938) was the first that introduced the concept of a “critical” void ratio. Roscoe et al. (1958) developed the critical state theory, which is one basic component of the present model. The fundamental concept of this theory is that soil will reach a state, where “soil continues to deform at constant stress and constant void ratio” (Roscoe et al., 1958). The distance of a sand from this critical (or reference) state defines the current state of the sand. The measurement of this distance is possible by introducing the state parameter ψ as defined by Been and Jefferies (1985):

$$\psi = e - e_c \quad (2.12)$$

Wood et al. (1994) related the peak stress ratio and the state parameter providing thus a solid basis, whereupon reliable constitutive models can be built. The concept

of the state parameter can provide solution to problems arising in models such as Bardet's (1986) that treated loose and dense sands as different materials. In Figure 2.10 the concept of the state parameter is presented, in the $e-\ln(p)$ space. When initial void ratio is less than critical, soil is considered as dense (point a) and in undrained conditions (no change in volume, therefore no change in void ratio) it will first move at point a_d . This is done because of the initial contractive tendency, which causes development of positive pore water pressure and thus the effective stress (p) is reduced. Afterwards, soil will tend to dilate and point a will move to point a_c on the critical state line where it fails. Correspondingly, for a state looser than critical, point b will move to b_c where it fails. Often it can also reach b_d before turning back to b_c (Manzari and Dafalias, 1997).

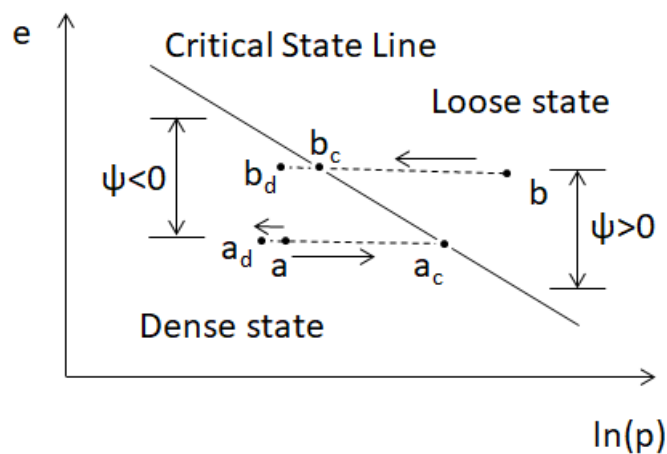


Figure 2.10: Illustration of the state parameter concept and the undrained path for sand denser than critical (point a) and looser than critical (point b).

The state parameter was then implemented in various models. In this project only SANISAND (Manzari and Dafalias, 1997) is presented, since it is the basis for the new model. SANISAND is a two surface model, as it is shown in Figure 2.11. The yield surface is considered as an open wedge in the stress space. Plastic stiffness depends on the distance between the center of the yield surface and a conjugate point on the bounding surface. There are two additional surfaces that distinguish the contractive from the dilative tendency. More specifically, when stress ratio ($\eta = q / p$) is above a^d then dilation occurs, while if it is above M and at the same time $\psi > 0$ then soil contracts.

the so-called memory (or history) surface. Stallebrass and Taylor (1997) proposed first this additional surface, which was kinematic. Other similar models were developed by Jafarzadeh et al. (2008), Maleki et al. (2009) and Di Benedetto et al. (2014).

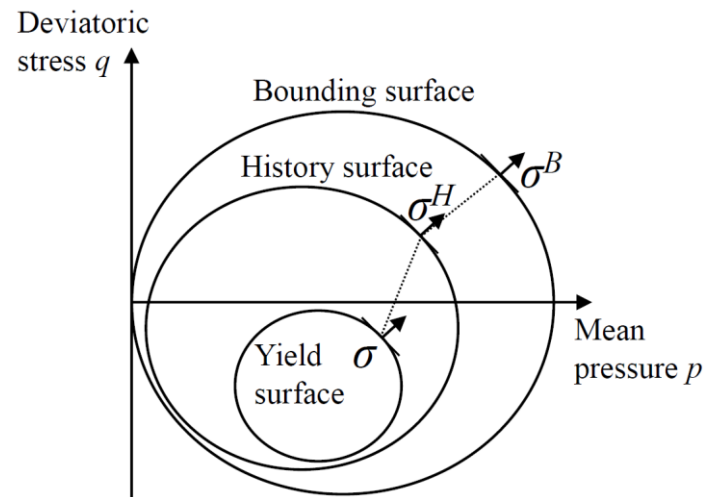


Figure 2.13: Memory (or history) surface by Stallebrass and Taylor (1997)

Corti (2016) unlike older models introduced a surface which can evolve in both size and position and combined it successfully with a bounding surface plasticity model for sand. Corti (2016) expressed two rules that describe the evolution of the memory surface:

- Rule 1: The current yield surface is always inside the memory surface, i.e. the yield surface is the minimum size of the memory surface.
- Rule 2: The memory surface changes in size because of the experienced plastic strains. More specifically, it expands when sand contracts and it decreases in size when sand dilates.

3. PERFORMANCE OF MODELS

In this chapter the performance of previous model is presented. The models are compared to experimental results from Wichtmann and Triantafyllidis (2016) in terms of pore pressure development. Three different tests were selected; one for loose, one for medium dense and one for dense samples. In chapter 5 more details about this database can be found.

3.1 EMPIRICAL MODELS

3.1.1 Seed model

The performance of Seed model is shown in figures Figure 3.1-Figure 3.3. The sand of these tests has practically zero FC and SR is also zero. So, equation 2.3 is reduced to $\alpha = c_2 I_{D0} + c_4$. In Table 1 the parameters used for Seed model are shown.

Table 1: Parameters of Seed model

	I_{D0}	c_2	c_4
Loose sand	27	0.007397	0.5058
Medium dense sand	62		
Dense sand	82		

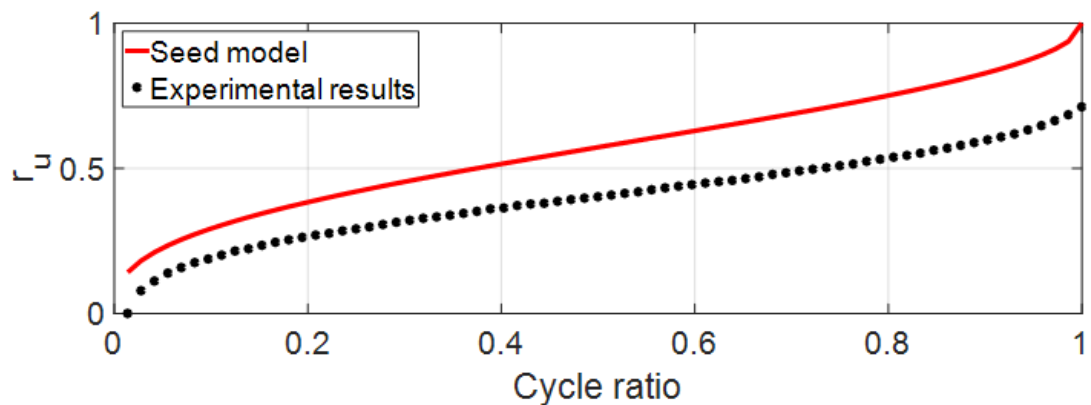


Figure 3.1: Comparison of pore pressure development for loose sand between Seed model and experimental results. Testing conditions: Isotropic, $e_0=0.952$, $p_0=200$ kPa and $q^{amp}/p_0=0.15$.

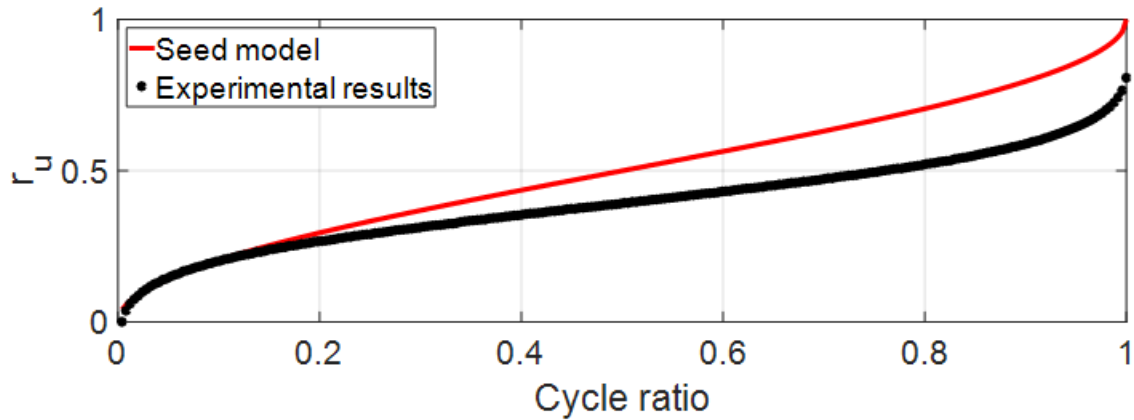


Figure 3.2: Comparison of pore pressure development for medium dense sand between Seed model and experimental results. Testing conditions: Isotropic, $e_0=0.821$, $p_0=100$ kPa and $q^{amp}/p_0=0.20$.

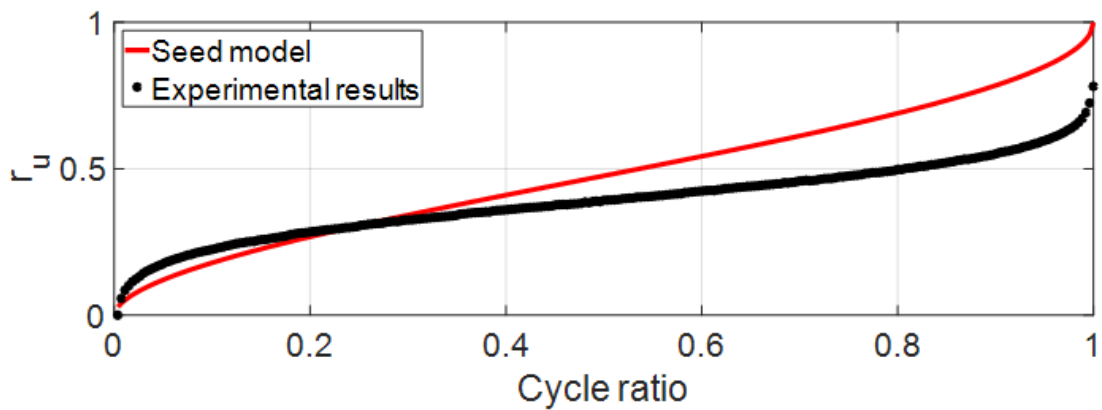


Figure 3.3: Comparison of pore pressure development for dense sand between Seed model and experimental results. Testing conditions: Isotropic, $e_0=0.744$, $p_0=300$ kPa and $q^{amp}/p_0=0.30$.

As it can be seen in the previous figures the performance of the Seed model is satisfactory. However, the drawback of this model is that it cannot be used for coupled dynamic numerical analysis (Polito et al., 2008), because number of cycles to liquefaction is defined a priori (Park et al., 2014). Also, this model, as well as the other empirical models presented in this chapter, cannot be used for cases where the mean effective pressure does not reach zero (i.e. no liquefaction present). Finally, the use of cycle ratio (N / N_i) is questionable, since it does not reproduce the real soil behaviour. This will be explained better in section 3.2.

3.1.2 GMP model

In Figures Figure 3.4-Figure 3.6 the performance of GMP model is shown. In order to compare straightforward this model with Seed model, cycle ratio is selected as the x-

axis. However, more often ratio W_s / W_s^{liq} is used. The performance of GMP model seems to be better than Seed model. The advantage over Seed model is that it can be used in time-domain analysis program (Park et al., 2015). However, GMP model is also impossible to use for cases where there is no liquefaction. Furthermore, Park et al. (2014) note that it cannot be used to simulate dense sand with strong dilative tendency.

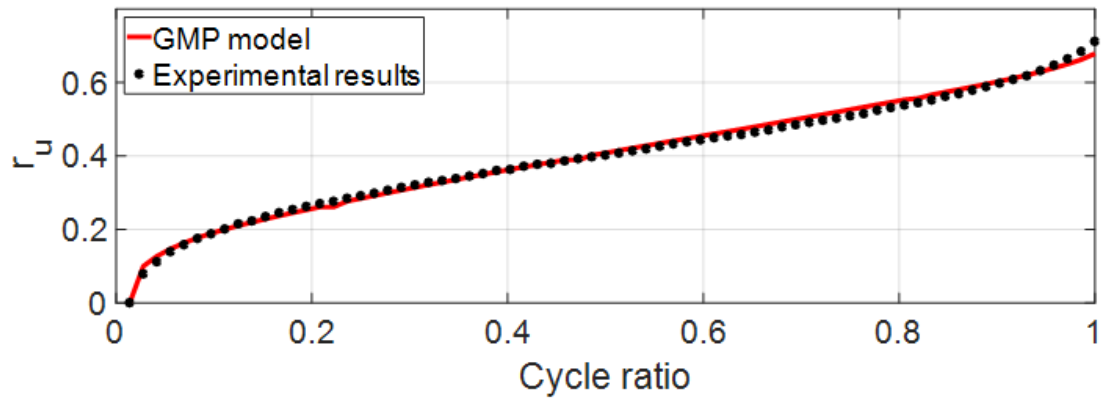


Figure 3.4: Comparison of pore pressure development for loose sand between GMP model and experimental results. Testing conditions: Isotropic, $e_0=0.952$, $p_0=200$ kPa and $q^{amp}/p_0=0.15$.

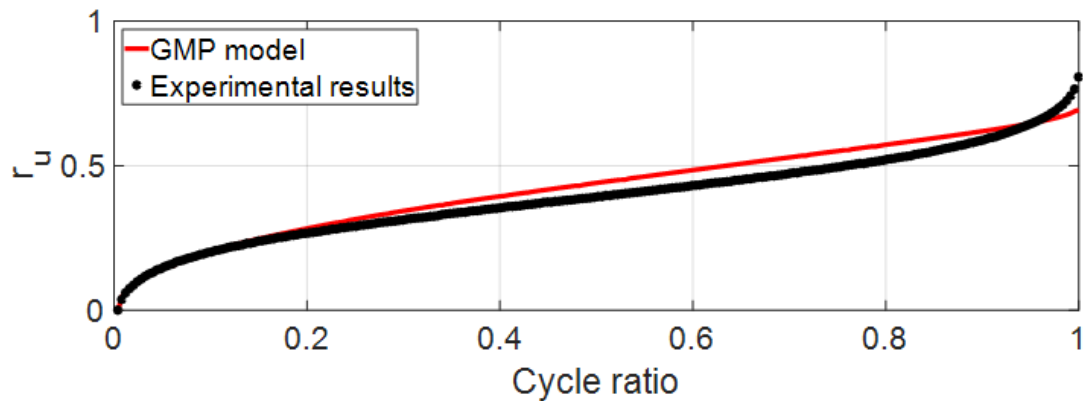


Figure 3.5: Comparison of pore pressure development for medium dense sand between GMP model and experimental results. Testing conditions: Isotropic, $e_0=0.821$, $p_0=100$ kPa and $q^{amp}/p_0=0.20$.

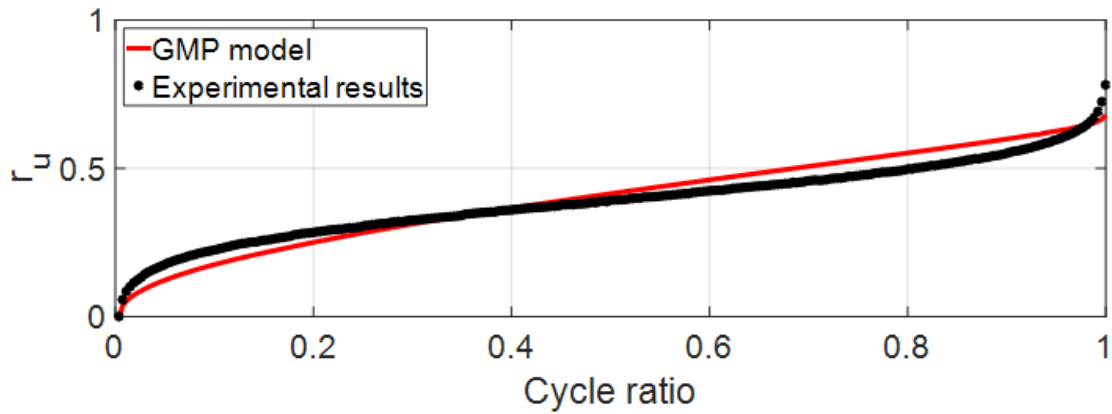


Figure 3.6: Comparison of pore pressure development for dense sand between GMP model and experimental results. Testing conditions: Isotropic, $e_0=0.744$, $p_0=300$ kPa and $q^{amp}/p_0=0.30$.

3.1.2 Ivicic - PWP model

In Figure 3.7 the results of Ivicic model are provided. It was especially convenient that there were available test results for cases of 15 cycles, so equation 2.7 was used ($(SR - SR_t) / (SR_r - SR_t) = (15 / N)^\alpha$). The parameters of this model are given in Table 2. It can be observed that the parameters are material dependent, since they have higher values for denser sands.

Table 2: Parameters of Ivicic model

Density	SR_t	α	SR_r
Loose	0.065	1.81	0.1
Medium dense	0.079	2.54	0.15
Dense	0.085	3.9	0.2

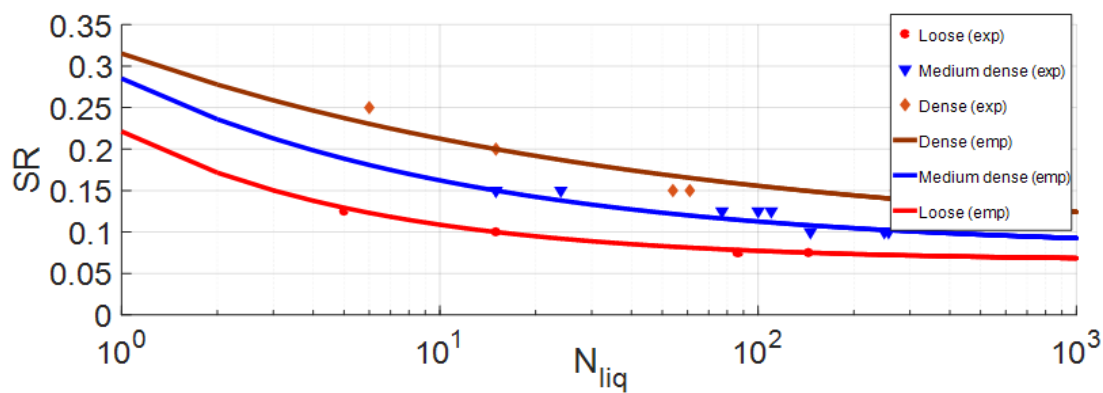


Figure 3.7: Cyclic resistance curves for loose, medium dense and dense sand according to Ivicic model

Regarding PWP model, it was possible to use only one set of parameters for all tests. The calibrated values can be found in Table 3.

Table 3: Parameters of PWP model

Parameter	a	b	c
Value	0.5	0.55	0.2

In Figures Figure 3.8-Figure 3.10 the performance of PWP is shown.

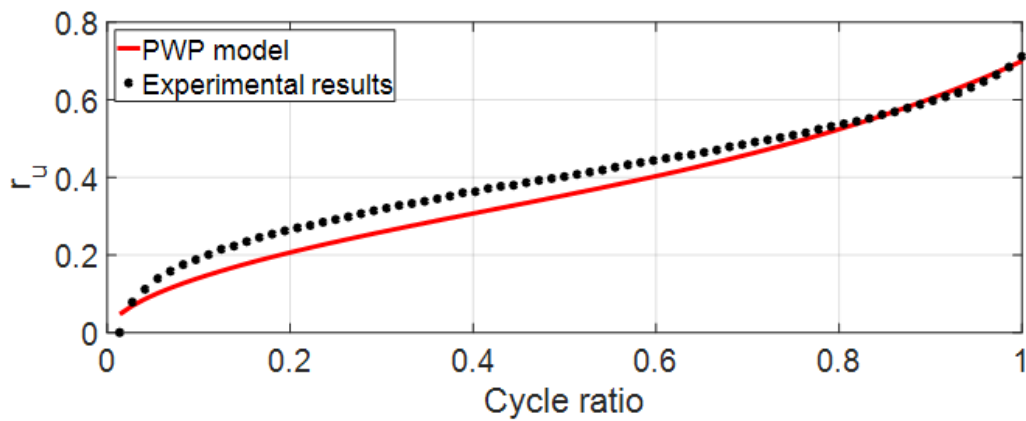


Figure 3.8: Comparison of pore pressure development for loose sand between GMP model and experimental results. Testing conditions: Isotropic, $e_0=0.952$, $p_0=200$ kPa and $q^{amp}/p_0=0.15$.

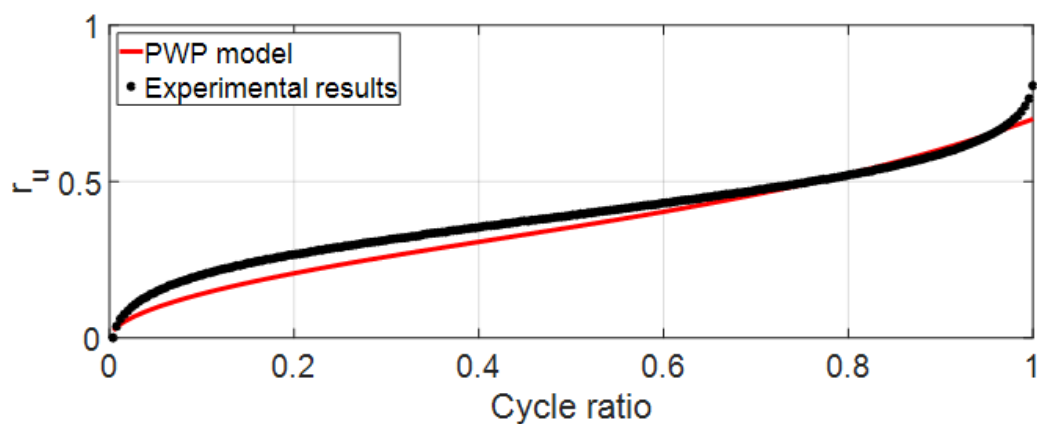


Figure 3.9: Comparison of pore pressure development for medium dense sand between PWP model and experimental results. Testing conditions: Isotropic, $e_0=0.821$, $p_0=100$ kPa and $q^{amp}/p_0=0.20$.

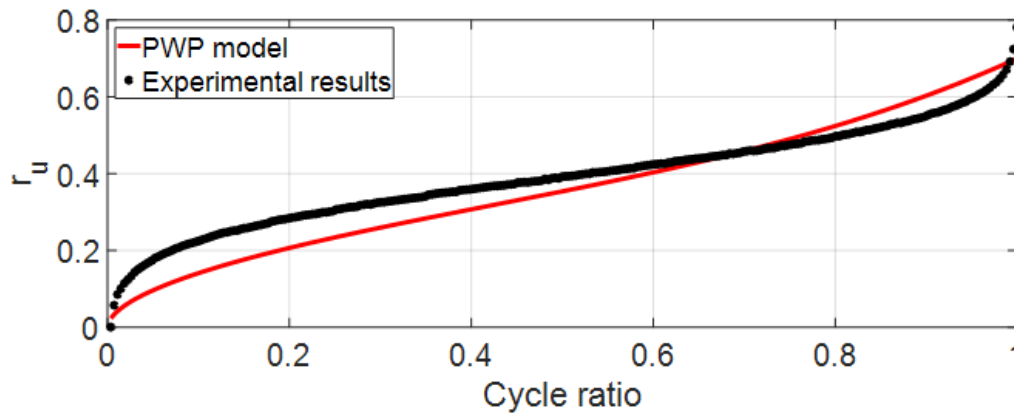


Figure 3.10: Comparison of pore pressure development for dense sand between GMP model and experimental results. Testing conditions: Isotropic, $e_0=0.744$, $p_0=300$ kPa and $q^{amp}/p_0=0.30$.

3.2 SANISAND

The complete mathematical formulation of Sanisand is not given in this thesis. However, the equations are similar to those of the new model, except for some modifications that account for the influence of the memory surface. The monotonic parameters were the same as the new model and their values are shown in the 5th chapter. Regarding the cyclic parameters of this model (they refer to fabric changes of sand), it was found that their influence on the final results was not important.

The performance of SANISAND is provided in Figures Figure 3.11-Figure 3.13. It is apparent that high-cyclic loading cannot be simulated realistically with this model. More specifically, it seems that SANISAND will always fail after 10 cycles or less. Also, butterfly shape will always be produced even though loose samples do not show this behaviour.

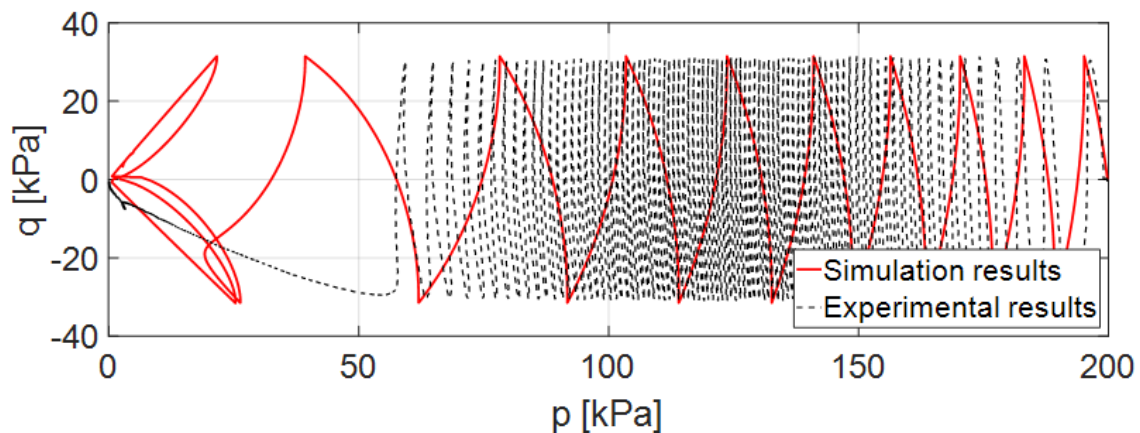


Figure 3.11: Comparison of SANISAND model to the experimental results for loose sand. Testing conditions: Isotropic, $e_0=0.956$, $p_0=200$ kPa and $q^{amp}/p_0=0.15$.

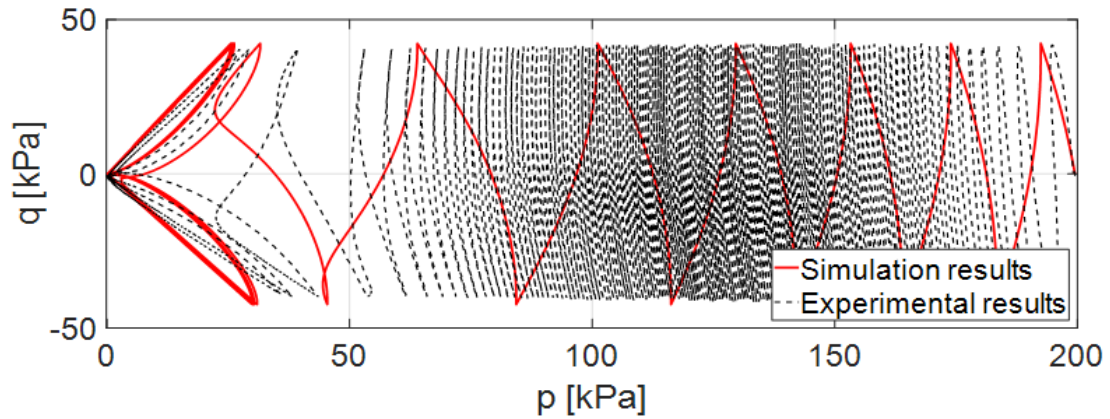


Figure 3.12: Comparison of SANISAND model to the experimental results for medium dense sand. Testing conditions: Testing conditions: Isotropic, $e_0=0.843$, $p_0=200$ kPa and $q^{amp}/p_0=0.20$.

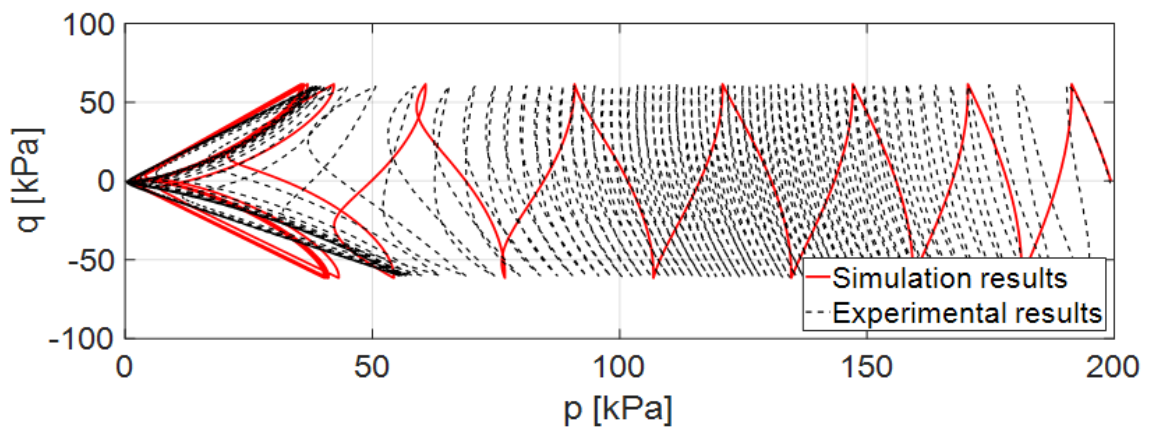


Figure 3.13: Comparison of SANISAND model to the experimental results for dense sand. Testing conditions: Testing conditions: Isotropic, $e_0=0.755$, $p_0=200$ kPa and $q^{amp}/p_0=0.30$.

In section 3.1.1 it was stated that use of cycle ratio is questionable. This is justified by Figures Figure 3.14 and Figure 3.15. In these figures it is shown that even though SANISAND predicts much less cycles than the actual number of cycles to liquefaction, if cycle ratio is used, this model gives satisfactory results.

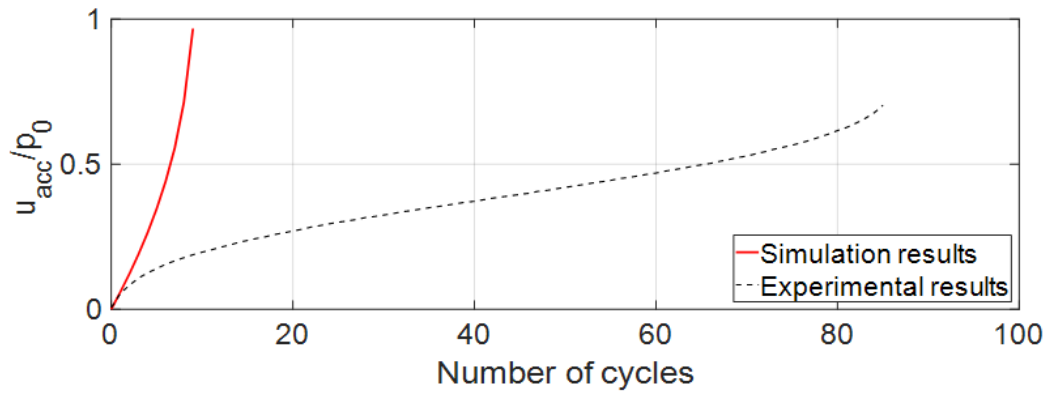


Figure 3.14: Pore pressure buildup vs. number of cycles of SANISAND model compared to the experimental results for the sand in figure Figure 3.11.

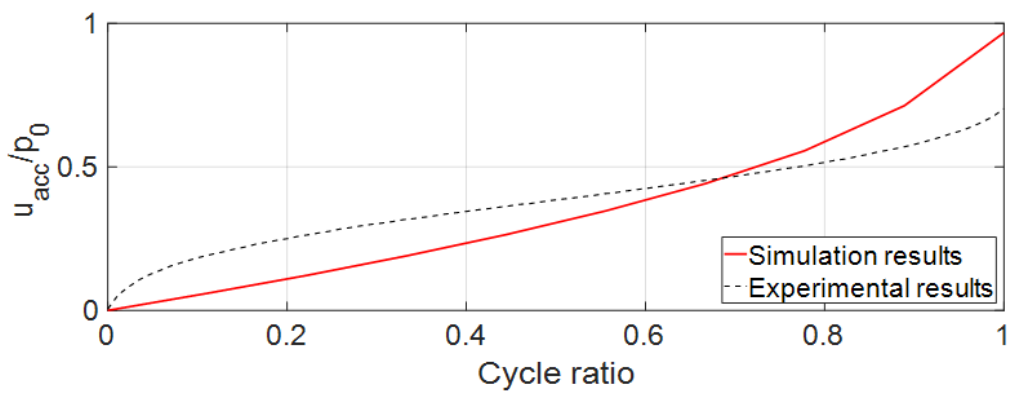


Figure 3.15: Pore pressure buildup vs. cycle ratio of SANISAND model compared to the experimental results for the sand in Figure 3.11.

4. THREE-SURFACE PLASTICITY MODELING

In this chapter the new model which was calibrated and used for the construction of cyclic contour diagrams, will be presented. The second order tensors are written in bold. The stress and strain tensors are denoted as $\boldsymbol{\sigma}$ and $\boldsymbol{\varepsilon}$ respectively. Both tensors comprise by two parts; the deviatoric and isotropic. The model has three surfaces in multi-axial space; the yield, bounding and memory surface. Also there are two more surfaces the dilatancy and critical surface which distinguish the dilative and contractive behaviour of sand. The complete mathematical formulation of the model can be found in Liu et al. (2018).

4.1 MATHEMATICAL FORMULATION OF THE MODEL

4.1.1 Elastic relations

The elastic behaviour of sand is described through hypoelasticity equations. More specifically, the elastic strain and the volumetric strain increment are given from equations 4.1 and 4.2:

$$d\mathbf{e}^e = d\mathbf{s} / 2G \quad (4.1)$$

$$d\varepsilon_v^e = dp / K \quad (4.2)$$

In equation 4.1 \mathbf{e} is the deviatoric strain tensor and \mathbf{s} the corresponding stress tensor. The terms ε_v (volumetric strain) and p in 4.2 are the isotropic parts of strain and stress tensors. G and K are the elastic shear modulus and the elastic bulk modulus respectively. The calculation of the moduli is done after Li and Dafalias (2000):

$$G = G_0 p_{atm} \left[\frac{(2.97 - e)^2}{1 + e} \right] \left(\frac{p}{p_{atm}} \right)^{0.5} \quad (4.3)$$

$$K = \frac{2G(1 + \nu)}{3(1 - 2\nu)} \quad (4.4)$$

where G_0 is a material constant, e the void ratio, p the current stress level, p_{atm} the atmospheric pressure, and ν the Poisson's ratio.

4.1.2 Yield criterion

The yield criterion of the model is given from equation 4.5, which in the multi-axial space is a cone shape.

$$f = \sqrt{(\mathbf{s} - p\boldsymbol{\alpha}) : (\mathbf{s} - p\boldsymbol{\alpha})} - \sqrt{\left(\frac{2}{3}\right)} pm = 0 \quad (4.5)$$

The center of the yield surface is the $\boldsymbol{\alpha}$ term of equation 4.5 and it is also found in the literature as the back-stress ratio tensor. The radius of the surface is $\sqrt{\left(\frac{2}{3}\right)}m$.

This surface is characterized by kinematic hardening, thus only $\boldsymbol{\alpha}$ changes and m is constant. The symbol $:$ between two stress tensors denotes the trace of their inner product, i.e. $\mathbf{a} : \mathbf{b} = tr(\mathbf{ab})$. It is often that in equation 4.5 instead of \mathbf{s} and p , deviatoric stress ratio tensor is used: $\mathbf{r} = \mathbf{s} / p$, which represents the current stress state and it lies on the yield surface.

4.1.2.1 Other surfaces

Memory surface

The shape of memory surface is the same as the yield surface, as it can be observed by equation 4.6:

$$f^M = \sqrt{(\mathbf{s} - p\boldsymbol{\alpha}^M) : (\mathbf{s} - p\boldsymbol{\alpha}^M)} - \sqrt{\left(\frac{2}{3}\right)} pm^M = 0 \quad (4.6)$$

The superscript of $\boldsymbol{\alpha}^M$ and m^M indicate that these parameters refer to the memory surface.

Bounding, critical and dilatancy surface

The critical state framework is incorporated as defined by Schofield and Wroth (1968) with M being the critical stress ratio ($M = q_c / p_c$) and q , p are the deviatoric and mean pressure at critical state, respectively. The void ratio at critical state is defined in the following equation (Wang et al., 1990):

$$e_c = e_0 - \lambda_c \left(\frac{p_c}{p_{am}} \right)^\xi \quad (4.7)$$

In equation 4.7 e_0 is the reference void ratio or else the void ratio when $p_c = 0$, while λ_c and ξ are parameters of the model.

The bounding, critical and dilatancy surfaces have the same Argyris shape (Argyris et al., 1974) and they are given by:

$$\mathbf{r}^{b,c,d} = \sqrt{\frac{2}{3}} g(\theta, c) M^{b,c,d} \mathbf{n} \quad (4.8)$$

The term $g(\theta, c)$ is given by:

$$g(\theta, c) = \frac{2c}{(1+c) - (1-c)\cos 3\theta} \quad (4.9)$$

where $c = M_e / M_c$, i.e. the ratio of critical stress ratio in extension (M_e) and compression (M_c). The θ is the Lode angle, while $\mathbf{n} = \frac{\mathbf{r} - \mathbf{a}}{\sqrt{2/3m}}$ and it satisfies the relations $tr\mathbf{n} = 0$ and $tr\mathbf{n}^2 = 1$. Finally, M^b and M^d are given by

$$\begin{aligned} M^b &= M e^{n^b \Psi} \\ M^d &= M e^{-n^d \Psi} \end{aligned} \quad (4.10)$$

where n^b and n^d are model constants. The main surfaces of the model are shown in Figure 4.1.

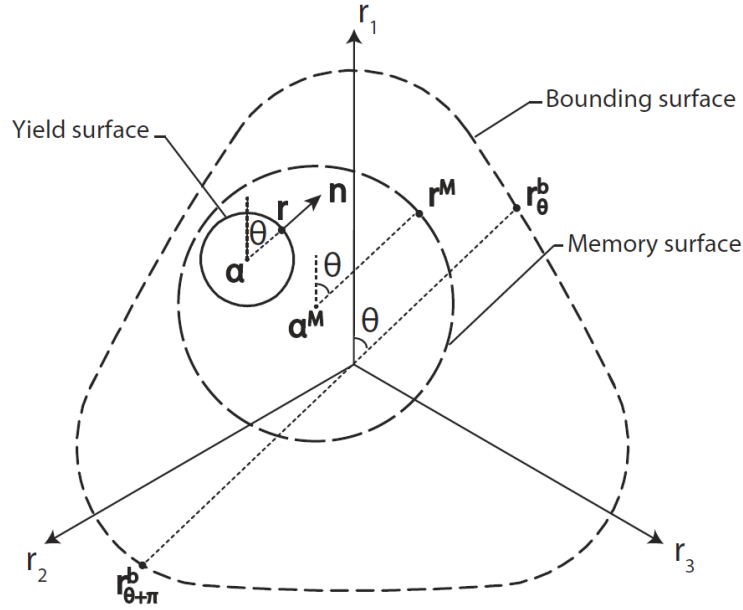


Figure 4.1: The model surfaces (from Liu et al., 2018).

4.1.3 Flow rule

As it has already been mentioned, flow rule describes the development of plastic strains, which in this model the definition of Manzari and Dafalias (1997) is used. The plastic volumetric strain increment is defined as:

$$d\varepsilon_v^p = \langle L \rangle D \quad (4.11)$$

L is the plastic multiplier, depended on the plastic modulus, and D is the dilatancy coefficient in multi-axial space and is given by

$$D = A_d(\mathbf{r}_\theta^d - \mathbf{r}) : \mathbf{n} \quad (4.12)$$

In the previous equation the difference $\mathbf{r}_\theta^d - \mathbf{r}$ represents the distance between yield surface and dilatancy surface. The memory surface is also taken into account in the dilatancy coefficient though A_d :

$$A_d = A_0 \exp\left(\beta \frac{\langle \tilde{b}_d^M \rangle}{b_{ref}}\right) \quad (4.13)$$

where β is a model constant and \tilde{b}_d^M is the distance between memory and dilatancy surface. The adjustment of the flow rule described above is demonstrated in Figure 4.2.

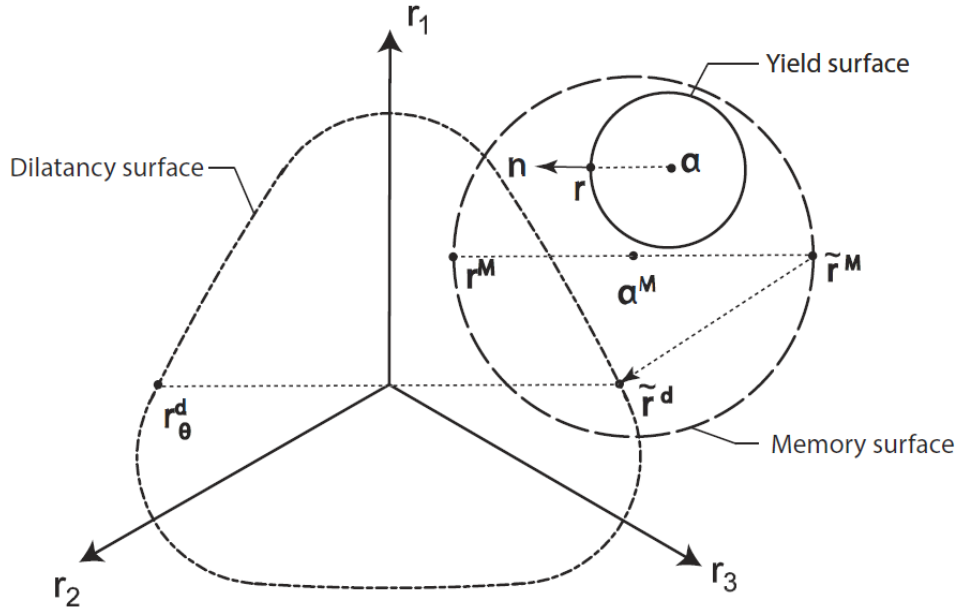


Figure 4.2: Defined distance for dilatancy coefficient (from Liu et al., 2018).

4.1.4 Yield surface evolution

The translation of the yield surface is given by

$$d\alpha = \frac{2}{3} \langle L \rangle h(\mathbf{r}^b - \mathbf{r}) \quad (4.14)$$

The response of the sand is determined by the value of plastic modulus:

$$K_p = \frac{2}{3} p h(\mathbf{r}^b - \mathbf{r}) : \mathbf{n} \quad (4.15)$$

If K_p is >0 , $=0$ or <0 then sand exhibits hardening, failure or softening response respectively.

The hardening modulus h of the previous equation is the hardening modulus and it is calculated as

$$h = \frac{b_0}{(\mathbf{r} - \mathbf{r}_{in}) : \mathbf{n}} e^{\mu(p) \left(\frac{b^M}{b_{ref}} \right)^2} \quad (4.16)$$

Where

$$b_0 = G_0 h_0 (1 - c_h e) \left(\frac{p}{p_{at}} \right)^{-0.5} \quad (4.17)$$

$$\mu(p) = \mu_0 \left(\frac{p}{p_{at}} \right)^{0.5} \quad (4.18)$$

and b_{ref} is a reference distance for normalization. The influence of the memory surface on the hardening modulus is realized with the last equation where μ_0 is a model constant and $\mu(p)$ is considered as confining pressure dependent.

4.1.5 Memory surface evolution

4.1.5.1 Translation of memory surface

Translation of the memory surface is described by an equation similar to the corresponding equation of the yield surface:

$$d\mathbf{a}^M = \frac{2}{3} \langle L^M \rangle h^M (r^b - r^M) \quad (4.19)$$

4.1.5.2 Change of size of memory surface

The size of the memory surface changes according to the following equation:

$$dm^M = \sqrt{\frac{3}{2}} \mathbf{n} : d\mathbf{a}^M - \frac{m^M}{\zeta} \left(1 - \frac{x_1 + x_2}{x_3} \right) \langle -d\varepsilon_v^p \rangle \quad (4.20)$$

When soil experiences dilative behaviour, soil behaves softer, thus it is reasonable to assume that memory surface will contract in this case, in order to indicate the fabric damage and memory loss. This is illustrated in Figure 4.3.

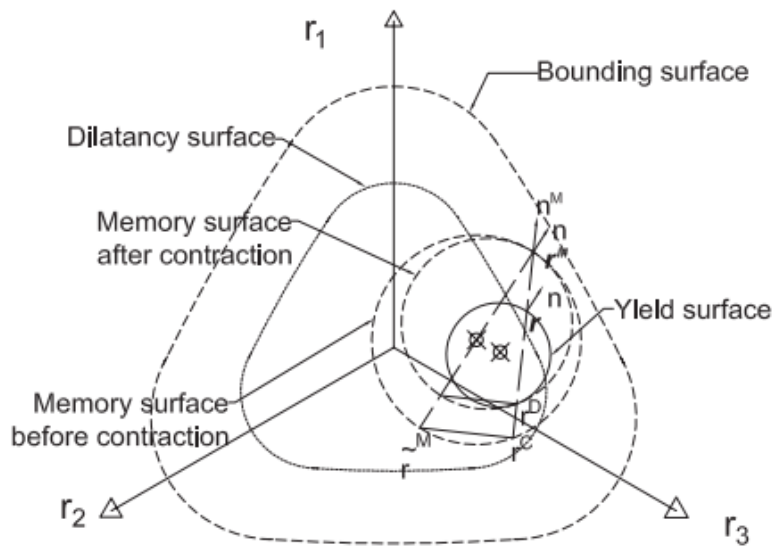


Figure 4.3: Contraction mechanism of memory surface (from Liu et al., 2018).

Correspondingly, when soil contracts, its fabric becomes stronger and memory surface expands. This expansion is described mathematically by equation 4.20 and more specifically with the first part. It is represented in Figure 4.4.

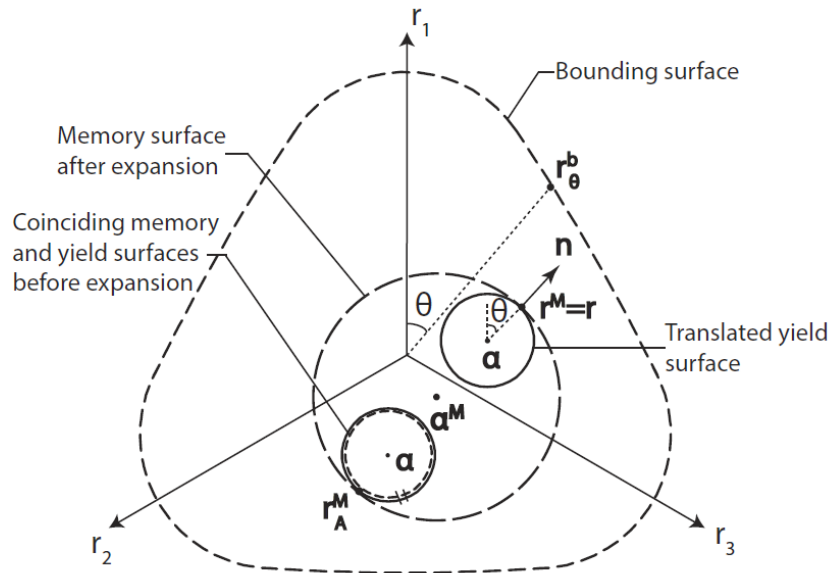


Figure 4.4: Expansion mechanism of memory surface (from Liu et al., 2018).

4.2 CALIBRATION OF PARAMETERS

From the previous chapter it can be concluded that the total number of parameters is 16, i.e. only one additional from the SANISAND as defined in Manzari and Dafalias (2004) and four additional from Corti (2016). In Table 4 all parameters are presented, as well as the recommended calibration strategy.

Table 4 Model parameters

Constant	Variable	Description	Calibration method
Elasticity	G_0	Shear modulus G at $p=p_{atm}$	Stress-strain curve from monotonic triaxial drained or undrained test
	ν	Poisson's ratio	
Critical state	M	Critical stress ratio at compression	Monotonic triaxial tests that reach critical state
	c	Ratio of stress ratios in extension and compression	
	λ_c	Slope of critical state line	
	e_0	Critical void ratio when $p=0$	
	ξ	Model constant	
Yield surface	m	Radius of yield surface	Small number
Plastic modulus	h_0	Model constant	Trial and error
	c_h	Model constant	Trial and error
	n^b	Kinematic hardening parameter to determine bounding surface size	Monotonic drained and undrained tests to get peak ψ and η and then use equation 3.9
Dilatancy	A_0	Dilatancy parameter	Trial and error
	n^d	Dilatancy parameter to determine size of dilatancy surface	Monotonic drained and undrained tests to get ψ and η at phase transformation state and then use equation 3.9
Memory surface	μ_0	Influence of memory surface on plastic modulus and plastic strain	Trial and error
	ζ	Constant that reflects fabric damage	
	β	Constant related to volumetric strain	

5. RESULTS

In this chapter the performance of a new multiple-surface plasticity model is provided. First, the database that was used is presented. Afterwards, the performance of the model for monotonic and cyclic tests is given. Finally, the cyclic contour diagrams that have been produced are presented.

5.1 EXPERIMENTAL TESTS

The new model was validated against triaxial test results from Wichtmann and Triantafyllidis (2016) for sand. In this database there are monotonic drained and undrained compression tests for sand of different relative density. Also, there are some undrained extension tests. In addition, cyclic tests are provided, for cases of zero and non-zero average shear stress. It has to be noted that for triaxial tests, deviatoric stress (i.e. difference of two normal stresses) plays the role of shear stress. In Table 5 the experimental results that will be presented in this chapter are given.

Table 5: Tests used for validation of new model

	Test	e_0 [-]	I_{D0} [-]	p_0 [kPa]	q^{ampl} [kPa]	η_0 [-]	N_{ini} [-]
Monotonic	TMD2	0.996	0.21	100	-	-	-
	TMD8	0.859	0.52	200	-	-	-
	TMD24	0.697	0.95	300	-	-	-
	TMU1	0.828	0.60	100	-	-	-
	TMU2	0.814	0.64	200	-	-	-
	TMU7	0.828	0.60	100	-	-	-
	TMU11	0.964	0.24	200	-	-	-
	TMU-AP2	0.941	0.30	300	-	-	-
	TMU-AP3	0.932	0.32	500	-	-	-
Cyclic	TCUI1	0.952	0.27	200	30	0	72
	TCUI7	0.800	0.67	200	60	0	11
	TCUI12	0.814	0.64	200	50	0	77
	TCUI17	0.726	0.87	200	60	0	185
	TCUI22	0.744	0.82	300	90	0	269
	TCUA2	0.812	0.64	300	120	0.5	-
	TCUA3	0.727	0.87	300	120	0.5	-
	TCUA4	0.816	0.63	300	60	0.5	-
	TCUA19	0.804	0.66	200	40	-0.5	-

TMD stands for Triaxial Monotonic Drained tests

TMU stands for Triaxial Monotonic Undrained tests

TMU-AP stands for Triaxial Monotonic Undrained Air Pluviation tests

TCUI stands for Triaxial Cyclic Undrained Isotropic tests

TCUA stands for Triaxial Cyclic Undrained Anisotropic tests

5.2 MONOTONIC PERFORMANCE

The monotonic performance of the new model is the same as SANISAND. However, it was necessary to calibrate the parameters according to the monotonic tests of Wichtmann and Triantafyllidis (2016), in order to proceed to the cyclic tests of this specific type of sand (Karlsruhe fine sand). The recommended set of parameters is given in Table 6. These values can be considered as reliable, since Wichtmann and Triantafyllidis (2016) provide all the relevant variables needed to calculate most parameters. Therefore, it was possible to calibrate only three parameters using the trial and error method and thus the time of the calibration can be reduced significantly.

Table 6 Proposed values of monotonic parameters

G_0 (kPa)	ν	M	c	λ_c	e_o	ξ	m	h_0	c_h	n^b	A_0	n^d
95	0.05	1.35	0.85	0.056	1.038	0.28	0.01	7.6	1.015	1.2	0.56	2.15

The calibration was first done using the undrained monotonic tests of the available data set. The results for some tests are shown in Figure 5.1 and Figure 5.2. The results can be considered satisfactory.

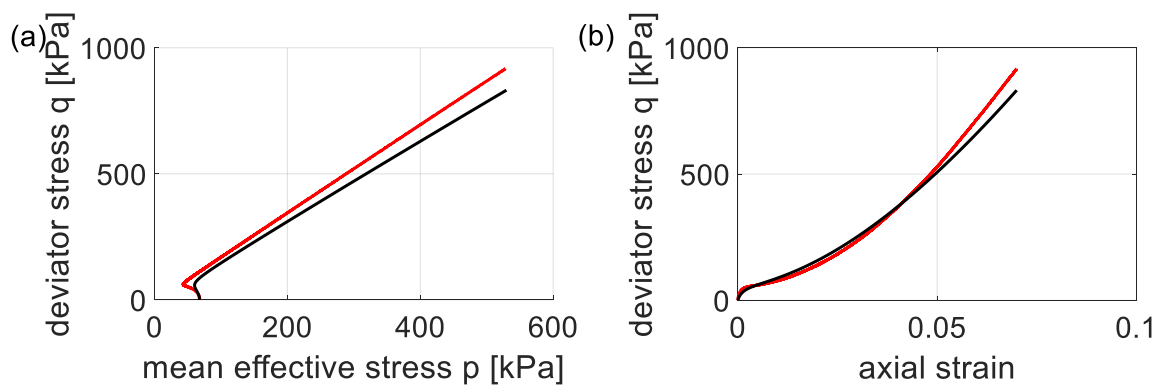


Figure 5.1: Performance of new model (red line) vs. experimental results (black line) for TMU1.

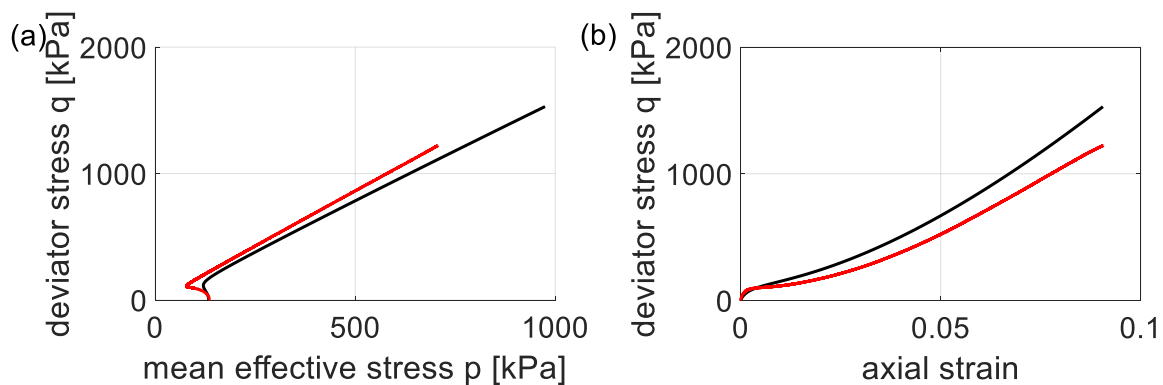


Figure 5.2: Performance of new model (red line) vs. experimental results (black line) for TMU2.

In Figure 5.1 and Figure 5.2 it can be observed that in q-p diagram, the inclination of the line does not coincide with the experimental data. This inclination is controlled from parameter M, which in this case should be smaller. However, this difference is explained since the strains in this case are smaller than Figure 5.3 and Figure 5.4, where it is clear that M is calibrated correctly.

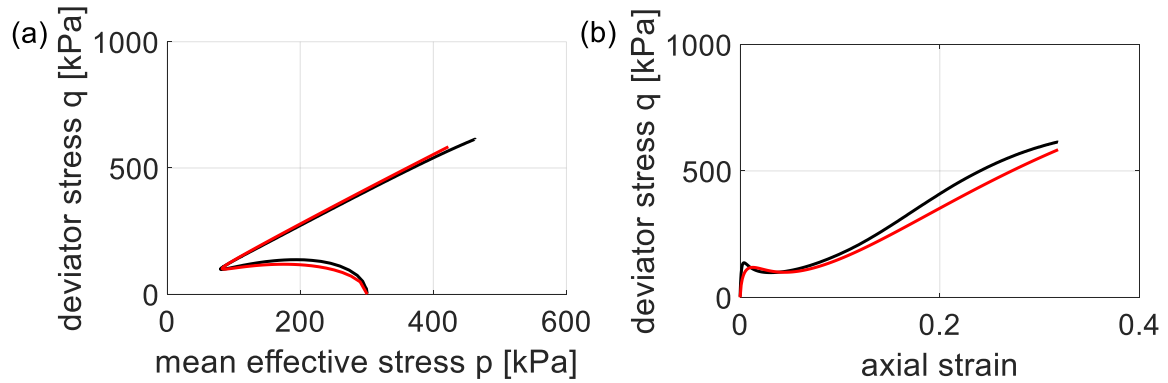


Figure 5.3: Performance of new model (red line) vs. experimental results (black line) for TMU-AP2.

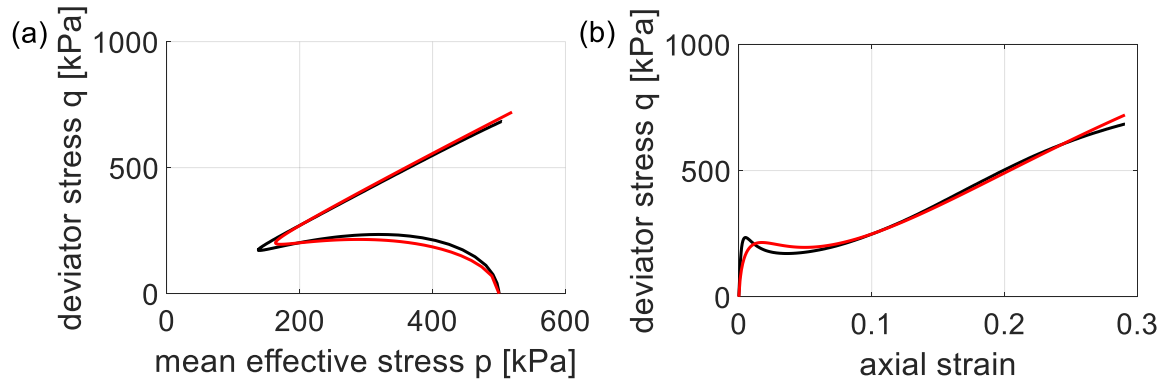


Figure 5.4: Performance of new model (red line) vs. experimental results (black line) for TMU-AP3.

In the same database there are also some extension tests included. However, the model cannot reproduce them satisfactorily as it can be seen in Figure 5.5 and Figure 5.6. A possible reason for this behaviour could be the shape of the bounding surface is smaller for the extension part.

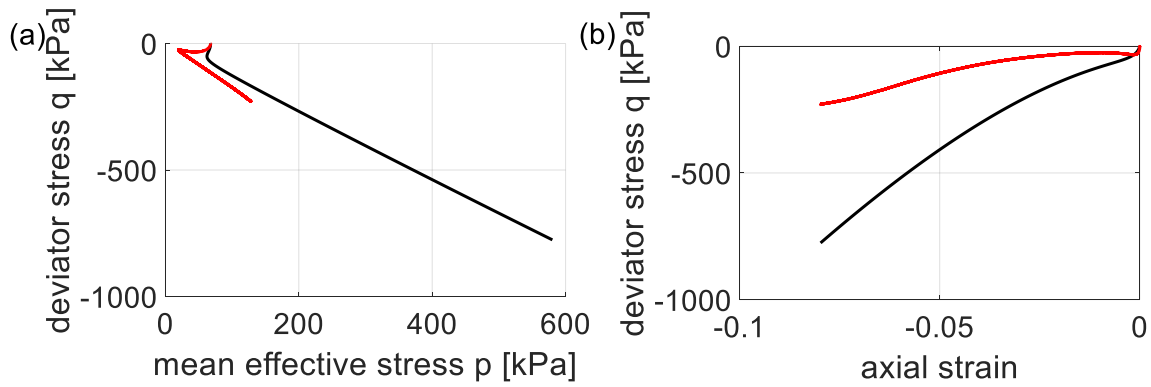


Figure 5.5: Performance of new model (red line) vs. experimental results (black line) for TMU7.

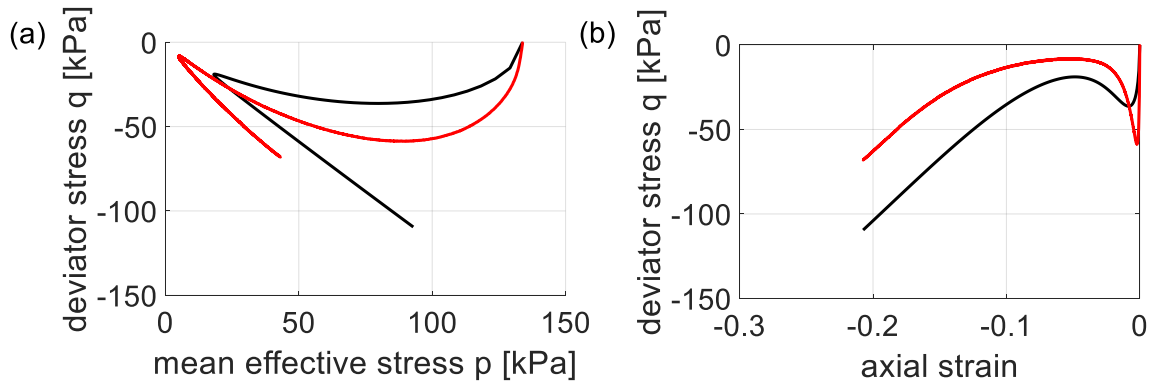


Figure 5.6: Performance of new model (red line) vs. experimental results (black line) for TMU11.

Furthermore, it was considered useful to validate the model for drained monotonic tests of Wichtmann and Triantafyllidis (2016). The results are shown in Figures Figure 5.7-Figure 5.9. It can be observed that the overall performance of the model is very good and only the contractive behaviour of loose samples cannot be reproduced accurately. However, it is safe to conclude that the model and the proposed values of the parameters are acceptable.

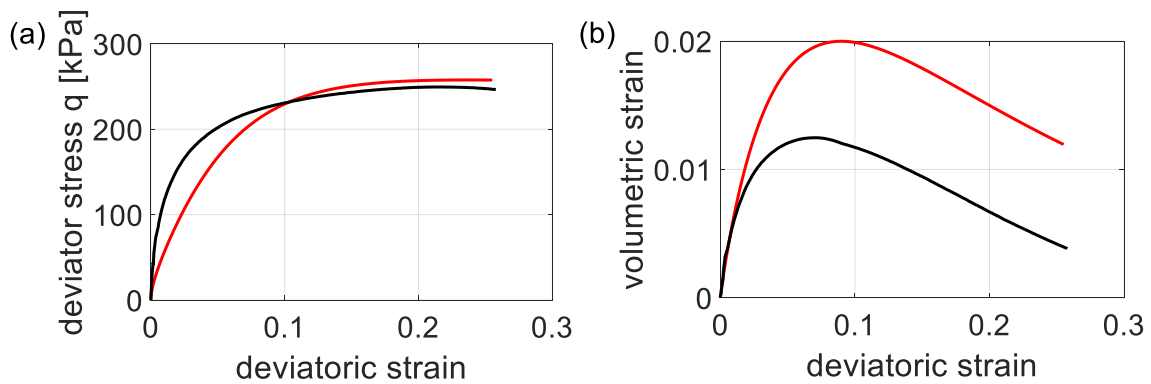


Figure 5.7: Performance of new model (red line) vs. experimental results (black line) for TMD2.

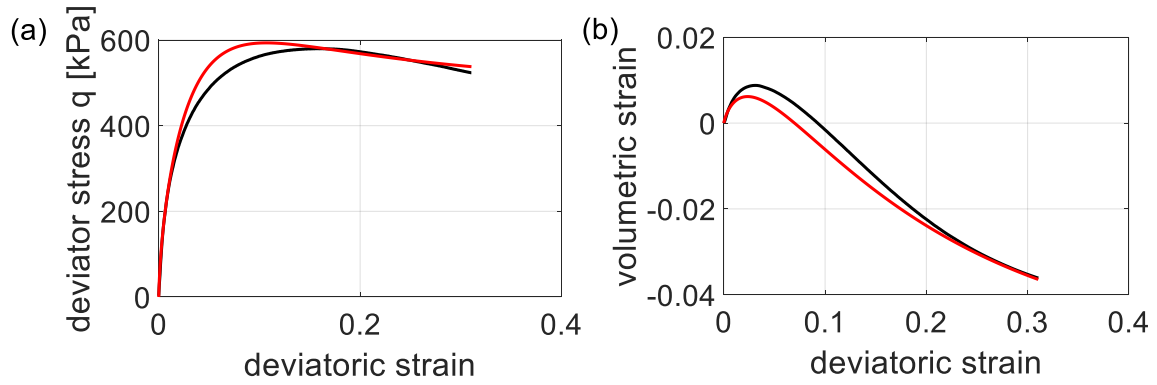


Figure 5.8: Performance of new model (red line) vs. experimental results (black line) for TMD8.

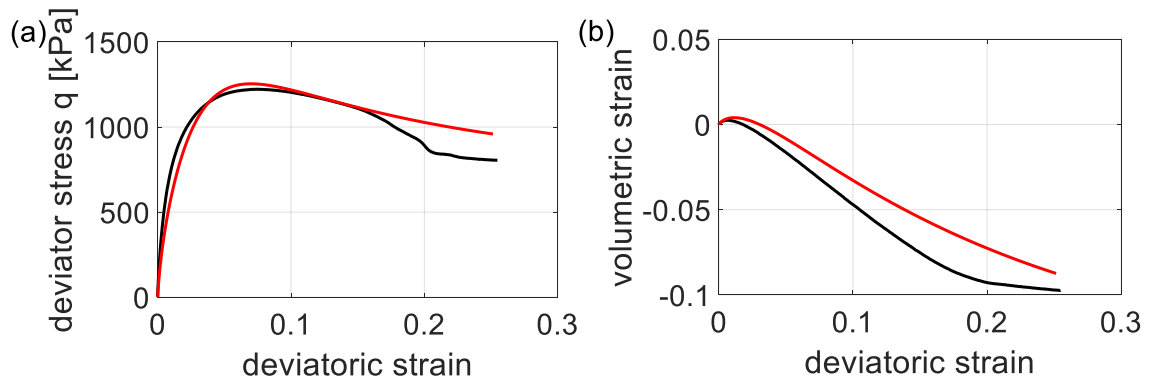


Figure 5.9: Performance of new model (red line) vs. experimental results (black line) for TMD24.

5.3 CYCLIC PERFORMANCE OF THE MODEL

5.3.1 Tests with symmetric loading

After the calibration of the monotonic parameters, the cyclic parameters could now be calibrated using cyclic tests from Wichtmann and Triantafyllidis (2016). The performance of the new model is shown in figures Figure 5.10-Figure 5.12 and it is apparent that stress path can be captured very satisfactory.

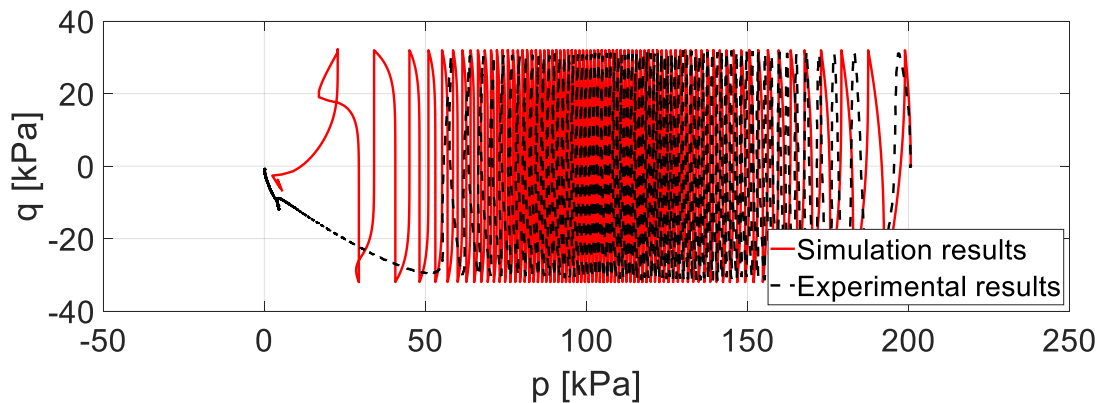


Figure 5.10: Stress path of loose sand (TCUI1). Red line refers to the new model and black line to the experimental results.

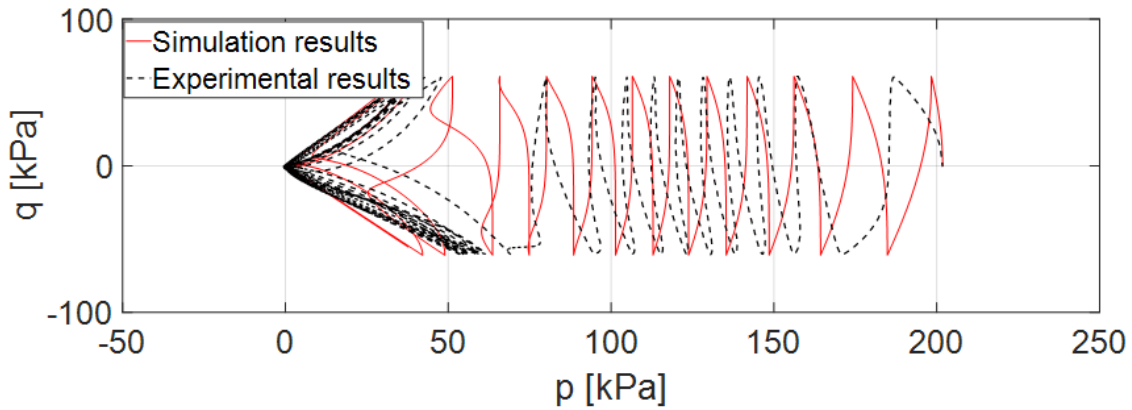


Figure 5.11: Stress path of medium dense sand (TCUI7). Red line refers to the new model and black line to the experimental results.

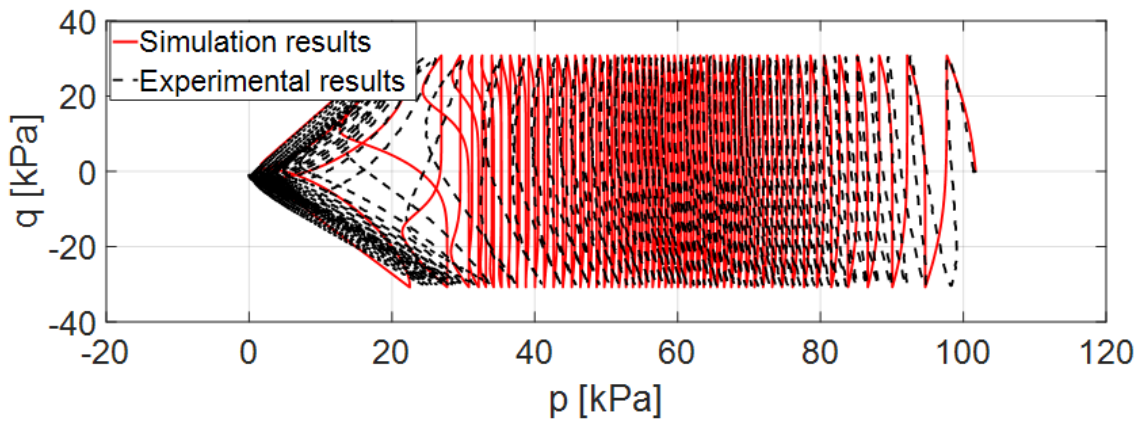


Figure 5.12: Stress path of dense sand (TCUI17). Red line refers to the new model and black line to the experimental results.

It can be seen that unlike Sanisand, the new model is able to capture the fact that there is no “butterfly” shape towards the end of the test for loose sands. Another important remark is that TCUI1 originally reaches zero effective mean stress because the experiment was stopped, after the failure criterion was fulfilled ($|\epsilon_1|=10\%$). This was achieved after the effective stress path crossing the failure line apparently.

The performance of the model is not as good in terms of strain development, especially for denser samples and after the initial liquefaction as it can be seen in Figures Figure 5.13 and Figure 5.14.

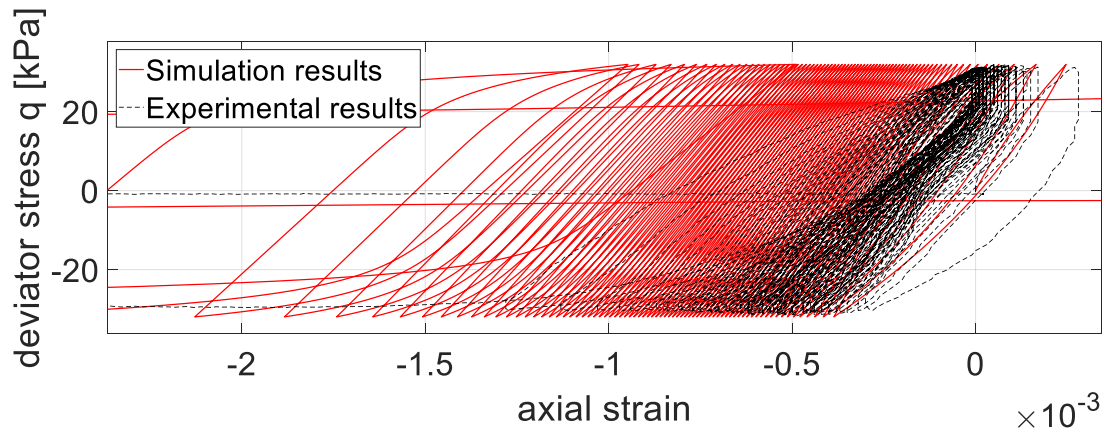


Figure 5.13: Stress-strain response of loose sand (TCUI1). Red line refers to the new model and black line to the experimental results.

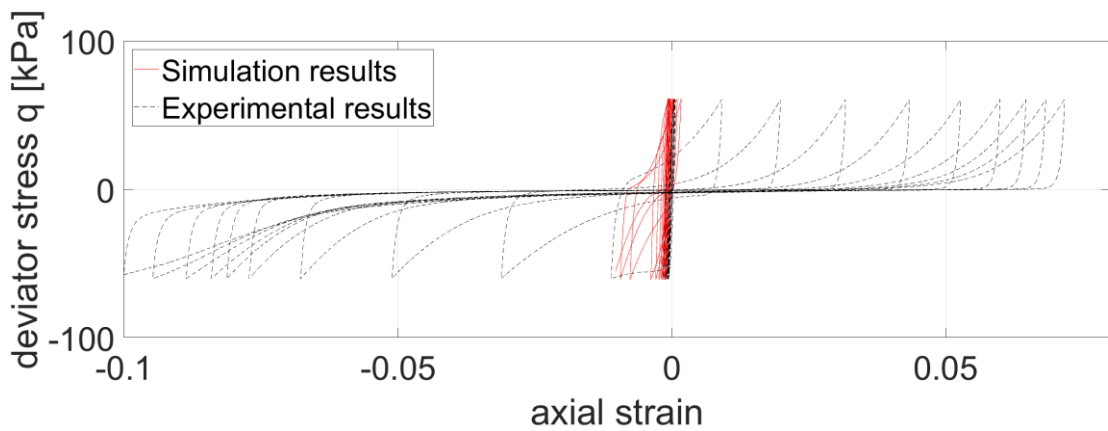


Figure 5.14: Stress-strain response of medium dense sand (TCUI7). Red line refers to the new model and black line to the experimental results.

The previous results were produced with a different set of parameters for each test, except for loose samples which were simulated with a single set of parameters. More specifically, μ_0 was the parameter that needed modification. In Table 7 the best-fit values of μ_0 are given.

Table 7: Optimum values of μ_0 for each test.

	Test	e_0 [-]	I_{D0} [-]	p_0' [kPa]	q^{amp1} / p_0' [kPa]	N_{ini} [-]	μ_0
Loose	TCUI1	0.952	0.27	200	0.15	72	82.5
	TCUI5	0.956	0.26	200	0.15	86	82.5
	TCUI6	0.964	0.24	300	0.15	144	82.5
Medium dense	TCUI7	0.800	0.67	200	0.30	11	35
	TCUI8	0.821	0.62	100	0.20	249	156.8
	TCUI9	0.798	0.68	100	0.25	100	128
	TCUI11	0.842	0.56	200	0.20	146	119.8
	TCUI12	0.813	0.64	200	0.25	77	92
	TCUI14	0.846	0.55	300	0.20	257	113.5
	TCUI15	0.808	0.65	300	0.25	110	79.5

Dense	TCUI17	0.726	0.87	200	0.30	185	92.5
	TCUI18	0.759	0.78	100	0.30	54	89
	TCUI21	0.754	0.80	200	0.30	61	67
	TCUI22	0.744	0.82	300	0.30	269	87.2

In the previous table it can be seen that for medium dense sand μ_0 is lower for higher ratio q^{amp}/p_0 , which is the amplitude of loading. For dense sand in three cases, which have the same q^{amp}/p_0 , μ_0 is approximately the same. This is also the case for loose sand. It seems that there is not a dependence of μ_0 on the relative density, since it does not increase (or decrease) for denser sand.

However, it is more convenient to have only one set, at least for a given density state of sand (loose, medium dense and dense). The proposed parameter sets are given in Table 8 and the values of μ_0 are the average values of the best-fit values. In the appendix the optimal values of μ_0 for each case will be given.

Table 8: Cyclic parameters for different density states of sand

Parameter	Loose	Medium dense	Dense
μ_0	82.5	115	82.2
ζ	0.0005	0.0005	0.0005
β	6.0	6.0	6.0

In Figures Figure 5.15-Figure 5.17 the accumulated pore pressure is shown for the optimal and average values of μ_0 , except those of loose samples for which the average and optimal μ_0 are identical.

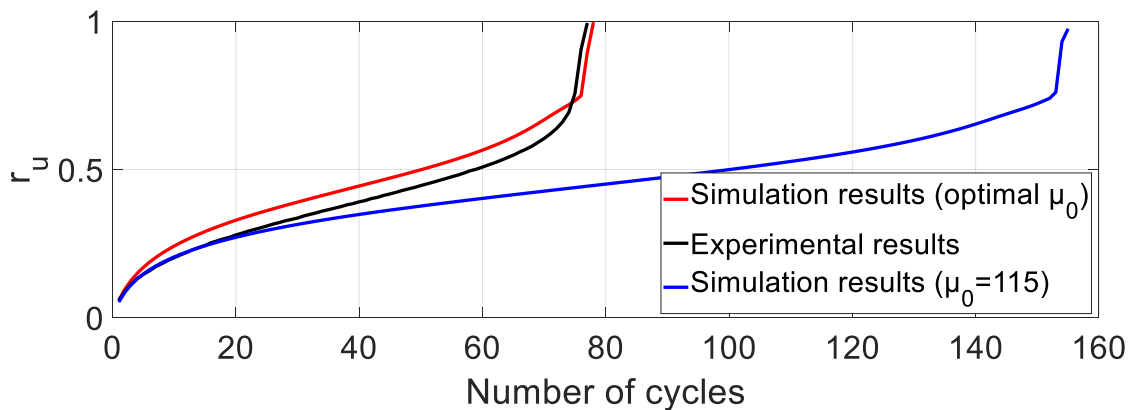


Figure 5.15: Pore water pressure accumulation for TCUI12. Optimal value of $\mu_0 = 92$.

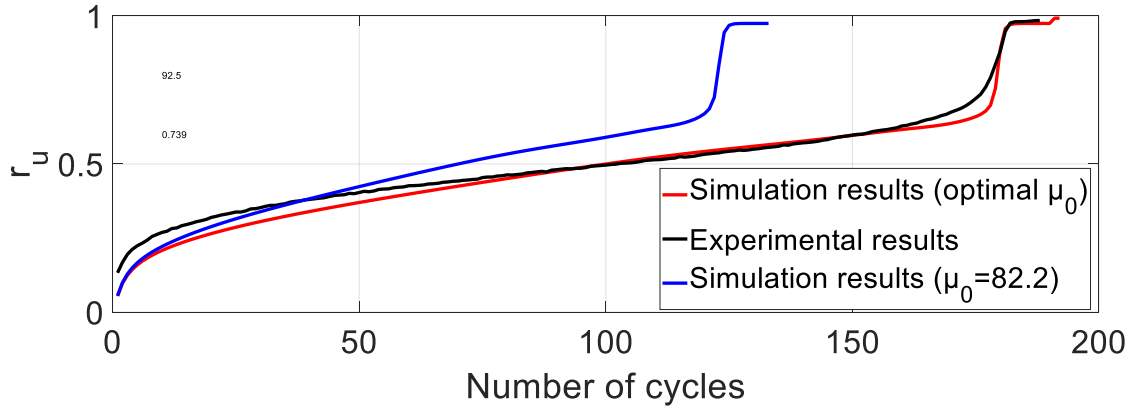


Figure 5.16: Pore water pressure accumulation for TCUI17. Optimal value of $\mu_0 = 92.5$.

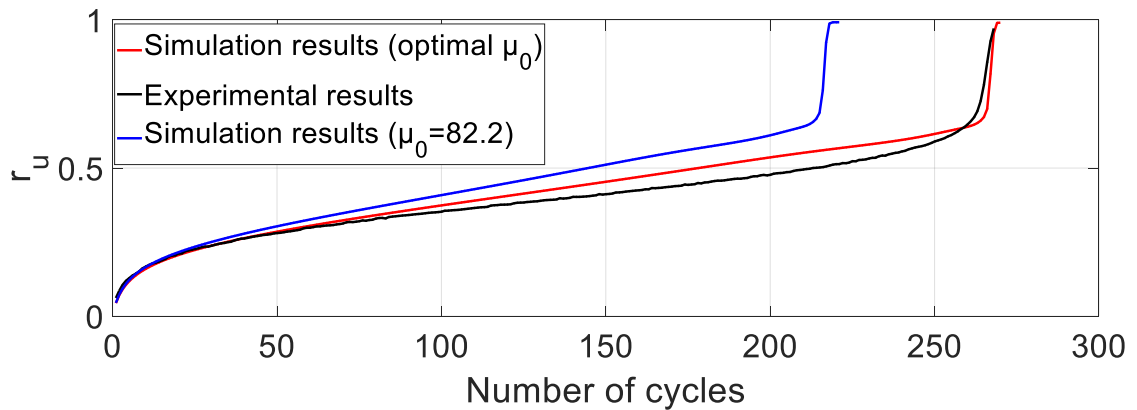


Figure 5.17: Pore water pressure accumulation for TCUI22. Optimal value of $\mu_0 = 87.2$.

It can be observed that when μ_0 is higher than the optimum value, the number of cycles to liquefaction is increased.

5.3.2 Tests with asymmetric loading

The previous tests refer to tests of isotropic consolidation or, else, symmetric loading. However, in most cases the consolidation of soil is anisotropic and the loading is not around zero average shear stress. In this case a different set of parameters is required in order to simulate sand behaviour. More specifically, ζ and β are very different from the case of symmetric loading as it can be seen in Table 10. As before, first the best fit values will be given for each test in Table 9.

Table 9: Optimum values of μ_0 and β for tests of asymmetric loading.

Test	e_0 [-]	I_{D0} [-]	$p_{0'}$ [kPa]	$q^{ampl} / p_{0'}$ [kPa]	η_0 [-]	μ_0	β
TCUA2	0.812	0.64	300	0.4	0.5	113.6	28.4
TCUA3	0.727	0.87	300	0.4	0.5	350	19
TCUA4	0.816	0.63	300	0.2	0.5	100	26.5

TCUA5	0.818	0.63	300	0.3	0.5	100	23.5
TCUA9	0.840	0.57	100	0.25	0.75	113.6	28.4
TCUA10	0.805	0.66	200	0.25	0.75	150	30
TCUA11	0.817	0.63	300	0.25	0.75	68	27
TCUA14	0.838	0.57	200	0.3	0.5	150	25
TCUA19	0.804	0.66	200	0.2	-0.5	150	32

For this type of tests, there is no clear dependence of the parameters on a property of sand or loading conditions. There seems to be an increase of μ_0 for higher relative densities, but there are not enough tests to confirm this. However in this case the parameters are not very different for each test. Furthermore, in the tests that are shown in next figures, as well as in the Appendix, the average parameters do not affect the response of the model. This happens due to the different nature of these tests, which are not characterized by the number of cycles to liquefaction, but from the final level of permanent pore pressure, which is constant after a few cycles. The average set of parameters is given in Table 10. The results refer only to medium dense sand, because the majority of samples in the data base are of this density.

Table 10: Parameters for tests of anisotropic consolidation (medium dense sand).

Parameter	Value
μ_0	113.6
ζ	1.0
β	28.4

The performance of the model for asymmetric loading is shown in Figure 5.18. The stress path in this case is produced with the average parameters and it can be seen that the results are very accurate. This is illustrated in Figure 5.19 where the final level of accumulated pore water pressure is not influenced as much as in the case of isotropic tests. The only difference between average and optimal values is that the final level of pore pressure is reached after a higher number of loading cycles.

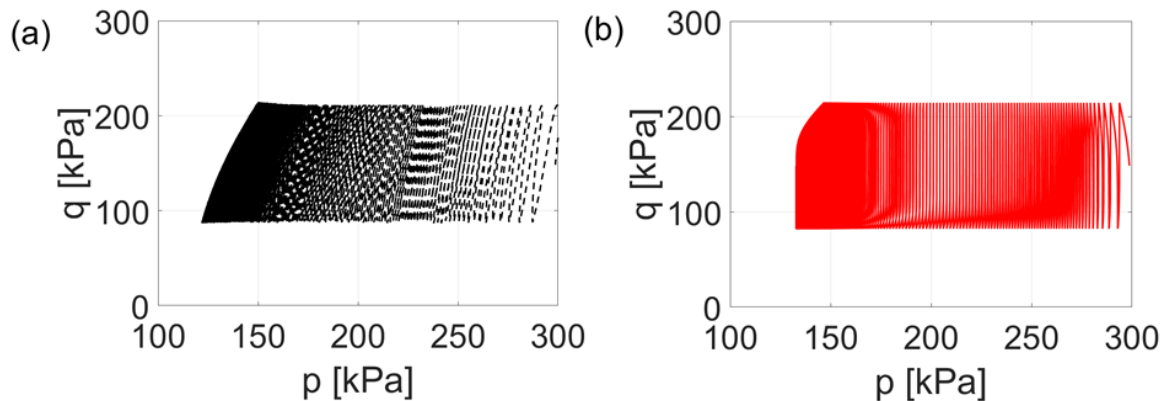


Figure 5.18: Stress path for TCUA4 (a) Experimental results, (b) New model.

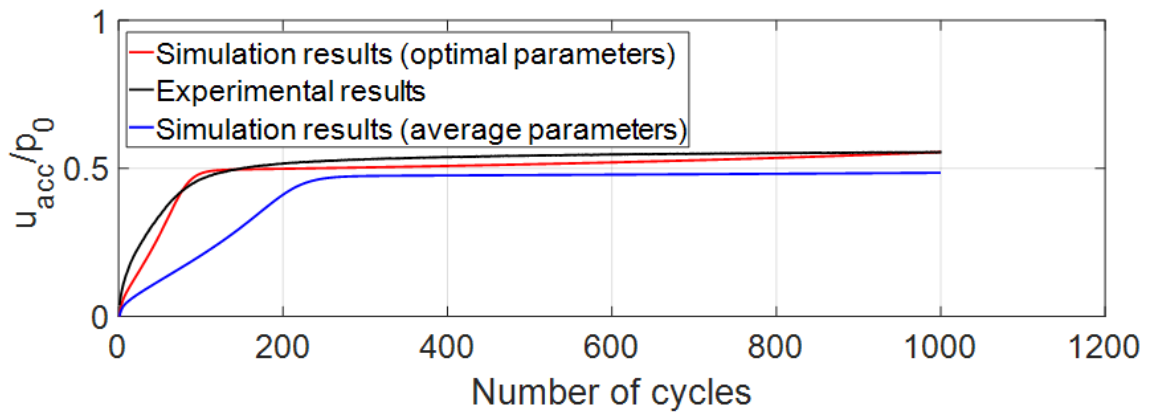


Figure 5.19: Pore water pressure accumulation for TCUA4. Optimal values: $\mu_0=100$, $\beta=26.5$.

Despite the fact that the new model is quite accurate regarding the pore pressure accumulation, the strain development is not satisfactory, which is common for the majority of the existing models. This is illustrated in Figure 5.20. A probable reason for this fault is the flow rule. It could be possible that a slightly different formulation of the dilatancy coefficient could solve this problem.

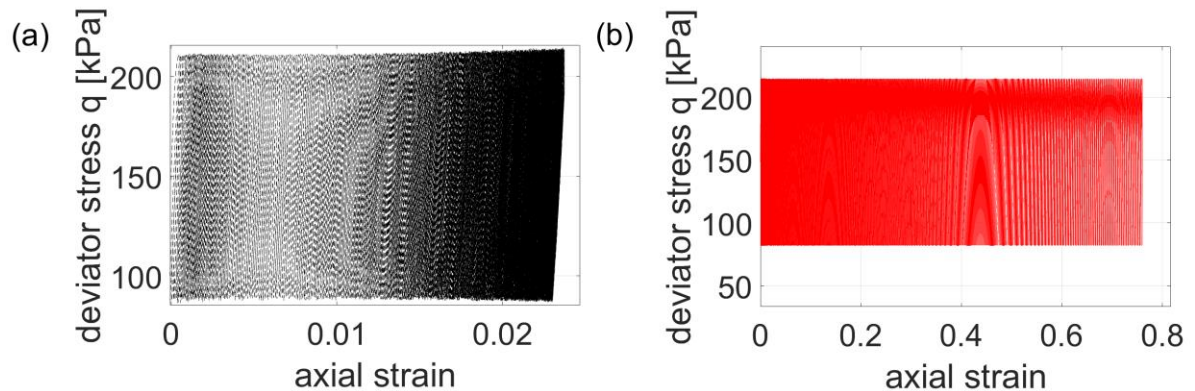


Figure 5.20: Stress-strain response for TCUA4 (a) Experimental results, (b) New model.

In Figure 5.21 the performance of the test for TCUA2 is shown and it can be seen that there are not optimal parameters for this test, since the average parameters were very close to the optimal values. Another interesting result is shown in Figure 5.22, which refers to dense sand. In this case the same set of parameters is used as before, so it would be reasonable to use only one set of parameters at least for cases with asymmetric loading.

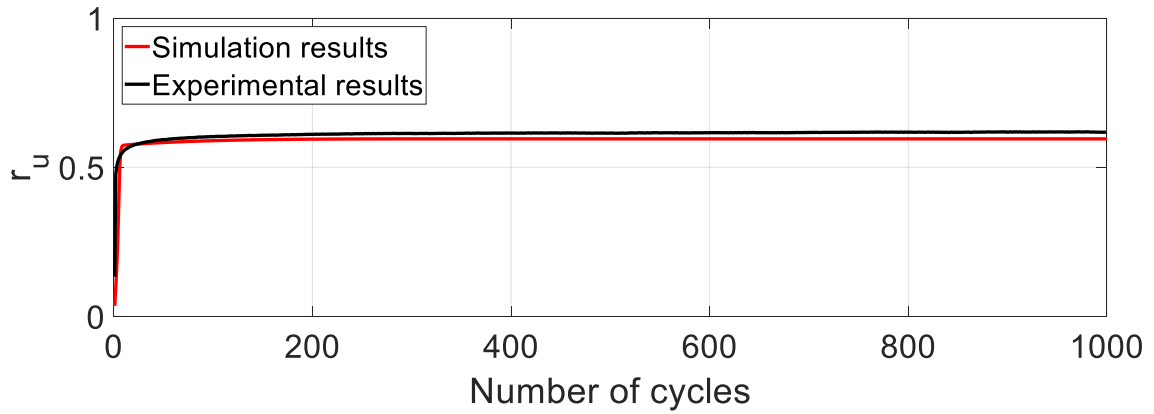


Figure 5.21: Pore water pressure accumulation for TCUA2.

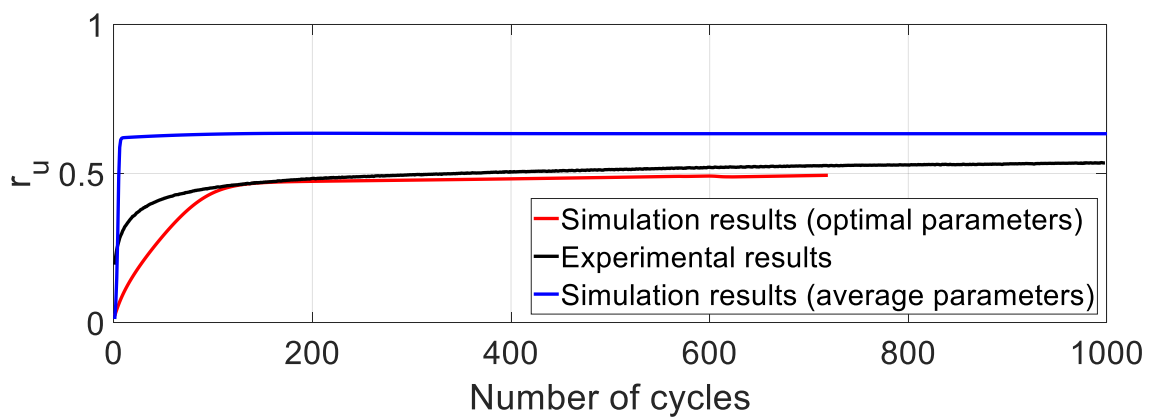


Figure 5.22: Pore water pressure accumulation for TCUA3. Optimal values: $\mu_0=350$, $\beta=19$.

In section 5.2 it was shown that the behaviour of the model for extension monotonic tests is not the optimum. Surprisingly, this is not the case for the cyclic loading, which is simulated accurately as it can be seen in Figures Figure 5.23 and Figure 5.24.

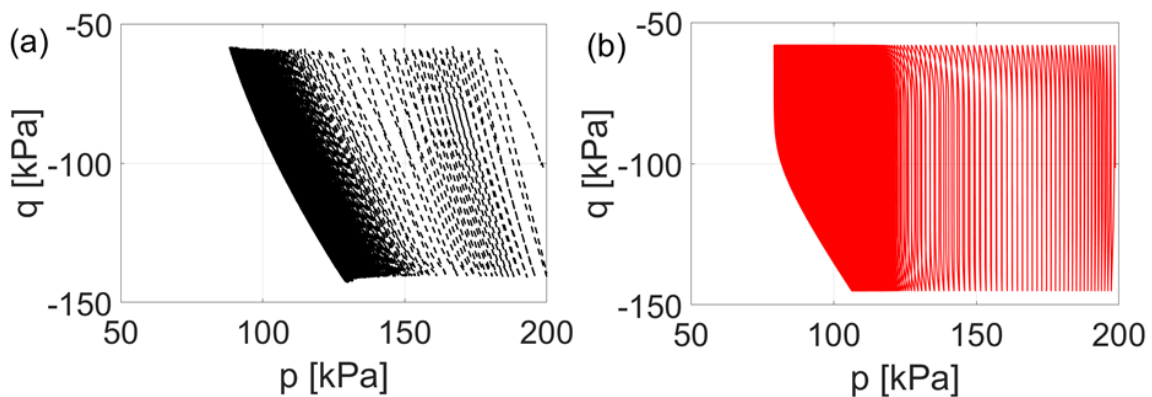


Figure 5.23: Stress path for TCUA19 (a) Experimental results, (b) New model.

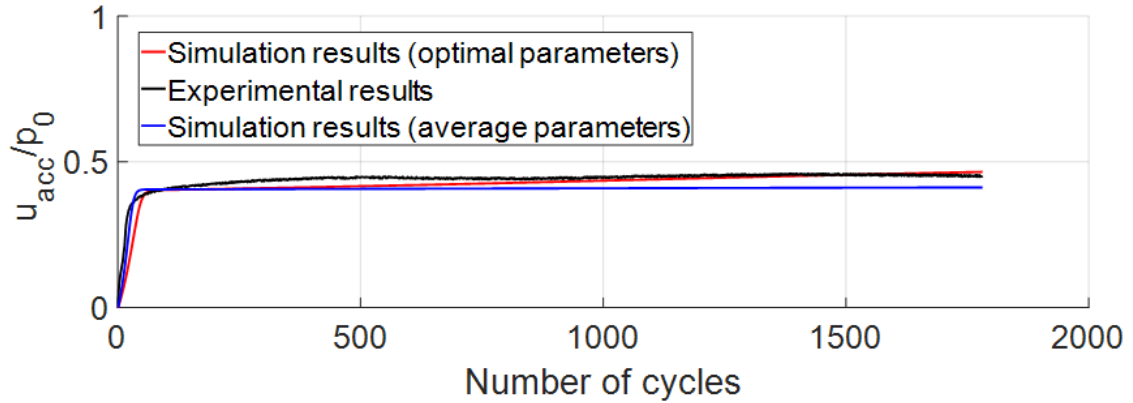


Figure 5.24: Pore water pressure accumulation for TCUA19. Optimal values: $\mu_0=150$, $\beta=32$.

5.3.3 Influence of cyclic parameters

The influence of memory surface parameters on the accumulation of pore pressure is useful, in order to understand the model and provide advices for future researchers, who want to calibrate the model for other types of sand. The tests selected to test their response are TCUI12 and TCUA4, which both refer to medium dense sand. It can be observed from Figures 5.25, 5.27,-5.29 that μ_0 and β have the biggest influence on either the number of cycles to liquefaction or the final level of pore pressure. On the other hand ζ does not affect the final results significantly (Figure 5.26). The tests for different ζ for TCUA4 are not included, since pore pressure is identical for all cases. In this case ζ ranged from 1.0 to 50.0.

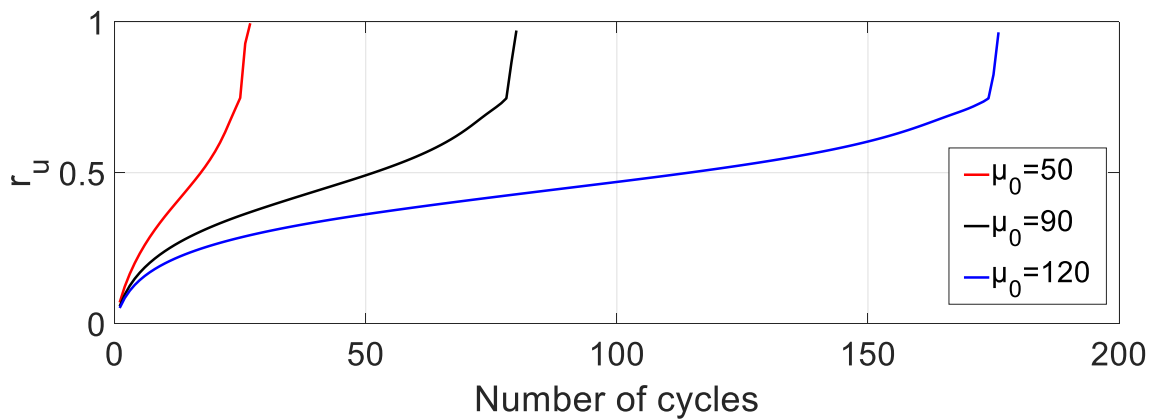


Figure 5.25: Influence of μ_0 on TCUI12.

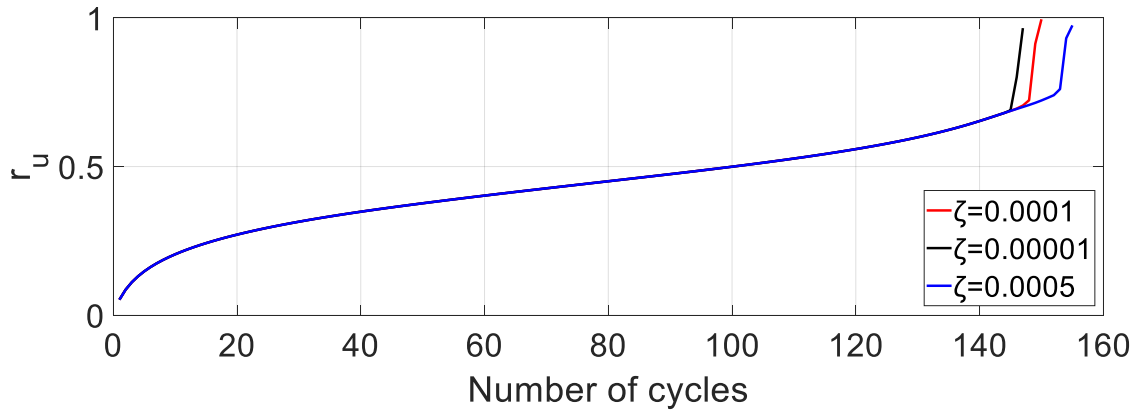


Figure 5.26: Influence of ζ on TCUI12.

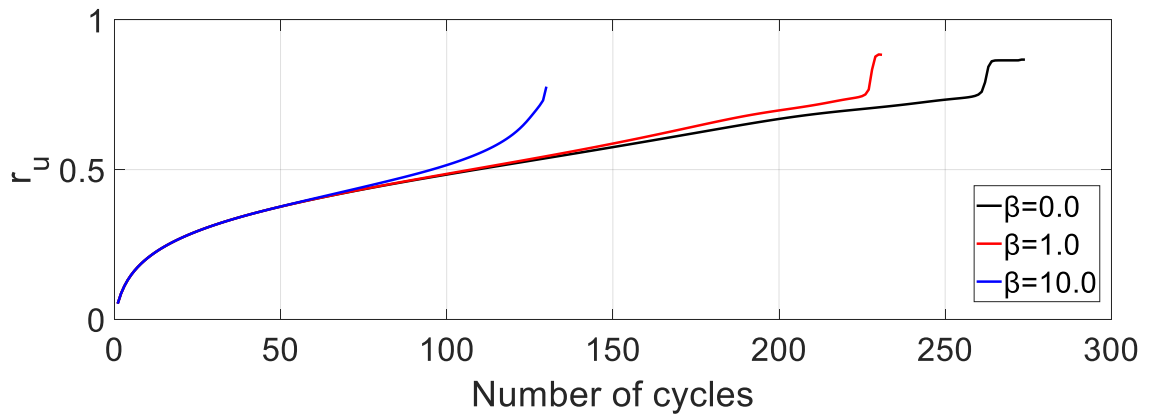


Figure 5.27: Influence of β on TCUI12.

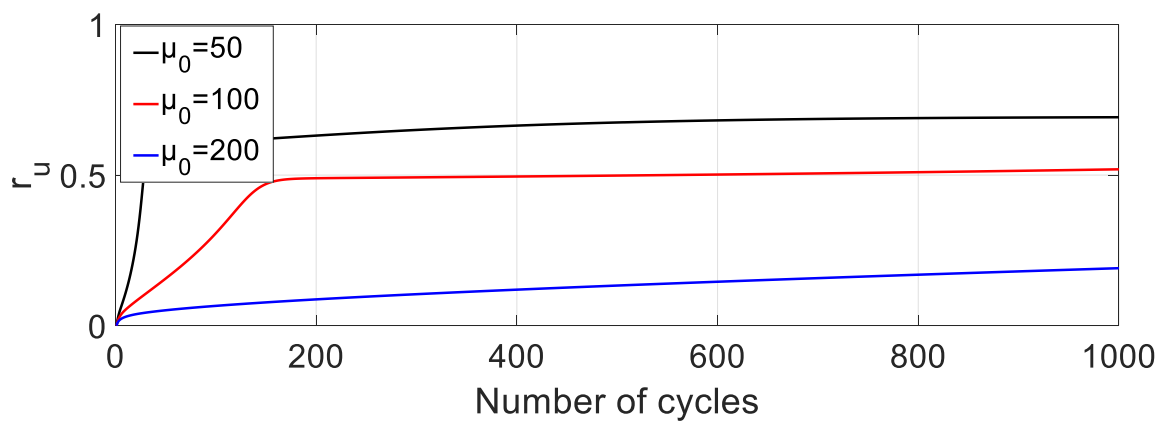


Figure 5.28: Influence of μ_0 on TCUA4.

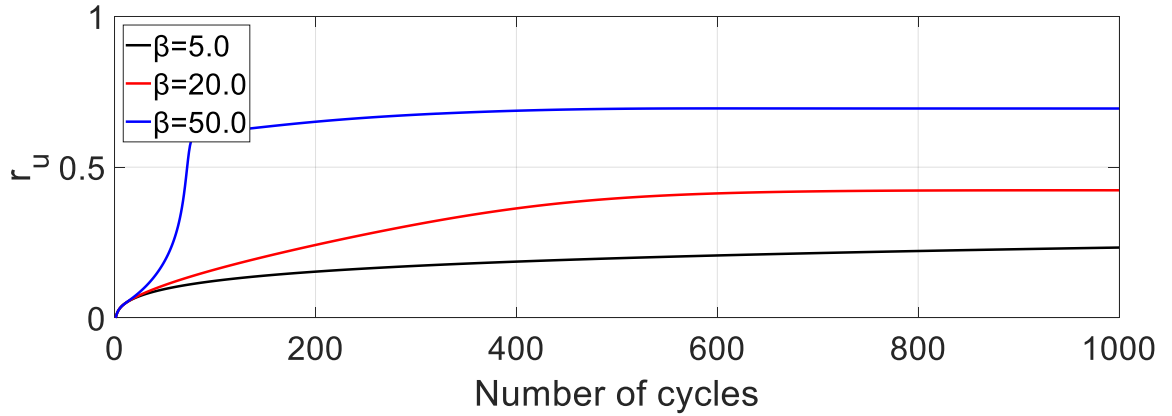


Figure 5.29: Influence of β on TCUA4.

5.3 CYCLIC CONTOUR DIAGRAMS

After the calibration of monotonic and cyclic parameters and the validation of the model for various loading conditions, cyclic contour diagrams can now be constructed. The fact that the new model is not accurate regarding the prediction of strain development, led to the choice of pore pressure contour diagrams. These diagrams will be presented in this section, as well as some corresponding diagrams of NGI, since they should not differ remarkably. In Figures 5.30 and 5.31 two pore pressure contour diagrams are given for different average shear stress.

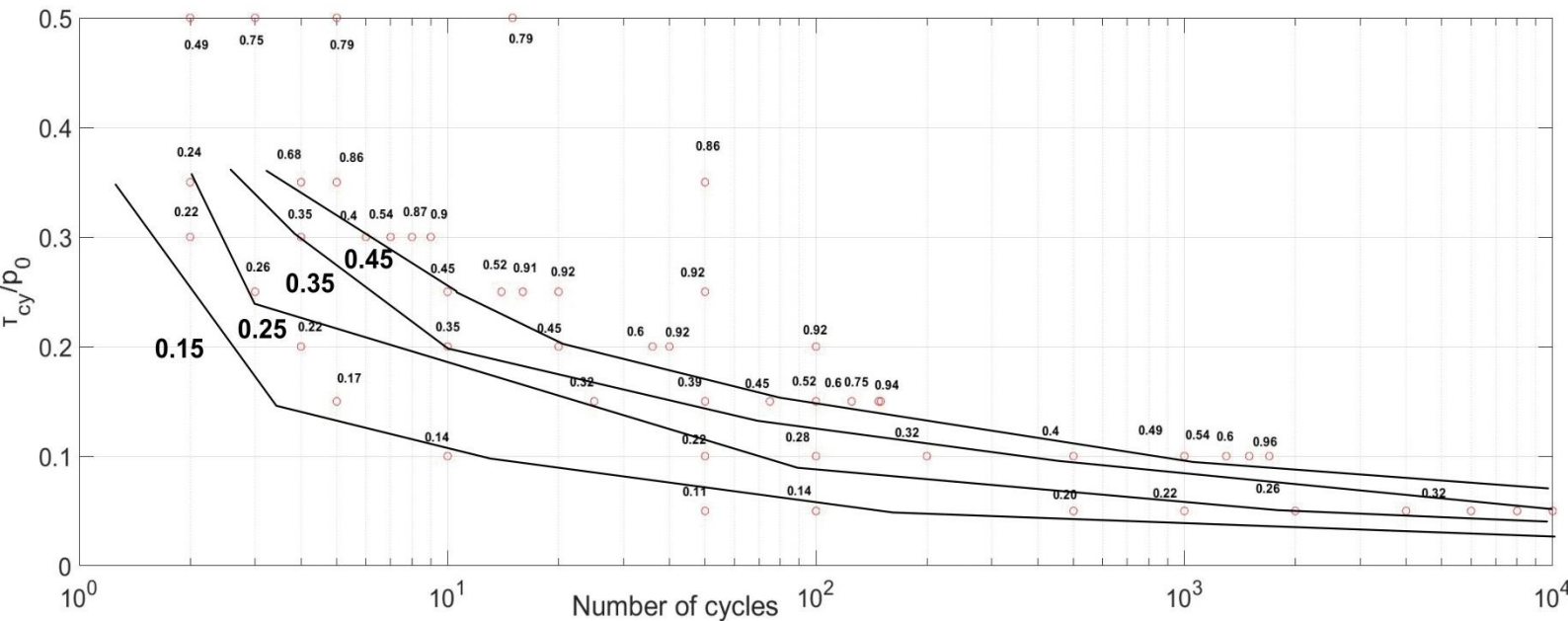


Figure 5.30: Pore pressure contour diagram for medium dense sand. Results from triaxial results, $\tau_{av}/p_0=0$, $p_0=200$ kPa, without drained precycle.

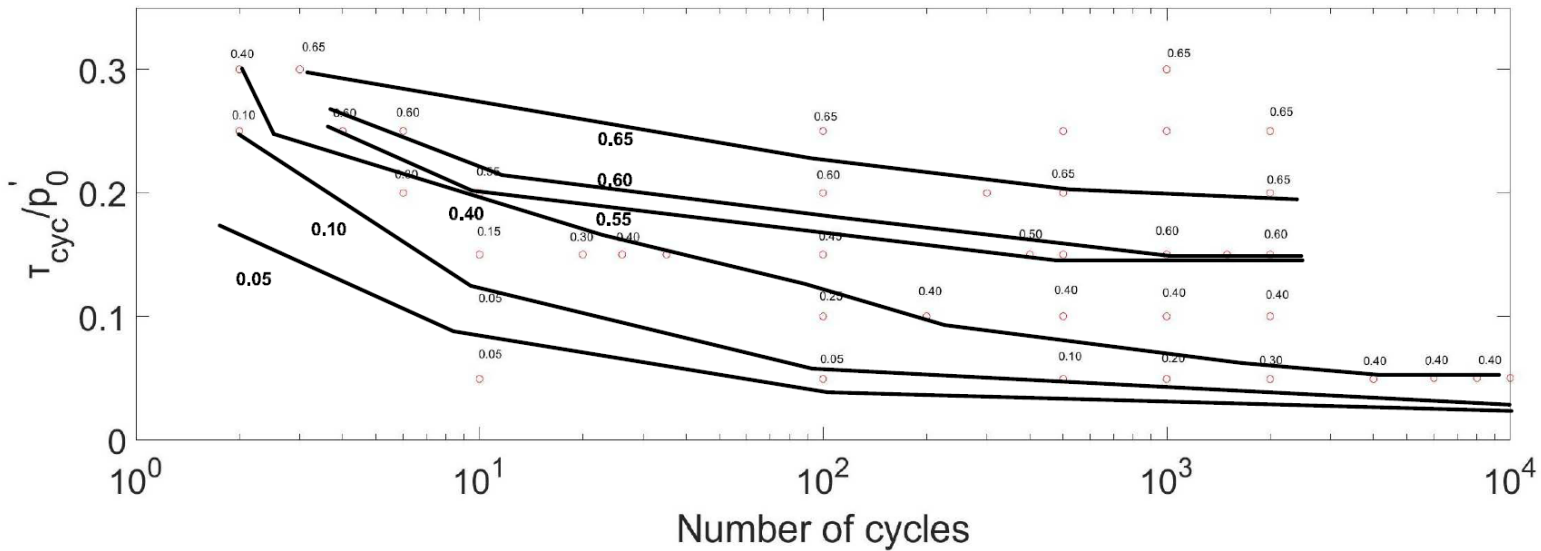


Figure 5.31: Pore pressure contour diagram for medium dense sand. Results from triaxial results, $\tau_{av}/p_0'=0.3$, $p_0'=200$ kPa, without drained precycle.

The previous diagrams can be directly compared to the NGI diagrams. One example of such a diagram, for similar conditions Figures 5.30-5.31, is given in Figure 5.32.

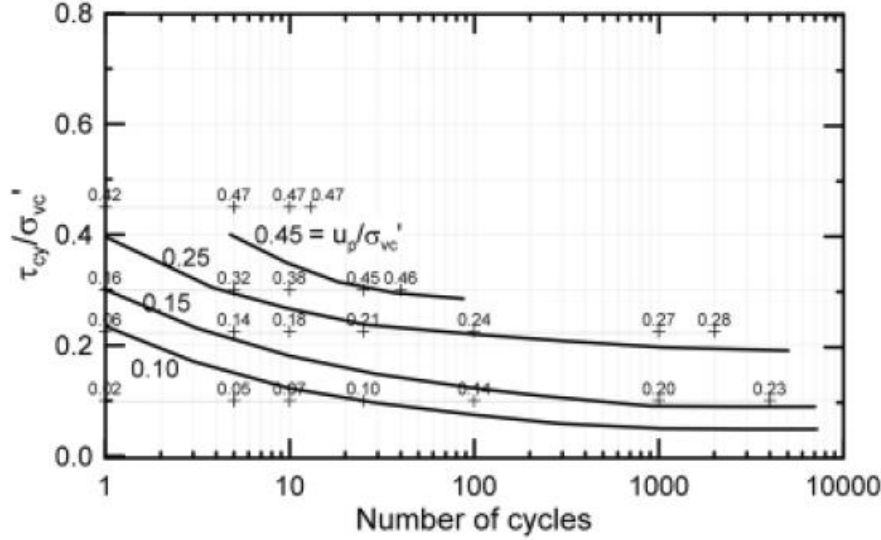


Figure 5.32: Pore pressure contours for medium dense sand. Results from triaxial results, $\tau_{av}/p_0'=0.25$, $p_0'=250$ kPa (from Andersen, 2015).

Other two contour diagrams were produced for given number of cycles (10 and 100). In Figure 5.33 it can be seen that for a higher number of cycles, permanent pore pressure reaches a higher value.

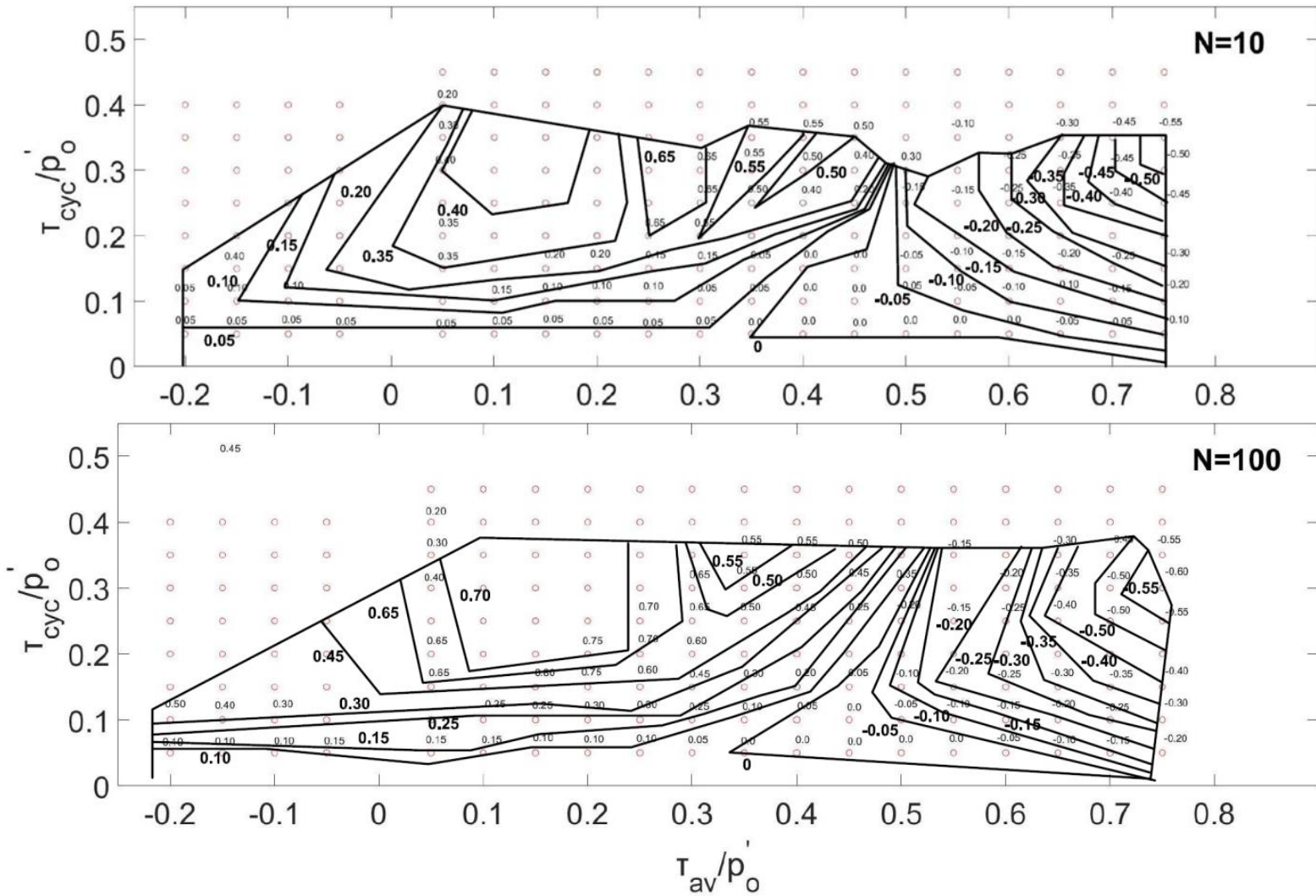


Figure 5.33: Pore pressure contours as a function of average and cyclic shear stresses for triaxial tests on medium dense sand. The upper figure refers to 10 loading cycles and the lower to 100 cycles.

There are also some corresponding diagrams in Andersen (2015). One example is given in Figure 5.34. It can be observed that the contour lines produced by the new model are not as smooth as in the NGI diagrams. A possible explanation is that in NGI diagrams the lines were developed after interpolations, while the new diagrams used over 60 tests to draw the contour lines. Of course, it is possible to smoothen the contour lines with more data points.

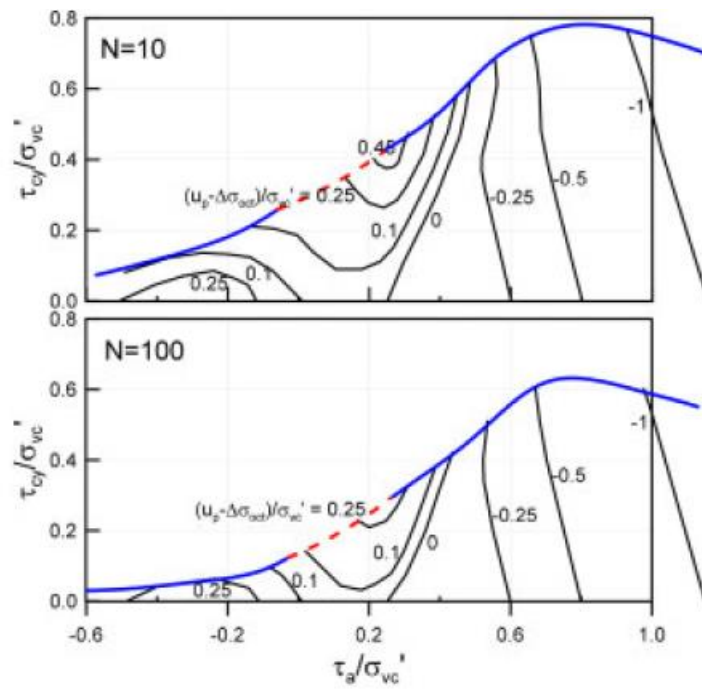


Figure 5.34: Permanent pore pressure for given number of cycles. Triaxial tests on medium dense sand (from Andersen, 2015).

6. CONCLUSIONS-RECOMMENDATIONS

In the previous pages the validation of a new constitutive model was presented. In this chapter, the advantages of the model will be discussed, as well as the limitations, which will lead to some recommendations for future research.

6.1 CONCLUDING REMARKS

The model presented in this thesis is a constitutive model that combines bounding surface plasticity theory and an additional surface, which tracks the stress history of soil; the memory surface. The thesis was focused on the validation of the model under undrained conditions that are often encountered in offshore practice. Undrained conditions were also indispensable in order to construct cyclic contour diagrams, which are often used in practice.

The first step towards the validation of the new model was firstly to find available data for a specific type of sand for high cyclic loading and it was extremely useful that Wichtmann and Triantafyllidis (2016) have made available such a data base for sand. Besides that, they have included monotonic tests that made much easier and more valid the calibration of the model parameters. The conclusions that can be extracted after a careful observation of the results are the following:

- The monotonic behaviour of Sanisand and the new model is identical. This is one of the main reasons that it was selected to follow the formulation from Dafalias and Manzari (2004), since this model is well established for monotonic conditions, for a variety of sand types.
- The prediction for monotonic compression tests is satisfactory. In nearly all cases the stress path is captured very well and the stress-strain response, too. Only for loose samples and drained conditions it can be said that volumetric strain is a little over-predicted.
- The extension monotonic tests were not simulated as good as the compression ones, probably due to the shape of bounding surface.
- The number of cycles to liquefaction for isotropic tests can be controlled with using different values of μ_0 . It has been noticed that this parameter is probably affected by void ratio, confinement pressure and stress amplitude.
- After the initial liquefaction, the model cannot capture the development of strains, which take positive values.
- The stress path of anisotropic tests is well simulated from the model, in almost all cases. There are not enough tests though for loose samples.
- In reality, strain development during anisotropic tests stops after some loading cycles. However, this is not captured from the model.
- The cyclic extension tests are well simulated by the model.

- The cyclic contour diagrams produced by this model can be compared to already established diagrams from NGI, at least qualitatively.

6.2 FUTURE RESEARCH

Despite the limitations discussed above the results are encouraging. The model can be used in order to predict the behaviour of a sand under a variety of loading conditions and relative densities. This can be done with calibrating the parameters with a limited number of lab tests. Also, foundation designers of offshore structures can use this model to construct contour diagrams without extensive laboratory or site-specific testing. As a result, the cost of such a structure can be reduced significantly without negotiating its integrity.

Some recommendations for future development of the model can be summarized as following:

- A slight modification of the bounding surface may allow better prediction of the extension tests.
- A possible modification of the flow rule in order to capture more accurately the stress-strain response.
- Modification of equation 4.18 to incorporate the influence of stress amplitude on μ_0 .
- The model was calibrated using stress-controlled tests. The tests for the contour diagrams were also done using stress-controlled tests. However, it can be useful to test the model for strain controlled tests, as well.
- Calibration of the model for other types of sand (e.g. Toyoura sand) or with higher fines content.
- It is useful to create cyclic contour diagrams for DSS tests, as well.

BIBLIOGRAPHY

Airey, D. W. & Fahey, M. (1991). Cyclic response of calcareous soil from the North-West Shelf of Australia. *Geotechnique*, 41(1), pp. 101-121.

Andersen, K.H, Kleven, A. & Heien, D. (1998). Cyclic soil data for design of gravity structures. *Journal of the Geotechnical Engineerin, ASCE*, 114(5), pp. 517-539.

Andersen, K.H, & Lauritzen, R. (1998). Bearing capacity of foundation design. *Journal of the Geotechnical Engineerin, ASCE*, 114(5), pp. 540-555.

Andersen, K. H. (2009). Bearing capacity under cyclic loading - offshore, along the coast, and or land. *Canadian Geotechnical Journal*, 46(5), pp. 513-535.

Andersen, K. H. (2015). Cyclic soil parameters for offshore foundation design. *3rd McClelland Lecture: Frontiers in Offshore Geotechnics III*, V. Meyer, ed., Taylor & Francis Group, Oslo, Norway, pp. 5-82.

Andrus, R. D., & Stokoe, K. H., II. (1997). Liquefaction resistance based on shear wave velocity." *Proc., NCEER workshop on evaluation of liquefaction resistance of soils*. Nat. Ctr. for Earthquake Engrg. Res., State Univ. of New York at Buffalo, pp. 89-128.

Andrus, R.D., and Stokoe, K.H.,II. (2000). Liquefaction resistance of soils from shear-wave velocity. *J. Geotech. and Geoenviron. Engrg., ASCE*, 126(11), pp. 1015-1025.

Bardet, J.P. (1986). Bounding surface plasticity model for sands. *Journal of Engineering Mechanics*, 112(11), pp. 1198-1216.

Been, K. & Jefferies, M. G. (1985). A state parameter for sands. *Géotechnique*, 35(1), pp. 99-112.

Booker, J.R., Rahman, M.S. & Seed, H.B., (1976). GADFLEA-A computer program for the analysis of pore pressure generation and dissipation during cyclic and earthquake loading. *Rep. No. EERC 76-24*, Earthquake Engineering Research Center, Univ. of California at Berkeley, Berkeley, Calif.

Casagrande, A. (1936). Characteristics of cohesionless soils affecting the stability of slopes and earth fills. *Journal of the Boston Society of Civil Engineers*.

Casagrande, A. (1938). The shearing resistance of the soils and its relation to the stability of earth dams. *Proceedings, Soils and Foundation Conference of the U.S. Engineer Department*.

Castro, G. & Poulos, S.J. (1977). Factors affecting liquefaction and cyclic mobility. *Journal of Geotechnical and Geoenvironmental Engineering*, 103(6), pp. 501-516.

Chiaradonna, A., Tropeano, G., d'Onofrio, A. & Silvestri, F. (2015). Application of a simplified model for the prediction of pore pressure build-up in sandy soils subjected to seismic loading. *Proc. 6th Int. Conf. Earthquake Geotechnical Engineering*, Christchurch, New Zealand.

Corti, R. (2016). *Hardening memory surface constitutive model for granular soils under cyclic loading conditions*. PhD Thesis, University of Bristol, Bristol (U.K.).

Dafalias, Y. F. & Popov, E. P. (1975). A model of nonlinearly hardening materials for complex loading. *Acta Mechanica*, 21(3), pp. 173-192.

Dafalias, Y. F. (1986). Bounding surface plasticity. I: Mathematical foundation and hypoplasticity. *Journal of Engineering Mechanics*, 112(9), pp. 966-987.

Dafalias, Y. F., & Manzari, M. T. (2004). Simple plasticity sand model accounting for fabric change effects. *Journal of Engineering Mechanics*, 130(6), 622-634.

Di Benedetto, H., Blanc, M., Tiouajni, S. & Ezaoui, A. (2014). Elastoplastic model with loading memory surface (LMS) for monotonic and cyclic behaviour of geomaterials. *International Journal for Numerical and Analytical Methods in Geomechanics*, 38(14), pp. 1477-1502.

Finn W.D.L. & Bhatia, S.K. (1982). Prediction of seismic pore water pressures. *10th International conference in soil mechanics and foundations*, Stockholm, pp 201–206.

Gennaro, V. D., Canou, J., Dupla, J. C., & Benahmed, N. (2004). Influence of loading path on the undrained behaviour of a medium loose sand. *Canadian Geotechnical Journal*, 41(1), 166-180.

Georgiannou, V. N., Tsomokos, A. & Stavrou, K. (2008). Monotonic and cyclic behaviour of sand under torsional loading. *Géotechnique*, 58(2), pp. 113-124.

Green, R.A., Mitchell, J.K. & Polito, C.P. (2000). An energy-based pore pressure generation model for cohesionless soils. *Proc., John Booker Memorial Symp.-Developments in Theoretical Geomechanics*, D.W. Smith and J.P. Carter, eds, Balkema, Rotterdam, The Netherlands, pp. 383-390.

Houlsby, G., Ibsen, L.B. & Byrne, B. (2005). Suction caissons for wind turbines. *Frontiers in Offshore Geotechnics: Proceedings of the International Symposium on Frontiers in Offshore Geotechnics (IS-FOG 2005), 19-21 Sept 2005, Perth, WA, Australia*.

Ishihara, K., Tatsuoka, F. & Yasuda, S. (1975). Undrained deformation and liquefaction of sand under cyclic stresses. *Soils and Foundations*, 15(1), pp. 29-44.

Ivšić, T. (2006). A model for presentation of seismic pore water pressures. *Soil Dynamics and Earthquake Engineering*, 26, pp. 191–199.

Jafarzadeh, F., Javaheri, H., Sadek, T. & Muir Wood, D. (2008). Simulation of anisotropic deviatoric response of Hostun sand in true triaxial tests. *Computers and Geotechnics*, 35(5), pp. 703-718.

Kramer, S.L. (1996). Geotechnical earthquake engineering. *Prentice Hall*.

Krieg, R. D. (1975). A Practical Two Surface Plasticity Theory. *Journal of Applied Mechanics*, 42(3), 641.

Liu, H., Abell, J.A., Diambra, A. & Pisano, F. (2018). A three-surface plasticity model capturing cyclic sand ratcheting. *Géotechnique submitted for publication*.

Luong, M. P. (1982). Mechanical aspects and thermal effects of cohesionless soils under cyclic and transient loading. *Proceedings of the Conference on Deformation and Failure of Granular Materials*, Delft, pp. 239-246.

Maleki, M., Cambou, B. & Dubujet, P. (2009). Development in modelling cyclic loading of sands based on kinematic hardening. *International Journal for Numerical and Analytical Methods in Geomechanics*, 33(14), pp. 1641-1658.

Manzari, M. T., & Dafalias, Y. F. (1997). A critical state two-surface plasticity model for sands. *Géotechnique*, 47(2), pp. 255-272.

Mao, X. & Fahey, M. (2003). Behaviour of calcareous soils in undrained cyclic simple shear. *Géotechnique*, 53(8), pp. 715-727.

Mroz, Z., Norris, V.A. & Zienkiewicz, O.C. (1978). An anisotropic hardening model for soils and its application to cyclic loading. *International Journal for Numerical and Analytical Methods in Geomechanics*, 2, pp. 203-221.

Muir Wood, D. (2004). Geotechnical modelling. *CRC Press*.

Muránsky, O., Hamelin, C.J., Smith, M.C., Bendeich, P.J. & Edwards, L. (2012). The effect of plasticity theory on predicted residual stress fields in numerical weld analyses. *Computational Materials Science*, 54, pp. 125-134.

Park, T., Park, D. & Ahn, J.K. (2014). Pore pressure model based on accumulated stress. *Bull. Earthquake Engineering*, 13, pp. 1913-1926.

Polito, C.P, Green, R.A. & Lee, J. (2008). Pore pressure generation models for sands and silty soils subjected to cyclic loading. *Journal of Geotechnical and Geoenvironmental Engineering*, 134(10), pp. 1490-1500.

Poulos, S. J. (1981). The steady state of deformation. *Journal of the Geotechnical Engineering Division*, ASCE, 107(5), 553-562.

Randolph, M. & Gourvenec, S. (2011). Offshore Geotechnical Engineering. *CRC Press*.

Rauch, A. F. (1997). EPOLLS: An empirical method for predicting surface displacements due to liquefaction-induced lateral spreading in earthquakes. *PhD Thesis, Virginia Polytechnic Institute Blacksburg, Virginia (USA)*.

Robertson, P. K., & Wride, C. E. (1998). "Evaluating cyclic liquefaction potential using the cone penetration test." *Canadian Geotechnical Journal*, 35(3), pp. 442–459.

Roscoe, K. H., Schofield, A. N. & Wroth, C. P. (1958). On the Yielding of Soils. *Géotechnique*, 8(1), pp. 22-53.

Seed, H.B., Martin, P.P. & Lysmer, J. (1975). The generation and dissipation of pore water pressures during soil liquefaction. *Rep. No. EERC 75-26*, Univ. of California, Berkeley, Calif.

Sladen, J. A., D'Hollander, R. D. & Krahn, J. (1985). The liquefaction of sands, a collapse surface approach. *Canadian Geotechnical Journal*, 22(4), pp. 564-578.

Stallebrass, S. E. and Taylor, R. N. (1997). The development and evaluation of a constitutive model for the prediction of ground movements in overconsolidated clay. *Géotechnique*, 47(2), pp. 235-253.

Sturm, H., Andersen, K.H, Langford, T. & Saue, M. (2012). An introduction to the NGI cyclic accumulation approach in the foundation design of OWTs. *12th Baltic Sea Geotechnical Conference, Infrastructure in the Baltic Sea Region Rostock, Germany 31 May - 2 June 2012*.

Taiebat, M., & Dafalias, Y. F. (2008). SANISAND: Simple anisotropic sand plasticity model. *International Journal for Numerical and Analytical Methods in Geomechanics*, 32(8), 915-948.

Towhata, I. (2008). *Geotechnical earthquake engineering*. Springer.

Wichtmann, T., Niemunis, A., Triantafyllidis, T., & Poblete, M. (2005). Correlation of cyclic preloading with the liquefaction resistance. *Soil Dynamics and Earthquake Engineering*, 25(12), pp. 923-932.

Wichtmann, T. and Triantafyllidis, T. (2012). Behaviour of Granular Soils Under Environmentally Induced Cyclic Loads. *Mechanical Behaviour of Soils Under Environmentally Induced Cyclic Loads* (C. Di Prisco and D. Muir Wood ed.) Springer Vienna, pp. 1-136.

Wichtmann, T., & Triantafyllidis, T. (2016). An experimental database for the development, calibration and verification of constitutive models for sand with focus to cyclic loading: part II—tests with strain cycles and combined loading. *Acta Geotechnica*, 11(4), pp. 739-761.

Wood, D. M., Belkheir, K., Liu, D.F. (1994). Strain softening and state parameter for sand modelling. *Géotechnique*, 44(2), pp. 335-339.

Yoshimine, M. & Ishihara, K. (1998). Flow potential of sand during liquefaction. *Soils and Foundations*, 38(3), pp. 189-198.

Youd, T.L. & Idriss, I.M. (2001). Liquefaction resistance of soils: summary report from the 1996 NCEER and 1998 NCEER/NSF workshops on evaluation of liquefaction resistance of soils. *Journal of Geotechnical and Geoenvironmental Engineering*, 127(4), 297-313.

APPENDIX A

RESULTS FOR MONOTONIC AND CYCLIC TESTS

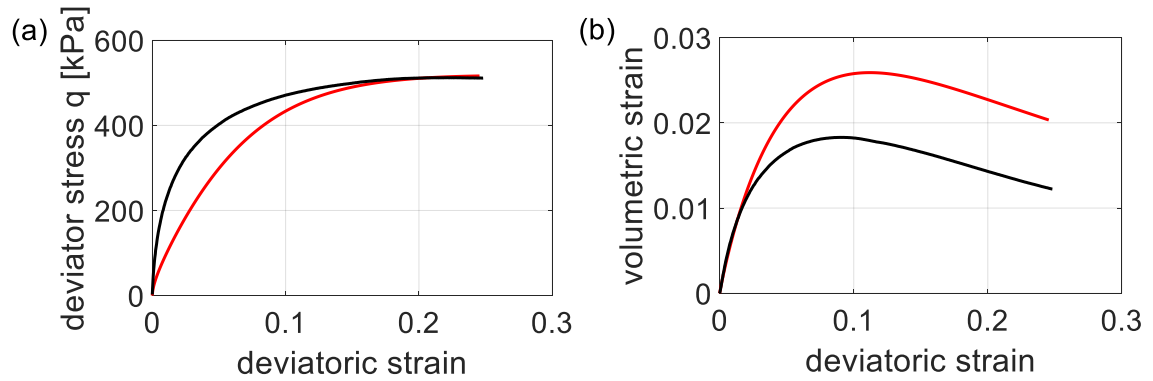


Figure 1: TMD3

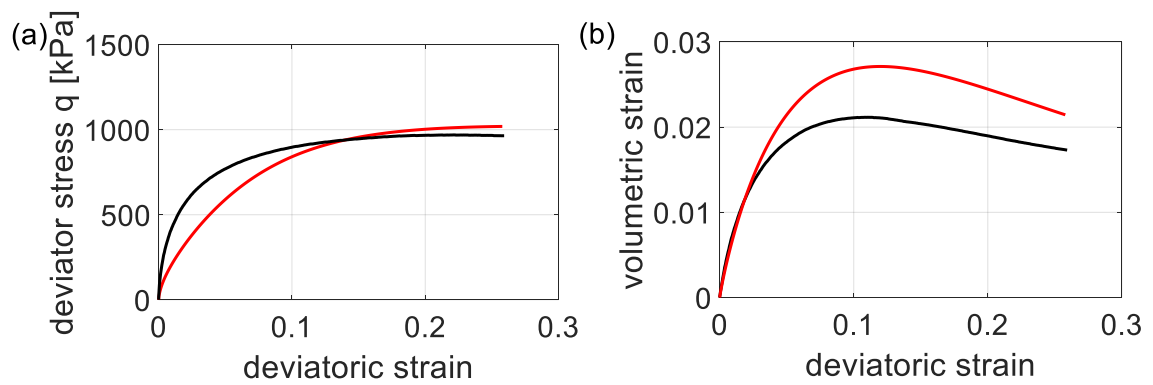


Figure 2: TMD5

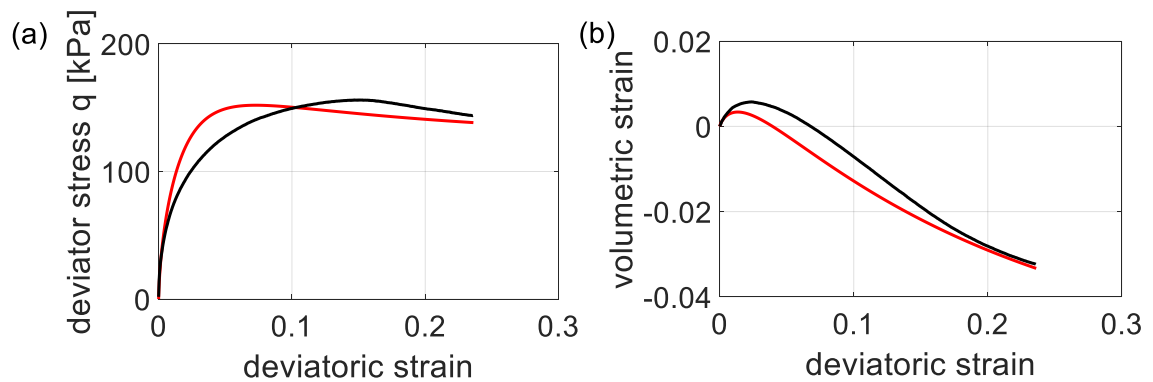


Figure 3: TMD6

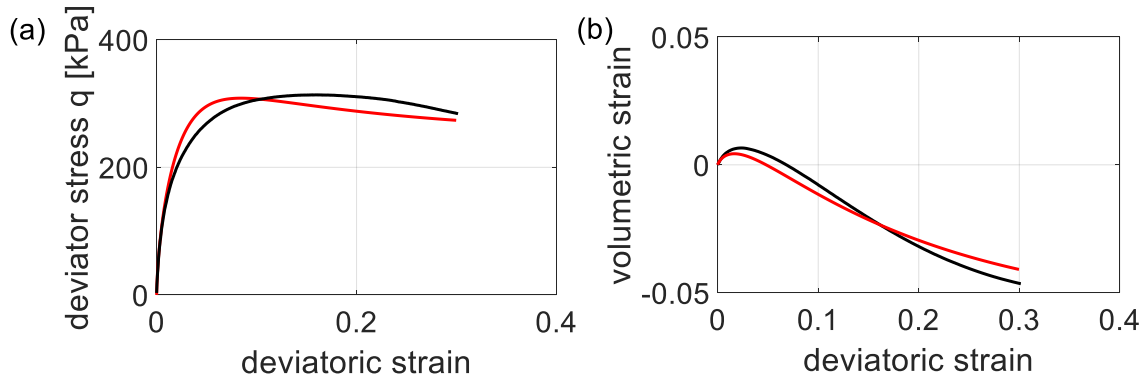


Figure 4: TMD7

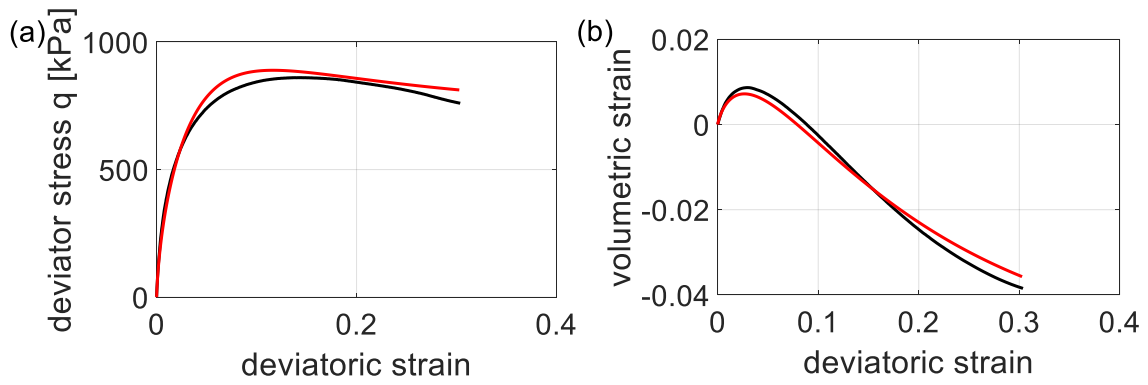


Figure 5: TMD9

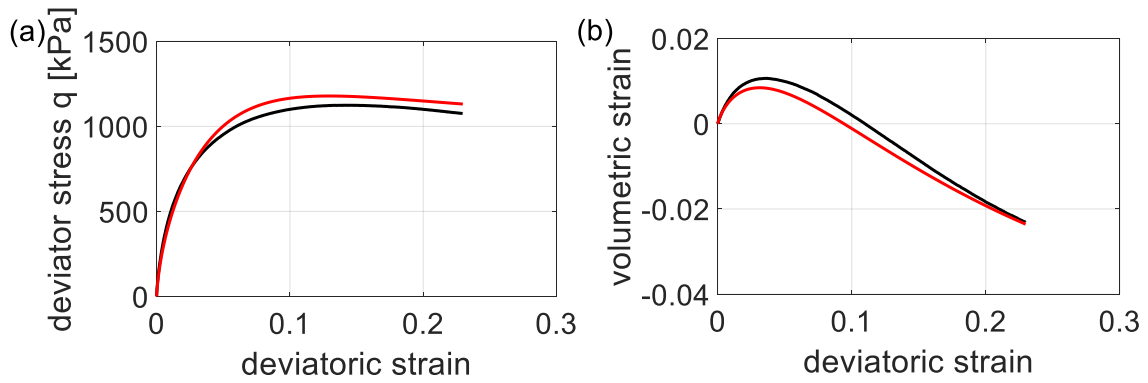


Figure 6: TMD10

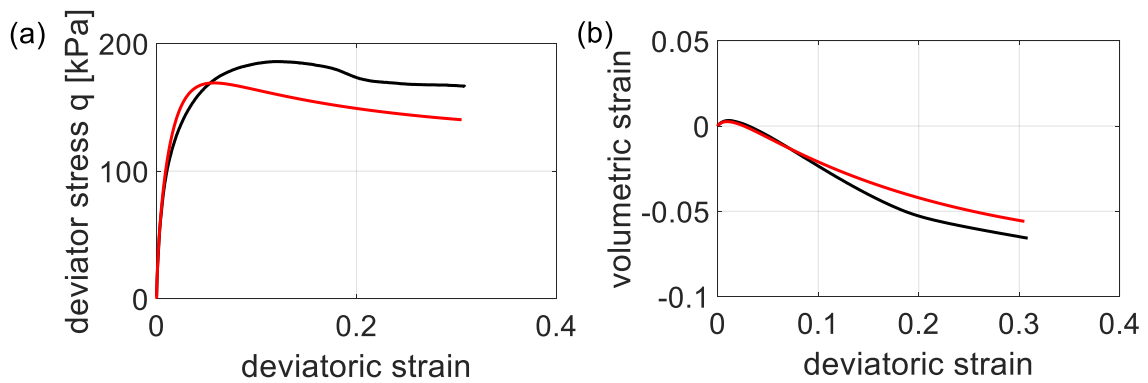


Figure 7: TMD11

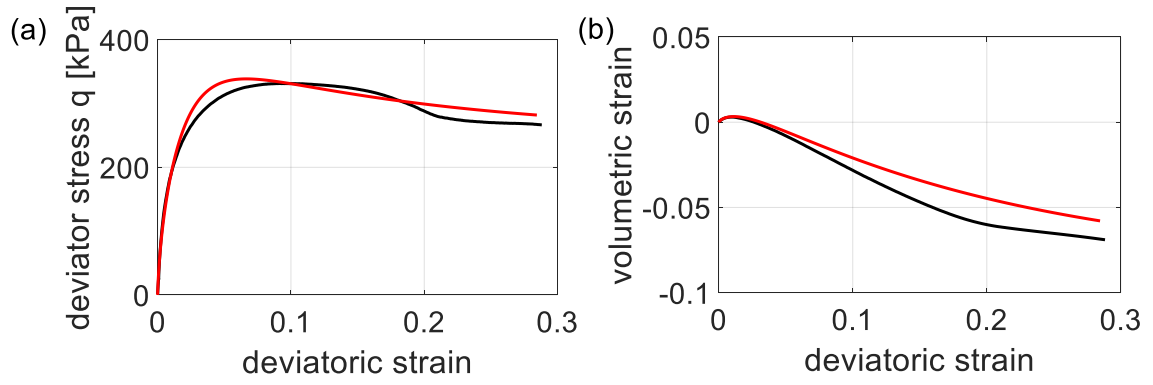


Figure 8: TMD12

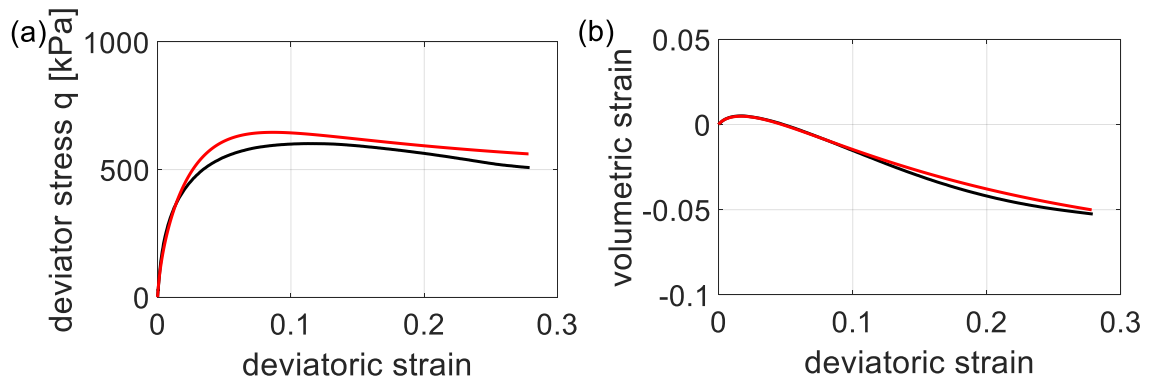


Figure 9: TMD13

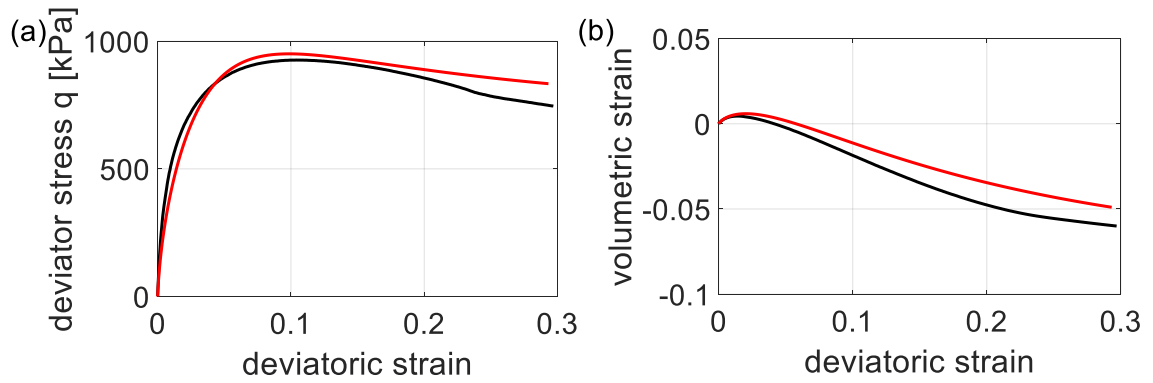


Figure 10: TMD14

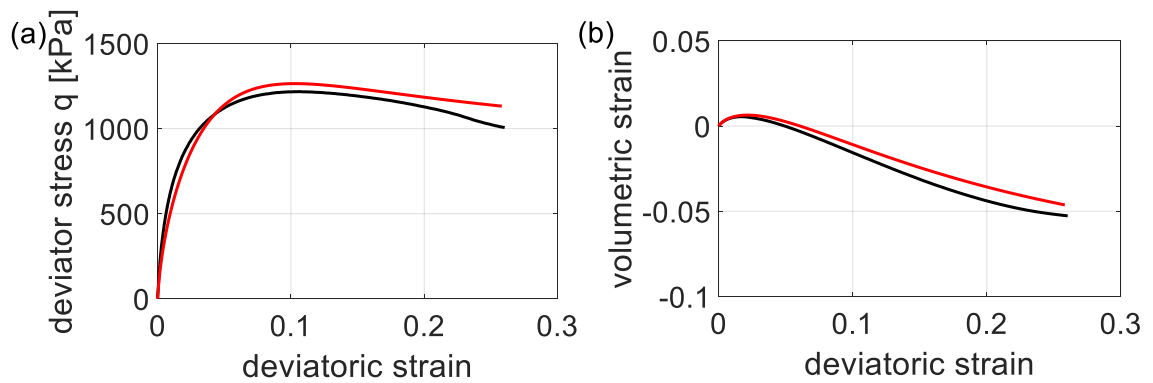


Figure 11: TMD15

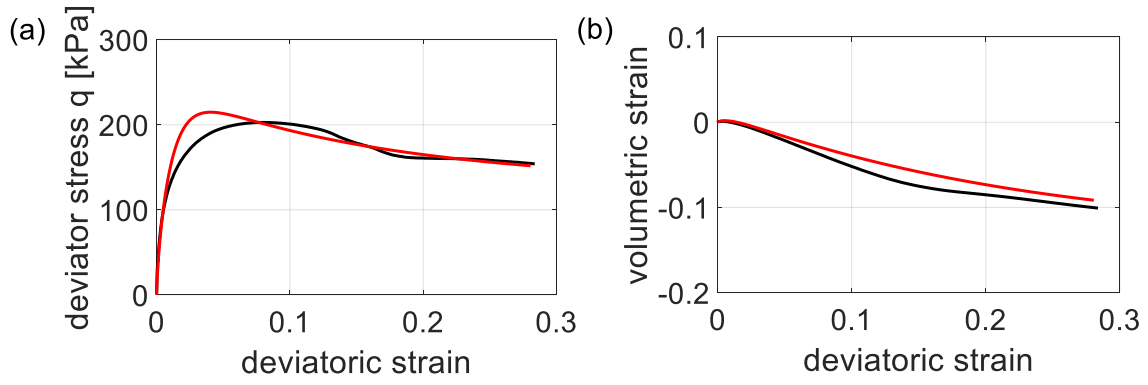


Figure 12: TMD16

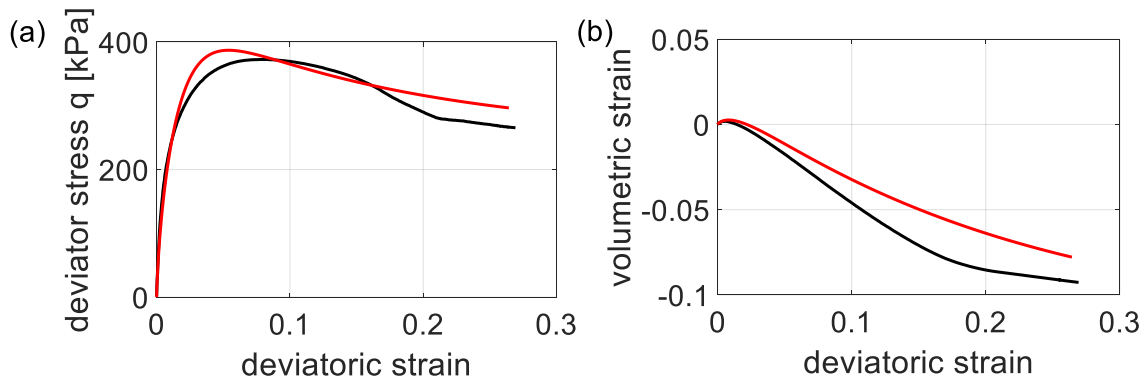


Figure 13: TMD17

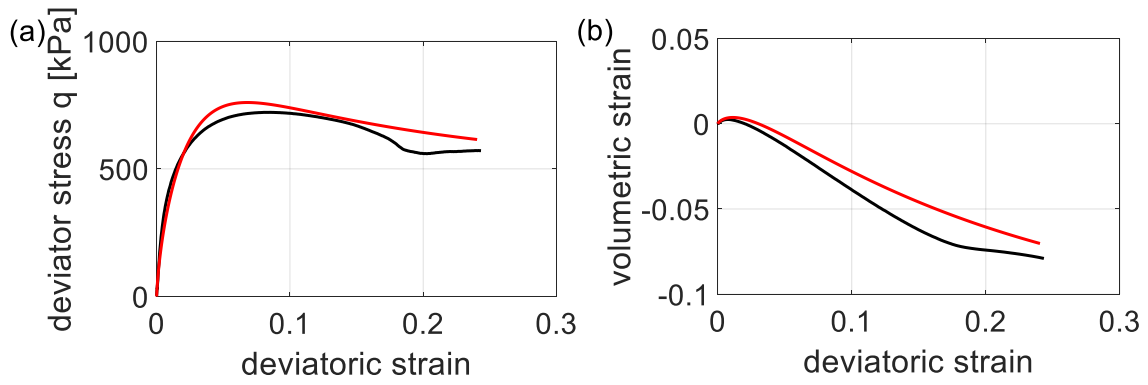


Figure 14: TMD18

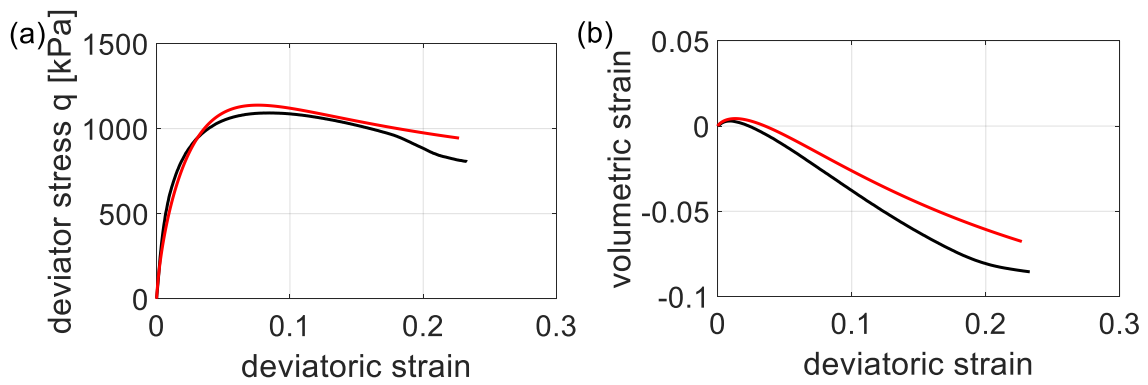


Figure 15: TMD19

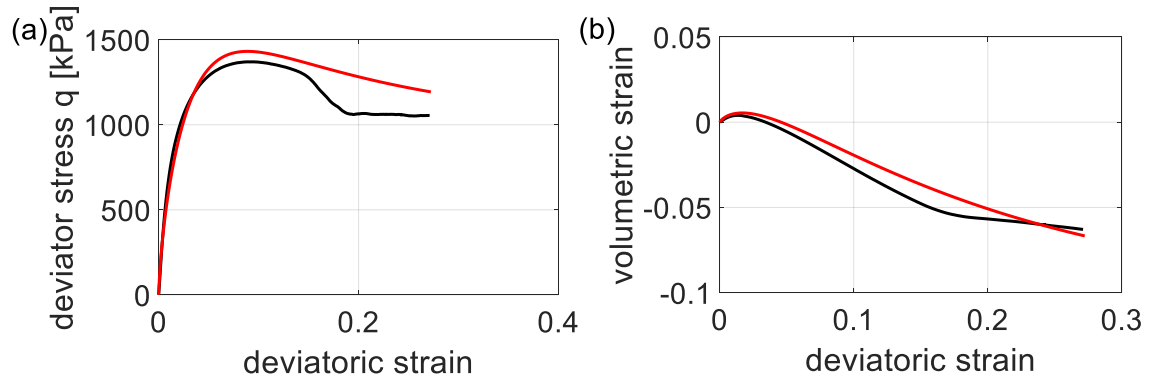


Figure 16: TMD20

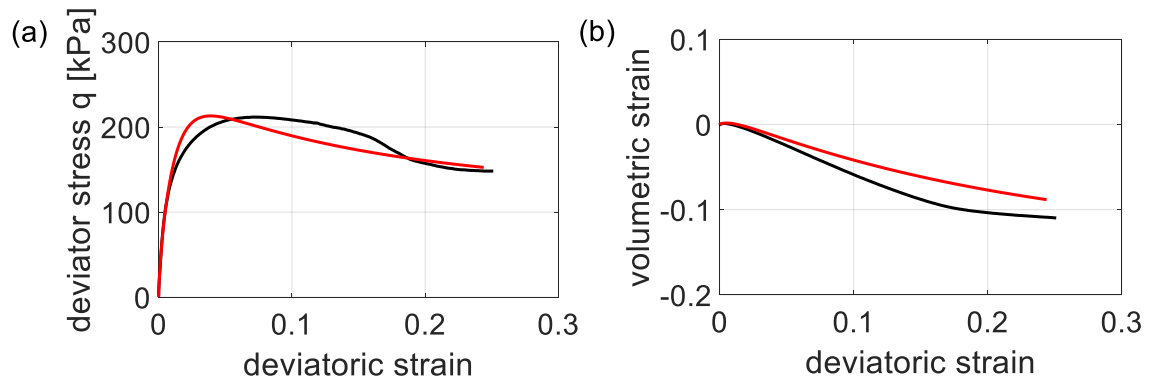


Figure 17: TMD21

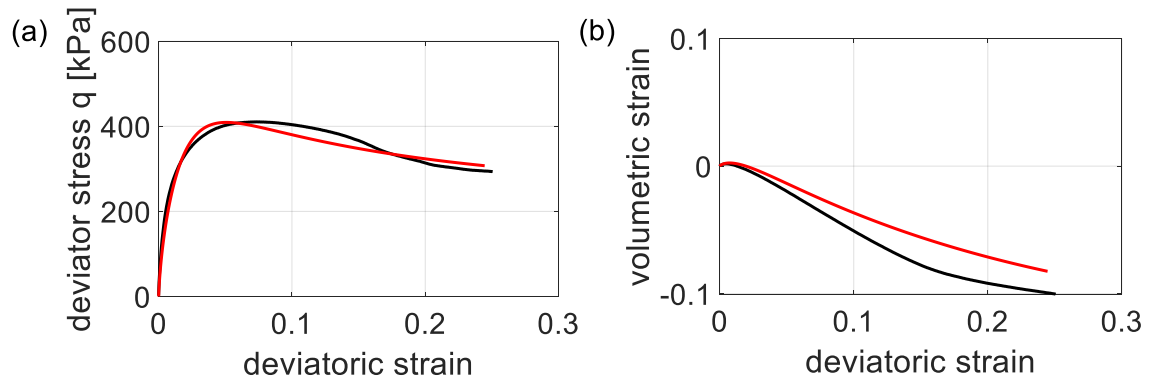


Figure 18: TMD22

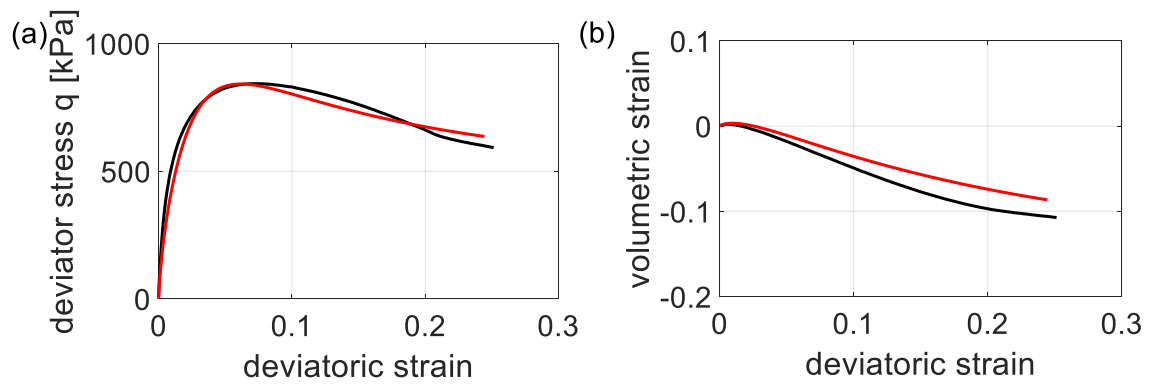


Figure 19: TMD23

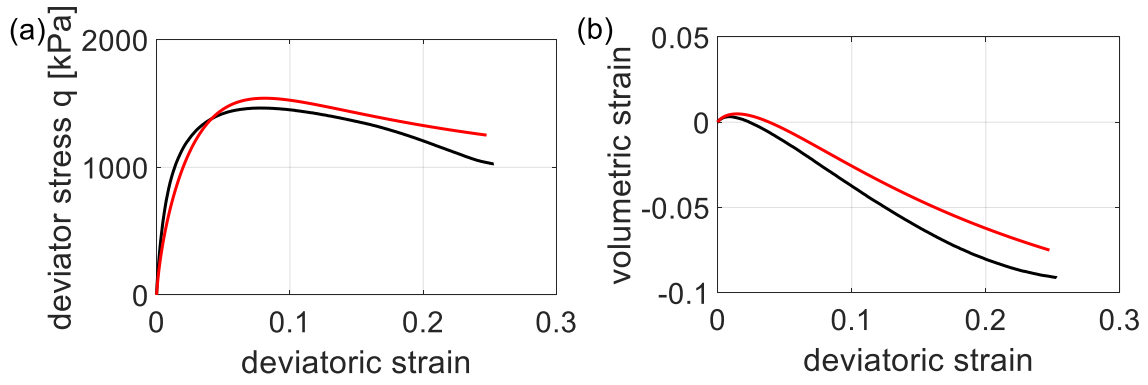


Figure 20: TMD25

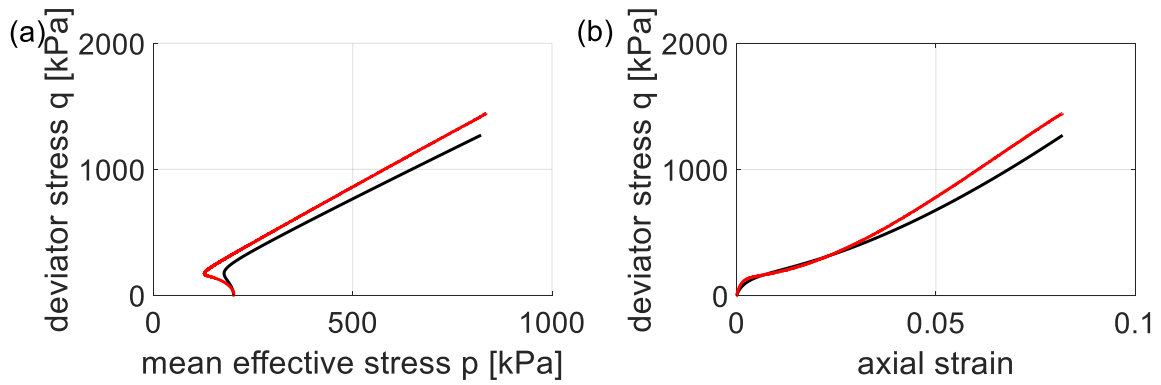


Figure 21: TMU3

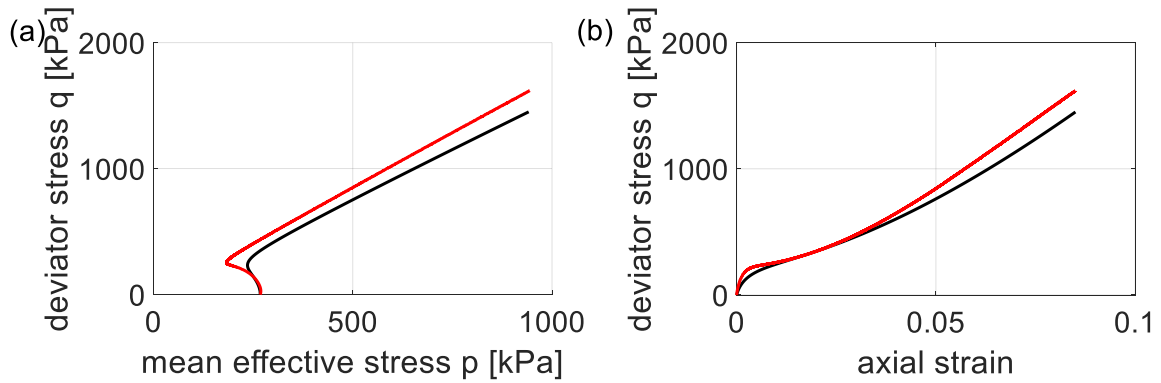


Figure 22: TMU4

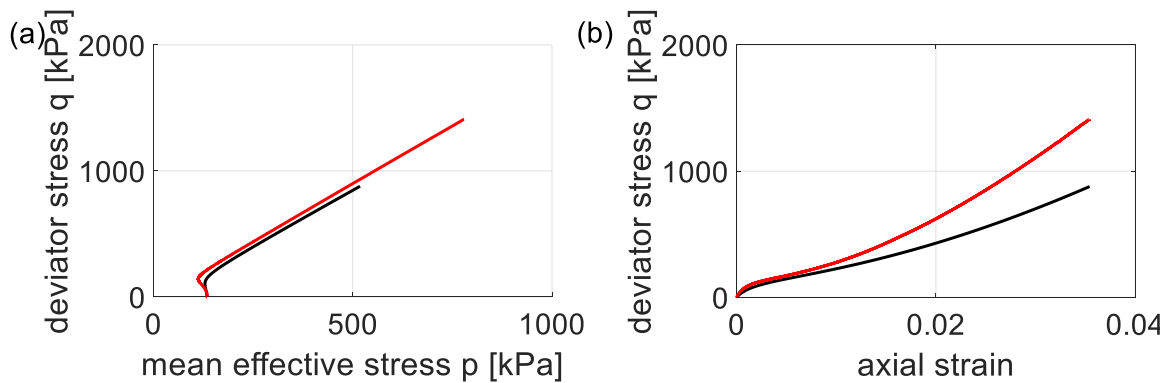


Figure 23: TMU6

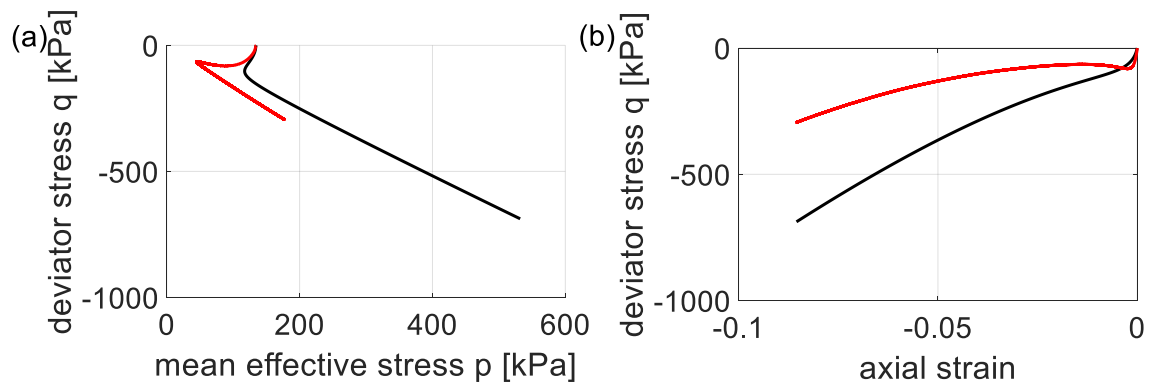


Figure 24: TMU8

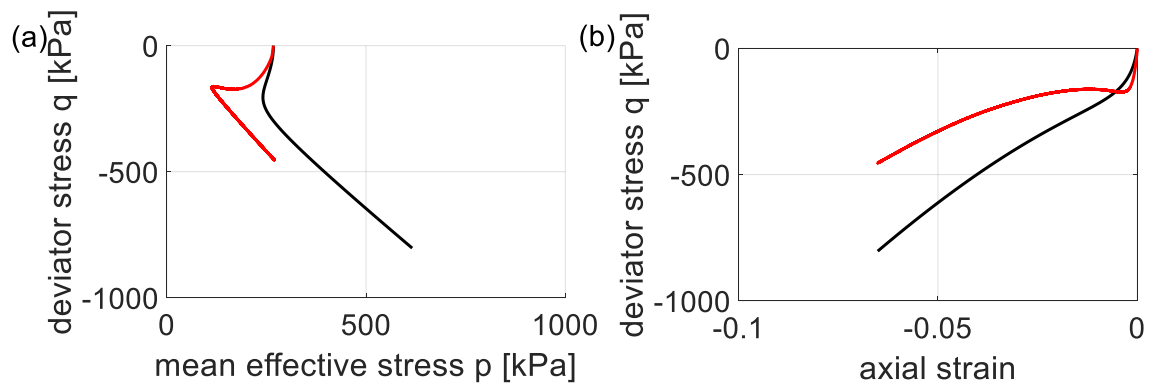


Figure 25: TMU10

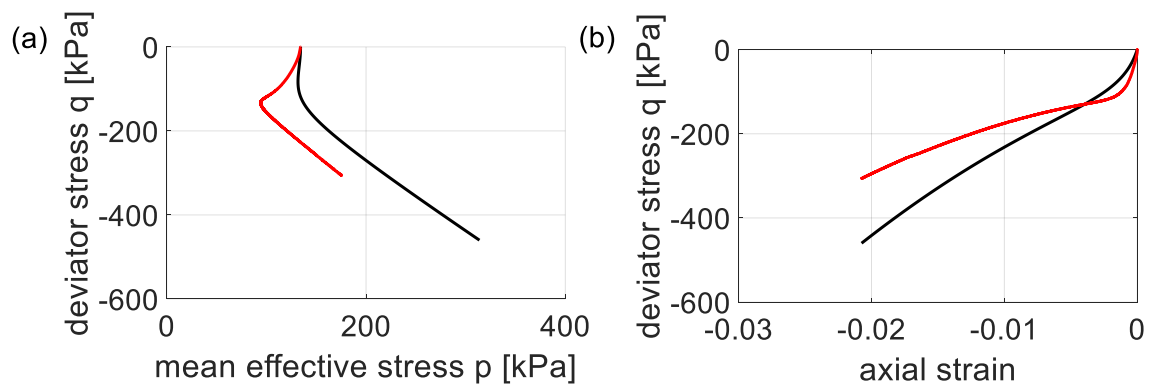


Figure 26: TMU12

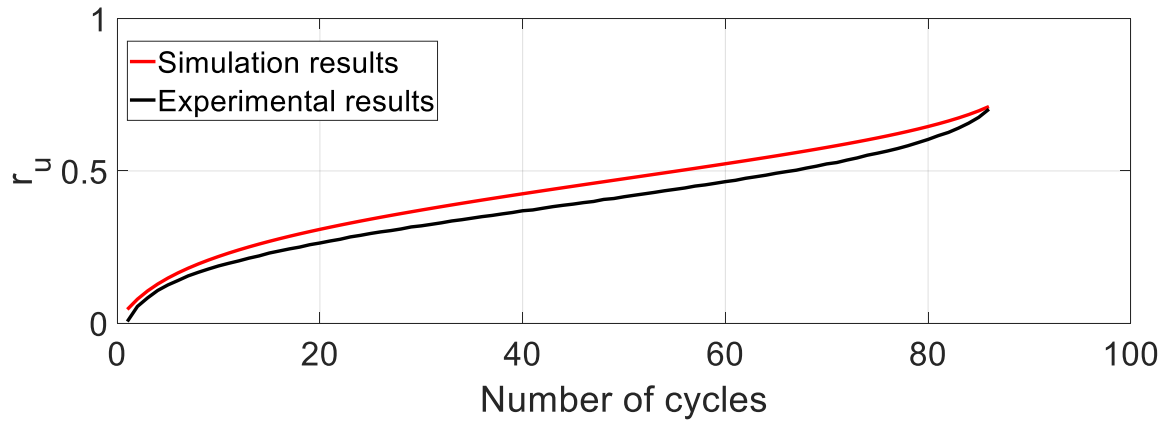


Figure 27: TCU15

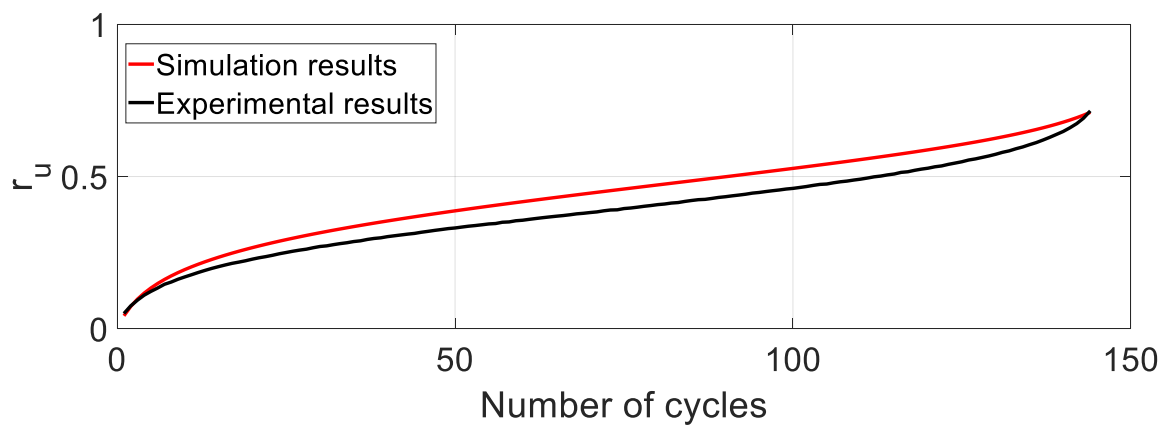


Figure 28: TCU16

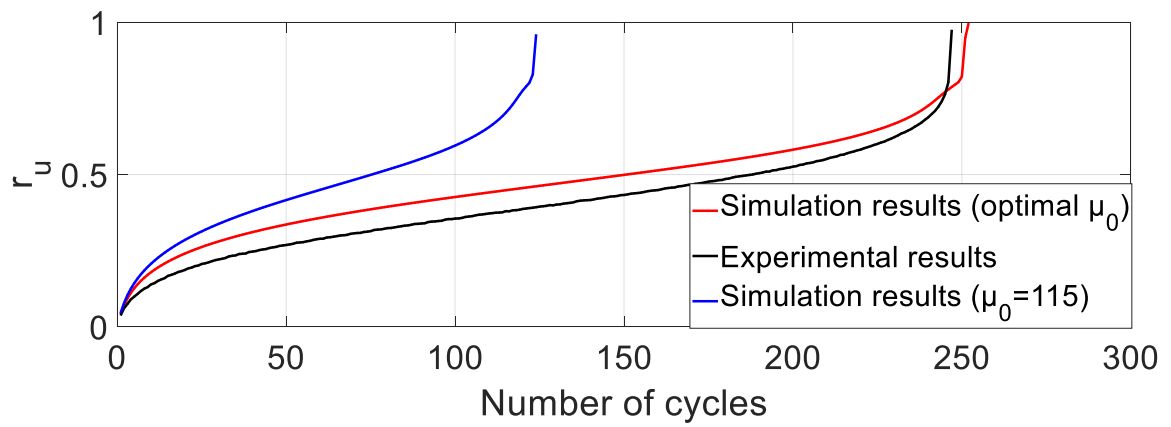


Figure 29: TCU18

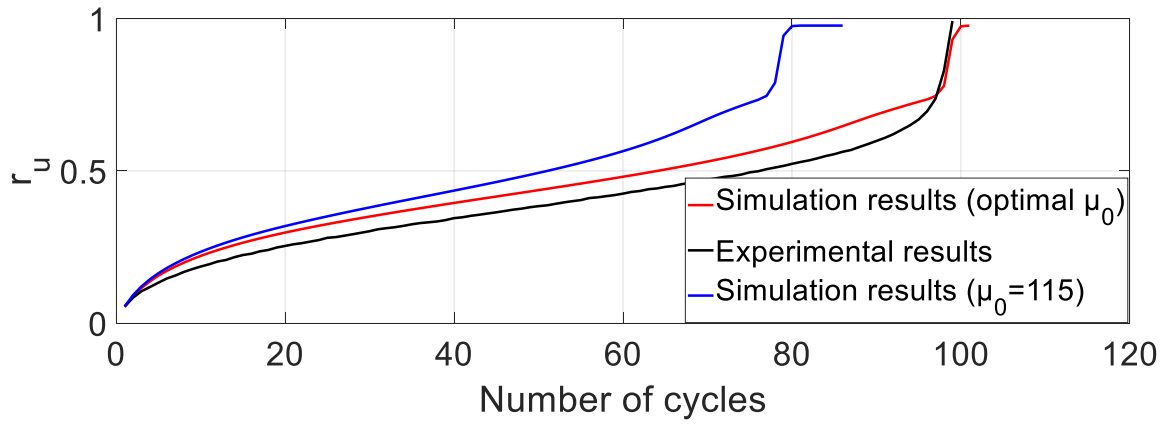


Figure 30: TCU19

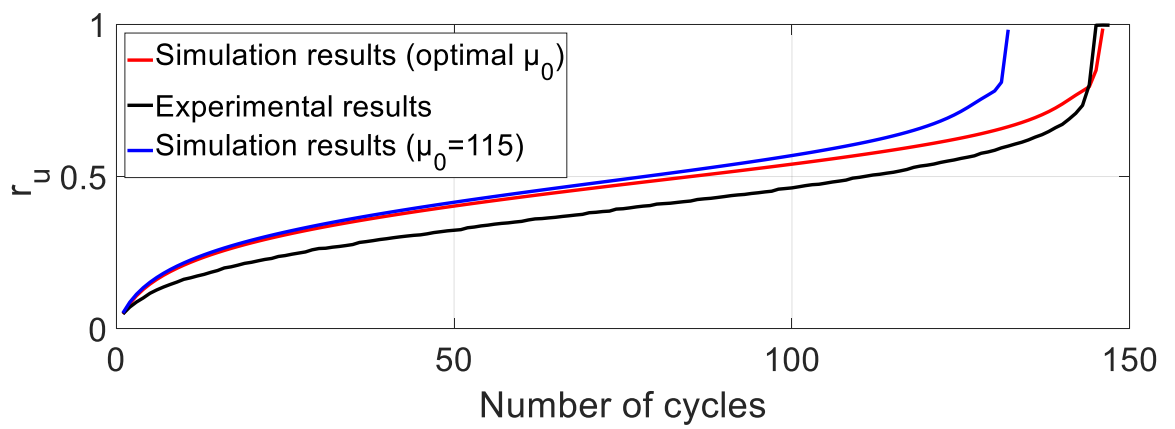


Figure 31: TCU11

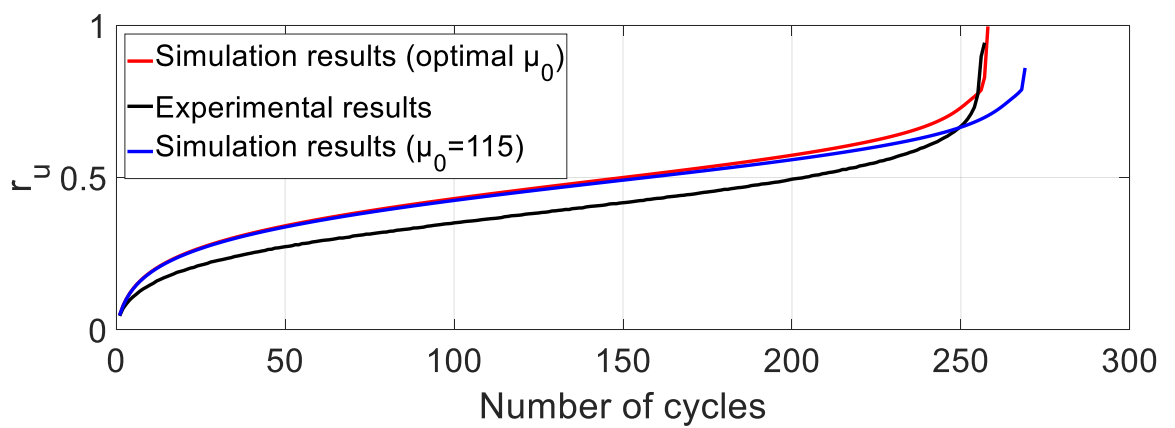


Figure 32: TCU14

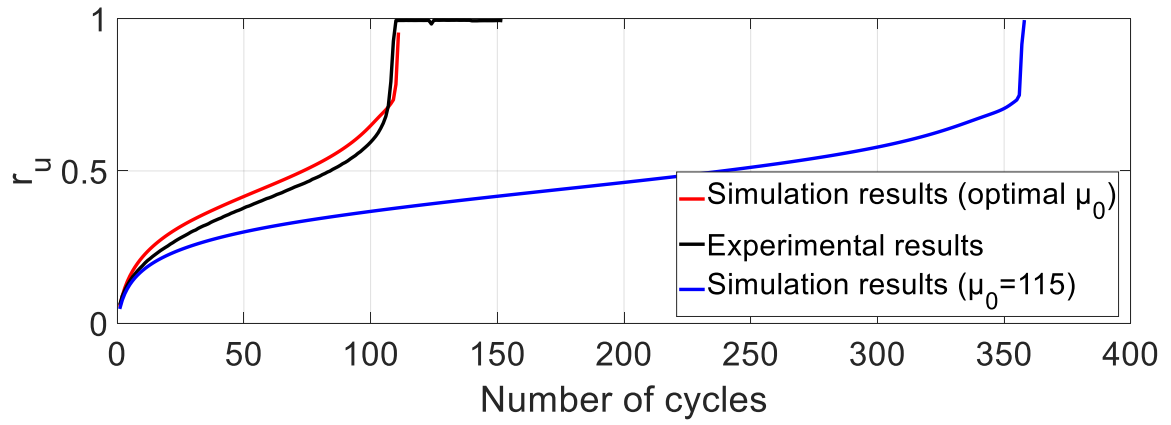


Figure 33: TCUI15

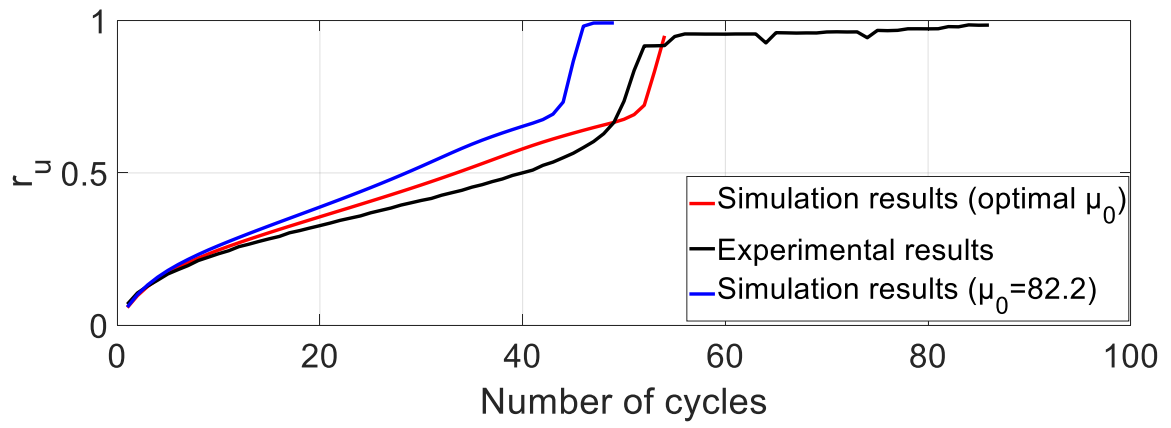


Figure 34: TCUI18

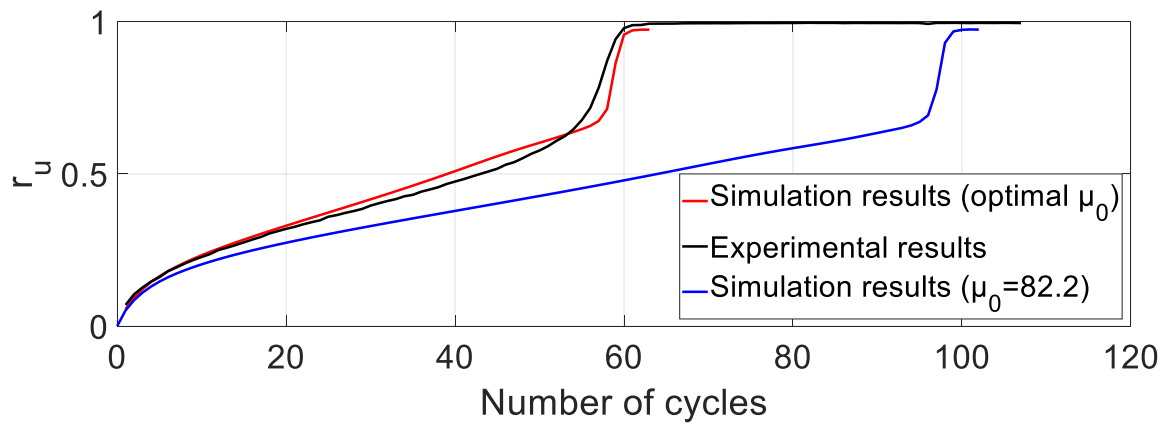


Figure 35: TCUI21

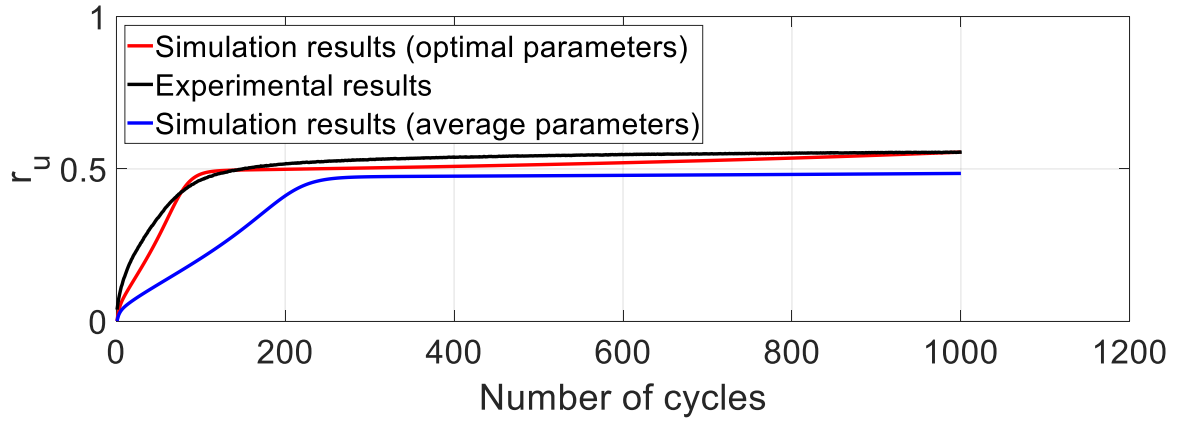


Figure 36: TCUA4

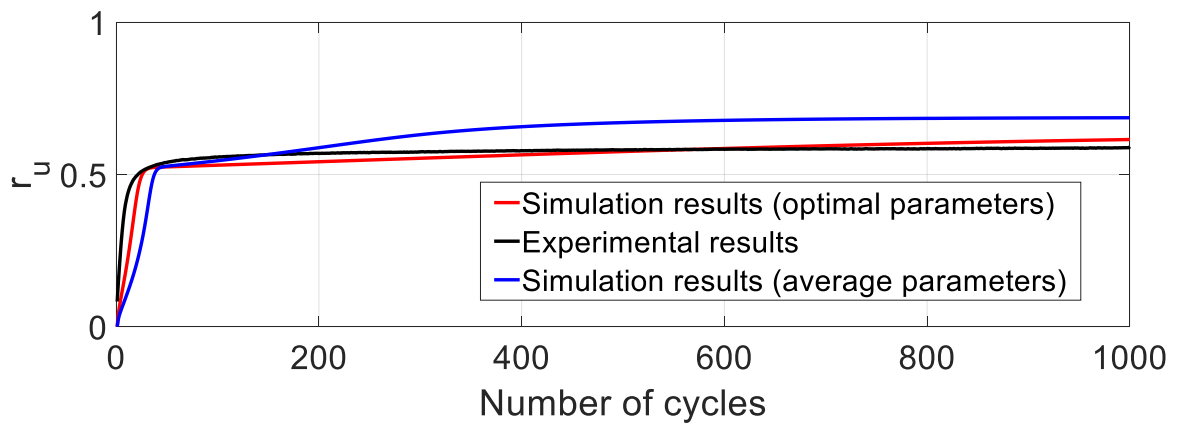


Figure 37: TCUA5

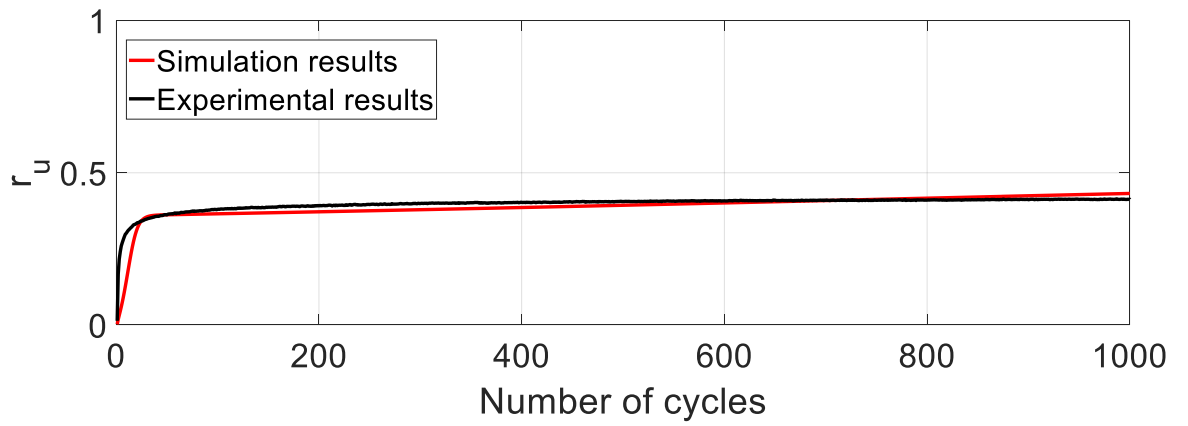


Figure 38: TCUA9

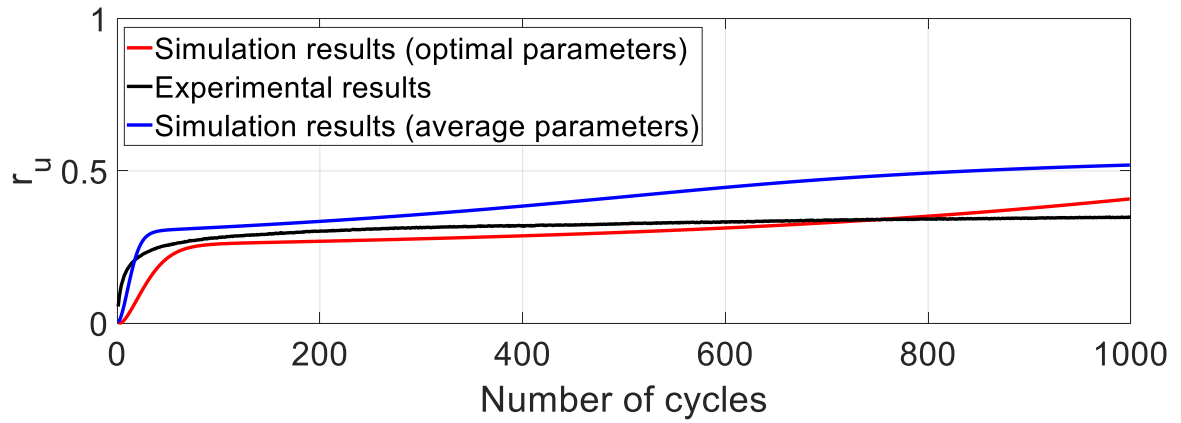


Figure 39: TCUA10

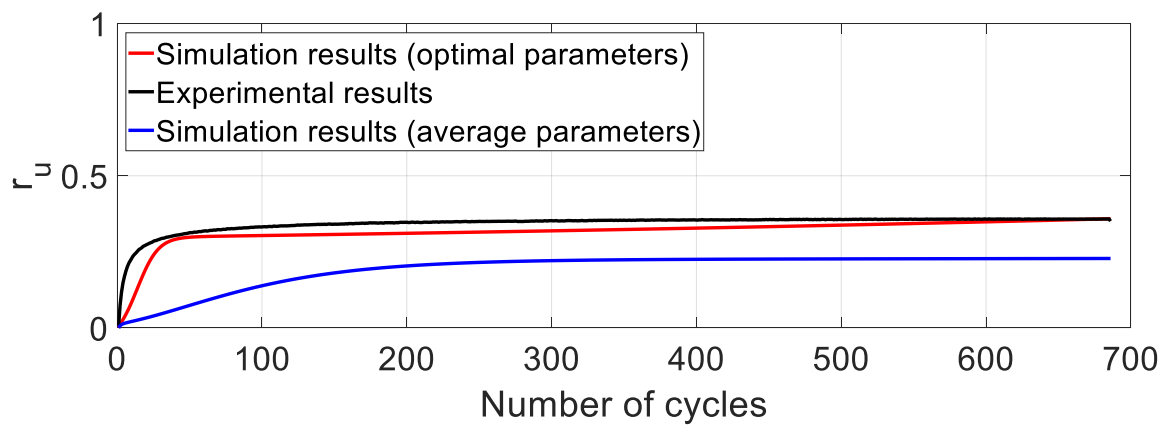


Figure 40: TCUA11

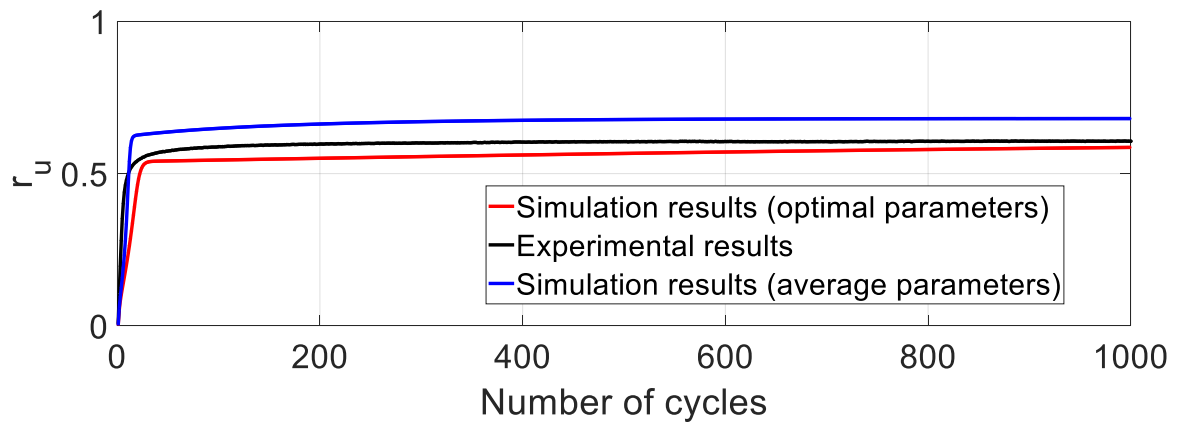


Figure 41: TCUA14

